Catarina Lopes Serra

MODELLING OF HEAT DIFFUSION FOR INFRARED THERMOGRAPHY APPLICATIONS IN BUILDING ELEMENTS

PhD Thesis in Sustainable Energy Systems
supervised by Professor António José Barreto Tadeu and Professor Nuno Albino Vieira Simões
submitted to the Department of Mechanical Engineering of the
Faculty of Sciences and Technology of the University of Coimbra

March 2017

· U C ·

UNIVERSIDADE DE COIMBRA

· U C ·

UNIVERSIDADE DE COIMBRA

MODELLING OF HEAT DIFFUSION FOR INFRARED THERMOGRAPHY APPLICATIONS IN BUILDING ELEMENTS

by

Catarina Lopes Serra

Thesis submitted to the Department of Mechanical Engineering, FCTUC
in partial fulfilment of the requirements for the degree of
Doctor of Philosophy in Sustainable Energy Systems

Supervisors
Professor António José Barreto Tadeu
Professor Nuno Albino Vieira Simões

March 2017

MIT Portugal
ITeCons
FCT
Fundação para a Ciência e a Tecnologia
MINISTÉRIO DA CIÊNCIA, TECNOLOGIA E ENSINO SUPERIOR
POPH
UNIÃO EUROPEIA
Fundo Social Europeu

ABSTRACT

Early detection and characterization of defects may be essential to prevent building pathologies and avoid costly repair works. Different non-destructive techniques have been proposed over the years to perform these tasks, one of which is infrared thermography (IRT). IRT is a powerful tool that can be used to evaluate materials and detect defects in a non-invasive manner. In buildings, IRT has been mostly used to assess the quality of building envelopes in energy efficiency studies and detect defects such as missing insulation, air leakages, thermal bridges and excessive moisture. These studies are most frequently confined to a steady state analysis. However, in many other sectors the technique has evolved to a stage where a quantitative IRT analysis is performed, enabling the characterization of defects regarding their most relevant properties such as depth and geometry. This requires the employment of specific testing techniques, such as actively heating the test specimen, and the interpretation of IRT data using complex processing techniques which depend on the material being inspected and which involve the development of heat transfer simulation tools to describe the heat field between the defect and the surface.

Most available techniques were developed for applications in sectors such as aeronautics, mechanics and electronics and are not adequate for building materials, which generally have lower conductivity and require deeper probing. This is the motivation for the present thesis.

The main goal of this research work was to develop modelling tools that contribute to the quantitative interpretation of transient thermal data obtained from IRT applications in buildings using a phase contrast approach, and to the definition of experimental setup parameters. To achieve this goal, heat transfer by conduction in solid media was modelled using analytical solutions and numerical methods formulated in the frequency domain in an attempt to simulate experimental IRT results and to study the complex relationships that exist between the variables (material thermal properties, defect characteristics) affecting the thermal wave phase response of defective building elements in transient regime. Throughout the study, the problem being modelled progressively evolved from the case of an unbounded solid medium containing a thin defect, to a multilayered medium containing a defect within one of its layers. Numerical modelling of the three-dimensional (3D) heat diffusion in the proximity of 3D defects was performed using a formulation of the boundary element method written in terms of normal derivative integral equation (TBEM) which is suited to solve heat transfer problems in the proximity of thin inclusions. Analytical solutions based on 3D Green's functions were used to simulate heat diffusion in multilayered systems.

In order to verify the applicability of the models to simulate IRT phase contrast results, active IRT experimental studies were carried out and thermal wave phase results were obtained after applying a Fourier transform to the transient temperature responses. Tests were carried out using different test specimens that incorporated defects located at various depths. This resulted in a collection of experimental measurements which were compared to the results obtained from the simulations. It was concluded that the proposed models can be used to predict the detectability of defects and in particular can be helpful in defining experimental setup parameters. These results support the interpretation of experimental phase contrast data in quantitative IRT applications to evaluate building elements.

RESUMO

Considera-se essencial a deteção e caracterização de defeitos em elementos construtivos de forma a prevenir a ocorrência de patologias em edifícios e as reparações onerosas consequentes. Várias técnicas de inspeção não destrutivas têm sido propostas para este efeito, sendo uma delas a termografia por infravermelhos. Esta é uma ferramenta não invasiva com grande potencial para avaliar materiais e detetar defeitos. Em edifícios a termografia tem sido maioritariamente utilizada para avaliar a qualidade da envolvente térmica em estudos de desempenho energético uma vez que esta permite a deteção da falta de isolamento, da existência de fugas de ar e de pontes térmicas, bem como da concentração de água. Estes estudos estão geralmente confinados a uma análise em regime permanente. Contudo, em outros sectores esta técnica tem evoluído para uma análise quantitativa que permite uma avaliação dos defeitos relativamente às suas características mais importantes, como por exemplo a sua profundidade e geometria. Isto requer o uso de técnicas experimentais específicas, como a termografia ativa em que se faz o aquecimento ou arrefecimento da superfície em análise, e a interpretação de resultados experimentais obtidos em regime transiente. Esse processamento depende do material estudado e requer por sua vez o desenvolvimento de ferramentas de simulação da transferência de calor para descrever o campo de calor entre o defeito e a superfície.

A maioria das técnicas que se encontram disponíveis foram desenvolvidas para as áreas da aeronáutica, mecânica e eletrónica e não se encontram adequadas aos materiais de construção, que em geral apresentam uma condutibilidade menor e requerem uma inspeção a maior profundidade. Esta é a motivação para o trabalho de investigação apresentado nesta tese.

O principal objetivo do trabalho foi o desenvolvimento de modelos de simulação que permitam contribuir para a interpretação quantitativa dos resultados experimentais obtidos em regime transiente em aplicações de termografia em edifícios usando uma abordagem em termos de diferença de fase, bem como para a definição da configuração de ensaio. Para isso foram desenvolvidos modelos de transferência de calor por condução em meios sólidos com base em expressões analíticas e métodos numéricos com vista à simulação de resultados experimentais de aplicações de termografia e ao estudo das relações complexas que existem entre as variáveis que afetam a resposta, em regime transiente, da fase da onda térmica em elementos construtivos com defeitos (propriedades térmicas dos materiais e características dos defeitos). Ao longo deste trabalho, o problema a ser modelado evoluiu progressivamente: do caso de um defeito fino inserido num meio sólido infinito para um defeito fino num meio estratificado. A modelação numérica de defeitos 3D fez-se com recurso a uma formulação do método de elementos fronteira adequada para resolver problemas de transferência de calor na proximidade de inclusões finas (TBEM) e a simulação da condução 3D ao longo de meios estratificados foi feita com recurso a soluções analíticas baseadas em funções de Green.

A fim de se verificar a aplicabilidade dos modelos para simular resultados de diferença de fase em aplicações de termografia, realizaram-se ensaios experimentais com termografia ativa e obtiveram-se os resultados em termos de diferença de fase através da aplicação de uma transformada de Fourier. Os testes foram realizados utilizando provetes com defeitos localizados a profundidades distintas. Isto resultou num conjunto de resultados que foram comparados com os obtidos nas simulações. Concluiu-se que os modelos propostos podem ser utilizados para prever a detetabilidade dos defeitos e, em particular, podem ser úteis na definição dos parâmetros de teste. Estes resultados suportam a interpretação de resultados experimentais de diferença de fase em aplicações de termografia quantitativa para a avaliação de elementos de construção.

AKNOWLEDGEMENTS

The research work presented in this thesis was funded by the Foundation for Science and Technology of the Portuguese Ministry of Education and Sciences (grant SFRH/BD/91686/2012), for which I am extremely grateful. I would also like to thank the Energy for Sustainability Initiative of the University of Coimbra (EfS) for supporting the dissemination of this work over the past few years. This research has also been supported in part by the FEDER-COMPETE 2020 co-funded projects POCI-01-0247-FEDER-003393 and POCI-01-0247-FEDER-003179.

I would like to express my deepest appreciation to my supervisors, Professor António Tadeu and Professor Nuno Simões for granting me the opportunity to carry out this work at the Institute for Research and Technological Development in Construction, Energy, Environment and Sustainability (ITeCons), for providing continuous insight, knowledge and encouragement, and for allowing me to consume their time and patience.

In one way or another I am certain that all of my colleagues at ITeCons are deserving of my sincerest gratitude for their friendship and support. However, I would like to take this opportunity to personally express my thanks to Inês Simões, Joana Prata, Aurélio Gonçalves, Saúl Martins, António Nascimento and João Laranjeira for their precious help.

I would also like to point out the outstanding work done by Ana Ramos in support of the students of the EfS initiative and the MIT-Portugal Program in Coimbra.

Last but not least I want to thank my family for their love. In particular, my mom for always caring and my sister for being a constant source of inspiration.

TABLE OF CONTENTS

CHAPTER 1

INTRODUCTION

1 INTRODUCTION

1.1 Context and motivation

Infrared thermography (IRT) is a non-destructive evaluation technique which is used in many areas to detect and characterize defects located beneath the surface. In general terms, this technique consists in the analysis of thermal images recorded by an infrared camera, which is a device that is sensitive to the radiation emitted as electromagnetic waves by the surface of any object at a temperature other than absolute zero. When defects such as cracks, voids, delaminations or inclusions made of other materials are located beneath the surface, heat field propagation is affected. This changes the infrared energy emitted by the object being evaluated, causing disturbances to appear in the thermal pattern images recorded by IRT cameras. Therefore, these temperature disturbances can be used to locate hidden defects. Furthermore, successive thermal images recorded over time can be analysed to gather more information regarding defect characteristics such as depth or size. Additionally, different transformation techniques can be used to analyse thermal response in other domains, such as the frequency domain and the wavenumber domain. In the literature, many accounts can be found reporting the use of phase images to enhance defect detectability and geometry resolution.

IRT has become a popular inspection method used and it is currently used to detects defect in many applications, including civil engineering. Its growing popularity stems from being non-contact, not harmful to its users or its subject, and increasingly more affordable with the advancement of technology. In buildings, IRT is mostly used in energy efficiency studies to detect concentrated heat losses due to missing or damaged insulation, air leakages or thermal bridges, and to identify areas of excessive moisture. Using this technique in constructions has provided insightful and useful information leading to low-cost repair work and avoiding more aggressive inspection techniques as well as the consequent, much more costly, extensive renovations. However, these studies have been mostly confined to the thermal steady state analysis of the quality of the building envelope.

Increasing demand for low energy consumption and predictive maintenance of constructions strongly supports broadening IRT applications in buildings, since using a quantitative approach could lead to a more reliable identification and characterization of anomalies present in the building’s thermal envelope elements. Nonetheless, the relationships between the variables affecting the thermal response of materials and construction elements in transient regime are quite complex. Hence, the correct interpretation of IRT data for defect characterization requires the full knowledge of transient heat transfer phenomena and involves using specific testing techniques. Over the years, numerous techniques have been developed for industrial IRT applications which mostly focus on the evaluation of thin materials with high diffusivity. Hence, these testing and processing techniques are generally inadequate for construction materials, which mostly exhibit relative low conductivity and contain deeper defects.

It can be said that the importance of developing behaviour simulation tools for IRT applications is twofold. On the one hand, evaluation of defects can be achieved by solving inverse heat transfer problems in which the unknown conditions are the characteristics of the defect or of the material that is being investigated and what is known is the experimentally obtained IRT data. These systems are frequently ill-posed. On the other hand, the accurate analytical and numerical simulation of IRT experimental results is particularly useful for assessing the limitations of the technique and for defining test parameters required for the experimental setup. Valuable time and resources may be saved by using simulation tools since unnecessary preliminary testing can be avoided.

The research work presented in this thesis is driven by the fact that, in order for quantitative thermographic data analysis to be achieved in building applications, a deep understanding of transient heat transfer phenomena and the development of simulation models adequate for building elements is necessary. Along with their experimental validation, the development and implementation of such models is the main focus of this thesis. This work is aligned with the longstanding interest of the research team in developing tools to simulate the behaviour of buildings and building elements. In particular, correctly assessing the thermal behaviour of buildings in transient regime is considered essential within the context of energy efficiency and sustainability. An early detection and characterization of defects that may compromise the performance of building elements is essential for preventing building pathologies. Furthermore, the assessment of the integrity of structures, or the evaluation of detachments in building facades are examples of IRT applications that address concerns with safety in buildings.

In experimental IRT, the disturbed heat field caused by the presence of a defect propagates to the surface by conduction. Transient heat transfer by conduction in solids can be simulated using one of two approaches: analytical expressions or numerical methods. Analytical expressions provide exact solutions to the heat conduction problem in simple models and they can also serve as the basis for the formulation and the verification of numerical methods. Numerical models are used in more complex cases which cannot be solved analytically. These are able to provide good estimates of the solution. However, they require the use of high performance computers to make the calculations. With the progress of computer technology, the potential for using numerical methods has a tendency to increase. Nonetheless, even numerical models have limitations, in particular regarding computational effort. As the complexity of the problems increases in search for more realistic models, there is a continued need for researchers to develop new numerical models and applications.

In order to model transient heat diffusion in solid media, both the analytical and numerical approaches were used in this work. Analytical solutions based on Fourier and Bessel transformations were used to simulate three-dimensional (3D), two-dimensional (2D) and one-dimensional (1D) heat diffusion in multilayered media, and a formulation of the boundary element method (BEM) was used to model thin defects located in unbounded or layered media.

The benefits of using BEM are well documented. Compared to other modelling techniques based on domain discretization, the methods employed here only required the discretization of the inclusion being modelled, which corresponds to a great deal of savings in computational effort. Nonetheless, also presented in this work is an iterative approach to reduce the processing time of

BEM computations when dealing with multiple thin defects, which can also be seen as a tool that is able to reduce the time required to model any thin 3D defect (considering that it is divided into multiple inclusions).

Looking to benefit from the advantages shown by phase images in IRT experiments, the formulation of the problem was posed in the frequency domain, which allows for thermal wave phase to be computed directly, and results were analysed using a phase contrast approach. In defect detection studies, phase contrast refers to the difference between phase response in a defective area of the surface and the phase response in a sound area of the surface which does not contain defects. This difference can be used to describe a certain defect. In fact, the graphical representation of phase contrast obtained along the frequency spectrum (phase contrast curves) can contain information that is particularly useful in defect detection studies, such as the frequency at which a defect is most visible, or no longer visible, in terms of phase images.

The usefulness of these models was substantiated by performing experimental tests using active infrared thermography. Active infrared thermography are experiments that use an additional thermal stimulus to enhance the thermal imprint made by a defect. Since heat transfer occurs anytime there is a temperature difference (thermal energy naturally travels from areas of higher temperature to lower temperature), heating or cooling of the surface being inspected can be used to generate a greater temperature difference. In this study tests were performed using an active thermography technique based on prolonged periods of thermal stimulation and recording to allow for the long response of construction materials. Then, experimental frequency domain temperature results were calculated by applying a Fourier transform to the thermal response obtained in each pixel of the image recorded by the IRT camera.

The study presented herein is aligned with the research work developed at the host institution of the candidate, the Institute for Research and Technological Development in Construction, Energy, Environment and Sustainability (ITeCons), as well as the research areas of the Sustainable Energy Systems educational program under the MIT Portugal Program.

1.2 Objectives

The main goal of this research work was to contribute to the successful implementation of quantitative IRT as a reliable, non-destructive tool that can be used in building inspections to assess the integrity of building systems and structural elements in construction. To achieve this, the research focused on the development of models that attempt to describe the heat field created in solid media containing defects in the presence of a heat source, so as to simulate real active IRT experiments in buildings.

In order to reach this main goal, the following specific objectives were set out for the research:

- Development of numerical models that simulate heat transfer around 3D thin defects located in unbounded or layered media, subjected to either 3D or 1D heat sources;
- Implementation of numerical techniques that reduce the computational effort required to perform numerical calculations;
- Verification of the formulation of the models using analytical solutions or previously validated numerical models;
- Validation of the applicability of the models to simulate IRT tests by carrying out an experimental campaign using active infrared thermography on test specimens that simulate building elements with defects;
- Evaluation of the influence that a number of factors, which need to be accounted for when interpreting quantitative IRT data and defining test parameters (defect depth, size, shape, thickness and position, material properties, recording time or frame acquisition rate), have on the heat field disturbance created by the presence of a defect;
- Assessment of the limitations of defect detection using IRT in building elements and constructions by using case studies and test specimens that use common construction materials and that follow a layered configuration.

To attain these objectives, the research was structured around a sequential increase of the complexity of the system being modelled. This structure is explained in the next section.

1.3 Thesis structure

Besides its introduction and conclusion, the thesis is divided into four core chapters corresponding to the four main stages of the research. To facilitate its reading, this document is written in such a way that each chapter may be accessed individually. Therefore, each chapter contains its own introduction, problem definition and formulation, the results discussion, conclusions and references. Even though some overlapping may occur, due care has been taken to highlight the specificities of each part.

As mentioned before, the main focus of this research was the development of numerical models for IRT applications in buildings to enable a quantitative analysis of transient heat transfer results. Over the several chapters there is a clear evolution of the system being modelled, from a simpler case to a more sophisticated system that resembles a multilayered building element containing a thin 3D defect.

Chapter 2 of the thesis presents a numerical model based on a boundary element method (BEM) formulation in the frequency domain for the simulation of 3D heat conduction around a thin inclusion located in a solid. At this stage, the isotropic and homogeneous (other than for the defect) solid media is considered to be unbounded (infinite). A modified formulation of the 3D BEM, referred to here as 3D TBEM, is used to handle the thin defect. Analytical solutions to compute the resulting hypersingular integrals that occur in this method are also presented. The procedures used to obtain phase contrast results and time domain temperature responses are also described. The formulation is followed by a verification of the numerical model using analytical solutions for cylindrical inclusions. Finally, computations are performed for a number of case studies in which defect characteristics are changed so as to understand their influence in the results. The main results are presented and discussed.

In Chapter 3, the focus of the study is shifted to the development of an iterative approach that can be applied to the previous 3D TBEM model in order to reduce computational time. The results presented are focused instead on the evaluation of the performance of the iterative method. This is done by comparing the processing time required for the full formulation presented in the previous chapter in the presence of multiple inclusions, with the iterative approach. Furthermore, a domain decomposition method is also considered to analyse the inclusions either as a pair or separately.

The approach presented here was applied to an unbounded medium with multiple parallel inclusions, however, it should be noted that this approach may also be used to model one inclusion divided into smaller parts.

In Chapter 4, in order to approximate the problem closer to IRT experiments performed on building elements, instead of an unbounded medium, the system under study is comprised of multiple layers with different thickness and thermal characteristics. The defect is now modelled as one of the infinite layers (in two directions) of the system, which additionally allows for the investigation of the influence of changing the defect thickness. In this chapter, 3D fundamental solutions (Green's Functions) for multilayered systems are presented, and the 3D problem is posed as a sum of 2D problems with harmonic linear sources that vary sinusoidally along one direction. This formulation is then manipulated to simulate uniform planar heating of the surface achieved in IRT tests, which further reduces the problem to a 1D model. In addition to an analytical study, this chapter also includes an experimental campaign. The experimental and numerical studies focus on evaluating the influence of relevant factors (defect depth, thickness, material properties, recording time and presence of noise) that affect time domain temperature and frequency domain phase contrast results.

Chapter 5 presents a formulation of the 3D TBEM incorporating Green's functions for multilayered media for the simulation of 3D heat diffusion around a thin defect located within a multilayered system. This is an attempt to model a building element that consists of multiple layers and which contains a thin crack, delamination or material inclusion within one of those layers. In the numerical study, the influence that the choice of non-defective area (reference for phase contrast calculations) has on results, when uniform heating is not achieved, is studied. Hence, a correction technique to account for the three-dimensionality and the placement of the heat source is also presented. Experimental results are also presented and compared to numerical results.

The last chapter of the thesis offers the main conclusions of the research work developed, along with a brief mention of potential future research studies that may provide continuity to this work.

CHAPTER 2

MODELLING OF HEAT DIFFUSION AROUND A THIN DEFECT IN UNBOUNDED MEDIA USING 3D TBEM

2 MODELLING OF HEAT DIFFUSION AROUND A THIN DEFECT IN UNBOUNDED MEDIA USING 3D TBEM

2.1 Introduction

Infrared thermography (IRT) is an effective non-destructive testing (NDT) tool that can be used to find and evaluate defects located beneath the surface in many applications in several areas. When sequential thermal images are recorded by infrared cameras, it can be possible to achieve the characterization of major properties such as defect depth and material thermal properties [1]. Furthermore, it is also known that by applying domain transformation techniques to obtain IRT test results in the frequency domain, additional information can be extracted, namely phase images can be generated. However, in order to obtain useful experimental data, it is necessary to use specific testing and data processing techniques [2].

In order to correctly interpret transient thermal data recorded in IRT tests it is essential that heat transfer simulation tools are developed and that the complex heat transfer phenomena that occur within the material are fully understood. Nonetheless, the three-dimensional (3D) nature of defects combined with the need to simulate heat transfer in a transient regime still presents many challenges for researchers developing simulation tools. It is in this context that this study presents the formulation and application of a simulation model to compute heat diffusion around a 3D defect located in an otherwise homogeneous unbounded isotropic solid medium.

In addition to providing useful information about the general thermal behaviour of the material being studied, the development and application of modelling tools can also help to define experimental setup parameters, such as recording time or type of stimulation to be used in active IRT experiments. Simulations can be used to establish the limits of the effectiveness of the IRT technique. Even though comparisons between numerical models and experimental IRT results may not always be straightforward, such simulations can be used to determine defect detectability and to quickly estimate the observation time required for best visibility of several defects with different geometries and located at various depths [1]. Without them, establishing these test parameters would require numerous experimental tests and the ensuing wastage of a great deal of specimens.

In order to extract reliable information from IRT experiments it is necessary to resort to advanced thermal data processing techniques [3] which can involve the use of calibration curves and solving inverse heat transfer problems [4]. A direct or well-posed problem is defined by having sufficient boundary and initial conditions and a unique solution, and involves solving one or more coupled integral, partial, or ordinary differential equations. On the other hand, inverse problems occur when any of the required conditions to solve the problem are unknown. In this event, additional conditions may be obtained experimentally at several points in time or space. Such is the case of the temperature data results obtained in IRT tests. In inverse heat transfer problems, the existence of a unique solution can only be demonstrated for few cases, and stability is strongly affected by the noise present in the input data [5]. Therefore, these problems are labelled as mathematically ill posed and, along with solving complex algorithms, they may require regularisation ([6],[7]) and optimisation techniques [8]. These are mainly statistics based techniques that require the full knowledge of the direct problem. Thus, one of the most important steps in solving an inverse problem is to first solve its related forward problem.

In order to solve the direct problem, there are two possible approaches that can be taken to study heat diffusion in solid media. In simple cases, such as unbounded isotropic media with flat or regular surfaces (sphere, cylinder, wedge) it is possible to establish analytical expressions that provide exact solutions [9]. More complex geometries cannot be solved using analytical expressions and their solution relies on the use of numerical models. These are mostly based on domain discretization, such as the finite elements method [10] and finite differences method ([11],[12]), or on boundary discretization, such as the boundary element method (BEM) ([13],[14]). Recently, researchers have also developed meshless formulations such as the method of fundamental solutions [15], which does not require neither domain nor boundary discretization.

It is worth noting that, even though analytical solutions may appear to be confined to simple geometries, they are still particularly useful when modelling complex systems since they allow for the verification of numerical models.

The present study is motivated by an interest in assessing the potential that IRT has for detecting defects located within building elements, such as cracks, voids or other thin inclusions, whose size, shape and position may vary. In order to do so, a numerical model to compute 3D heat diffusion around a thin 3D defect in unbounded solid media based on a boundary elements formulation is presented herein. Of the available numerical methods for homogeneous unbounded systems modelling, BEM has the clear advantage of only requiring the discretization of the boundaries of the inclusion being modelled, which in this case is the surface of the thin defect in question [13]. Nonetheless, unlike domain discretization based techniques, which give sparse systems of equations, BEM allows a compact description of the regions, resulting in fully populated systems of equations [14].

Boundary elements based models can be viewed as a systematic way to construct numerical approximations to region-dependent or exact Green's functions [16]. In fact, the major disadvantage associated with using BEM is that it requires the prior knowledge of these fundamental solutions (Green's functions). Other difficulties include the fact that using BEM can lead to the appearance of singular or nearly singular integrals. When the thickness of the inclusion being modelled tends toward null, as in the case of very thin defects, the conventional direct BEM degenerates and becomes inaccurate. To overcome this, the dual boundary element method (DBEM) [17] or the traction boundary element method (TBEM) [18] written in terms of normal derivative integral equations may be used. However, when the element being loaded is the element being integrated, these methods lead to hypersingular integrals. A number of approaches have been proposed to deal with these hypersingular integrals. Solutions for specific two-dimensional (2D) problems can be found, as proposed by Cruse [19], Sládek and Sládek [20], Prosper [21], Prosper and Kausel [22] and by Mendes and Tadeu [23]. Unlike the case of 2D problems, where closed form solutions for singular and hypersingular integrals may be used, in 3D problems, singularities are mostly solved by using numerical schemes based on Gaussian integration. However, since the accuracy of the BEM is highly dependent on the precision of these integrals, semi-analytical and analytical solutions should be favoured ([24],[25]). Recently, Tadeu *et al.* [26] described an analytical evaluation of the singular and hypersingular integrals that appear in 3D boundary element formulations for heat diffusion in the frequency domain. Regardless of these difficulties, BEM is still considered to be one of the best tools for this kind of problem, mainly due to the fact that the resulting compact systems of equations require less computational effort, and that the response anywhere in the medium can be obtained from the response at the boundary without the need to repeat calculations.

Solutions for transient heat transfer problems can be obtained in the time domain, using a time-marching approach, or in transformed domains, in which an inverse transformation is necessary to obtain the time domain results. Looking to benefit from the advantages of phase image analysis, the model used in this study is formulated in frequency domain so that thermal wave can be computed directly. The defect being modelled is assumed to have null thickness, therefore a TBEM formulation in the frequency domain is used and the resulting hypersingular integrals are solved according to the analytical method proposed and verified by Tadeu *et al.* [26].

In the sections that follow, the problem under study is first defined. In order to investigate the influence that the type of heat source may have on results, the problem presented is twofold: all computations are performed considering a 3D point heat source and 1D planar source. Hence, the 3D TBEM formulation in the frequency domain is provided for both. Also described is the procedure used to calculate thermal wave phase results from the frequency domain temperature, as well as the methodology required to generate results in the time domain. The accuracy of the proposed model is verified by considering a simple geometry (cylindrical inclusion) and using known analytical solutions. Finally, to assess the influence that certain key parameters have on IRT studies, a number of numerical applications are performed with varying defect size, shape, position, distance to the source and distance to the surface. The main results are presented for time domain temperature and thermal wave phase, both in terms of phase contrast images and phase contrast curves.

2.2 Problem definition

The problem under study is the simulation of 3D heat transfer by conduction that occurs at $\boldsymbol{x}=\left(x,y,z\right)$, which can be anywhere in the proximity of a 3D thin inclusion located in a spatially uniform unbounded solid medium of density ρ, thermal conductivity λ and specific heat c. The inclusion is assumed to be of null thickness and null heat fluxes are prescribed along its surface S. This system is illustrated in Figure 2.1.

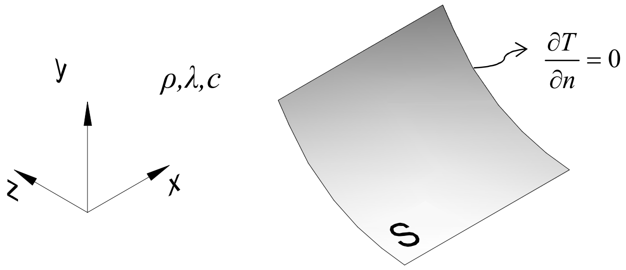

Figure 2.1: Geometry of the problem of 3D heat diffusion around a 3D thin defect.

The system may be subjected to either a 3D point heat source, which propagates energy in all directions (see Figure 2.2) or to a 1D planar heat source, for which it is considered that heat is propagated in only one direction (the x axis, as seen in Figure 2.3).

2.3 Problem formulation

In cartesian coordinates, 3D heat diffusion is governed by the following equation:

$$\left(\frac{\partial^2}{\partial x^2}+\frac{\partial^2}{\partial y^2}+\frac{\partial^2}{\partial z^2}\right)T\left(t,\boldsymbol{x}\right)=\frac{1}{K}\frac{\partial T}{\partial t}, \tag{2.1}$$

where $T\left(t,\boldsymbol{x}\right)$ is transient temperature, t is time and the thermal diffusivity is $K=\lambda/\left(\rho c\right)$, in which λ is thermal conductivity, ρ is density and c is specific heat capacity. By applying the Fourier transform to (2.1) we obtain a Helmholtz equation that expresses heat diffusion in the frequency domain:

$$\left(\frac{\partial^2}{\partial x^2}+\frac{\partial^2}{\partial y^2}+\frac{\partial^2}{\partial z^2}+\left(\sqrt{-\frac{\mathrm{i}\,\omega}{K}}\right)^2\right)\hat{T}\left(\omega,\boldsymbol{x}\right)=0, \tag{2.2}$$

in which $\hat{T}\left(\omega,\boldsymbol{x}\right)$ is temperature in the frequency domain, ω is angular frequency and $\mathrm{i}=\sqrt{-1}$. The Helmholtz equation allows heat diffusion to be studied as the propagation of harmonic waves oscillating at a frequency of ω.

3D heat transfer by conduction given in Equation (2.2) can also be written as:

$$\left(\frac{\partial^2}{\partial x^2}+\frac{\partial^2}{\partial y^2}+\frac{\partial^2}{\partial z^2}\right)\hat{T}(\omega,\boldsymbol{x})+k_c^{\,2}\,\hat{T}(\omega,\boldsymbol{x})=0\,, \tag{2.3}$$

in which $k_c=\sqrt{-\mathrm{i}\omega/K}$.

2.3.1 Heat field in unbounded solid media subjected to a 3D heat source

Consider the system in Figure 2.2, which is subjected to a 3D heat source placed at $\boldsymbol{x}_s=(x_s,y_s,z_s)$ given by $p(\omega,t,\boldsymbol{x})=P\delta(x-x_s)\delta(y-y_s)\delta(z-z_s)e^{\mathrm{i}\omega t}$, where P is the amplitude of the heat source and $\delta(x-x_s)$, $\delta(y-y_s)$ and $\delta(z-z_s)$ are Dirac delta functions.

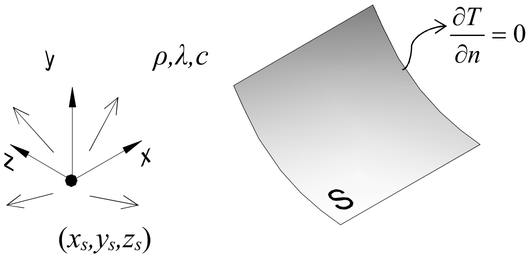

Figure 2.2: Geometry of the problem of 3D heat diffusion around a 3D thin defect subjected to a 3D point heat source.

Solving Equation (2.2) provides the heat field incident at $\boldsymbol{x}$ located anywhere in the domain, which is given by the following expression:

$$\hat{T}_{inc}(\omega,\boldsymbol{x},\boldsymbol{x}_s)=\frac{P\,e^{-\sqrt{\frac{\mathrm{i}\omega}{K}}r_s}}{2\lambda r_s}\,, \tag{2.4}$$

in which $\hat{T}_{inc}(\omega,\boldsymbol{x},\boldsymbol{x}_s)$ is the incident heat field and $r_s=\sqrt{(x-x_s)^2+(y-y_s)^2+(z-z_s)^2}$ is the distance to the heat source.

2.3.2 Heat field in unbounded solid media subjected to a 1D heat source

Now consider the system in Figure 2.3, which is subjected to a 3D heat source, but instead the incident heat field is generated by a planar heat source given by $\hat{p}\left(\omega,t,\boldsymbol{x}\right)=P\delta\left(x-x_s\right)e^{\mathrm{i}\omega t}$ located at $\boldsymbol{x}_s=\left(x_s,y,z\right)$.

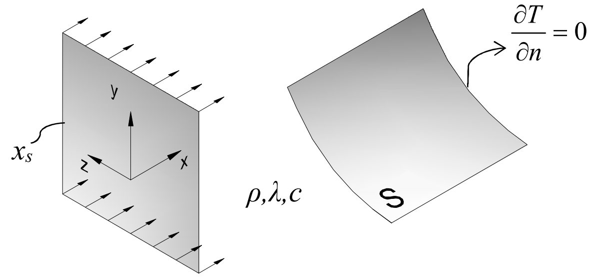

Figure 2.3: Geometry of the problem of 3D heat diffusion around a 3D thin defect subjected to a 1D planar heat source.

The solution to the 3D heat diffusion problem can be obtained by applying a double spatial Fourier transformation in the *y* and *z* directions to Equation (2.4). The heat field anywhere in the domain is given by:

$$\hat{T}_{inc}(\omega,\boldsymbol{x},x_s)=\frac{-\mathrm{i}P\mathrm{e}^{-\mathrm{i}\sqrt{-\frac{\mathrm{i}\omega}{K}}\left|x-x_s\right|}}{2\lambda\sqrt{-\frac{\mathrm{i}\omega}{K}}}. \tag{2.5}$$

2.3.3 Normal derivative integral equation (3D TBEM)

First consider a more general problem of a 3D solid inclusion with surface S_V located in an unbounded spatially uniform solid medium. This is illustrated in Figure 2.4.

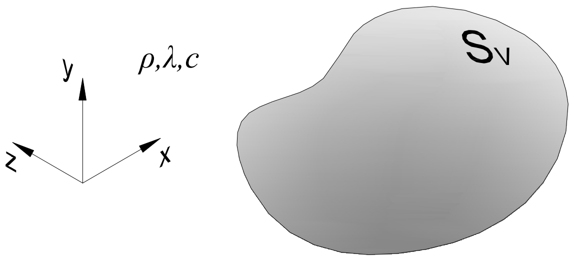

Figure 2.4: Geometry of the problem of 3D heat diffusion around a 3D solid inclusion.

When using the conventional boundary element method to solve heat diffusion around a solid inclusion with surface S_V, the BEM formulation in the frequency domain obtained from applying the reciprocity theorem is given by the classical boundary integral equation expressed by the following equations.

Along the outside boundary of the inclusion:

$$
\begin{aligned}
b\hat{T}(\omega,\boldsymbol{x}_0) = & \int_{S_V} G^{out}\left(\omega,\boldsymbol{x},\boldsymbol{x}_0\right) q^{out}\left(\omega,\boldsymbol{x},\mathbf{n}_{n1}\right)\mathrm{d}s \\
& -\int_{S_V} H^{out}(\omega,\boldsymbol{x},\boldsymbol{x}_0,\mathbf{n}_{n1})\hat{T}(\boldsymbol{x},\omega)\,\mathrm{d}s + \hat{T}_{inc}(\omega,\boldsymbol{x}_0,\boldsymbol{x}_s)\,.
\end{aligned}
\qquad (2.6)
$$

Along the inside boundary of the inclusion:

$$
\begin{aligned}
b\hat{T}(\omega,\boldsymbol{x}_0) = & \int_{S_V} G^{in}\left(\omega,\boldsymbol{x},\boldsymbol{x}_0\right) q^{in}\left(\omega,\boldsymbol{x},\mathbf{n}_{n1}\right)\mathrm{d}s \\
& -\int_{S_V} H^{in}(\omega,\boldsymbol{x},\boldsymbol{x}_0,\mathbf{n}_{n1})\hat{T}(\omega,\boldsymbol{x})\,\mathrm{d}s\,.
\end{aligned}
\qquad (2.7)
$$

In these equations G and H are Green's fundamental solutions for temperature $\hat{T}(\boldsymbol{x},\omega)$ and heat flux $q\left(\omega,\boldsymbol{x},\mathbf{n}_{n1}\right)$ for point $\boldsymbol{x}$ of boundary S_V subjected to a virtual heat load placed at a collocation point $\boldsymbol{x}_0 = \left(x_0, y_0, z_0\right)$; $\mathbf{n}_{n1}$ represents the unit outward normal along the boundary S_V at point $\boldsymbol{x}$; $\hat{T}_{inc}(\omega,\boldsymbol{x}_0,\boldsymbol{x}_s)$ is the heat field incident at $\boldsymbol{x}_0$ generated by the heat source located at $\boldsymbol{x}_s$; and b is a constant defined by the shape of the boundary, which is ½ if $\boldsymbol{x}_0 \in S_V$ and S_V is regular and continuous or 1 otherwise.

Solving these integrals requires the discretization of the boundary S_V into N_V boundary elements with one node per element. Each element may have one, four or nine nodes, if the interpolation functions are constant, linear or quadratic. The constant interpolation functions are used to illustrate how equations (2.6) and (2.7) are discretized. These expressions can be written as:

Along the outside boundary of the inclusion:

$$
\sum_{l=1}^{N_V} q^{l\_out} G^{kl\_out} - \sum_{l=1}^{N_V} \hat{T}^{l\_out} H^{kl\_out} + \hat{T}_{inc}^{k} = \tilde{b}_k \hat{T}^{k\_out}\,. \qquad (2.8)
$$

Along the inside boundary of the inclusion:

$$\sum_{l=1}^{N_V} q^{l\_in} G^{kl\_in} - \sum_{l=1}^{N_V} \hat{T}^{l\_in} H^{kl\_in} = \tilde{b}_k \hat{T}^{k\_in} . \tag{2.9}$$

In these expressions, *l* is the element being integrated and *k* is the element being loaded, q^l and $\hat{T}^l$ are the heat flux and temperature at each element *l* of the outside and inside boundaries. $H^{kl} = \int_{B_l} H\left(\omega, \boldsymbol{x}_l, \boldsymbol{x}_k, \mathbf{n}_{n1}\right) \mathrm{d}B_l$ and $G^{kl} = \int_{B_l} G\left(\omega, \boldsymbol{x}_l, \boldsymbol{x}_k, \mathbf{n}_{n1}\right) \mathrm{d}B_l$ are the integration of the Green's functions for a nodal point $\boldsymbol{x}_l = \left(x_l, y_l, z_l\right)$ being integrated, subjected to a virtual heat load placed at $\boldsymbol{x}_k = \left(x_k, y_k, z_k\right)$, and B_l is the surface of boundary element *l*.

The Green's function for temperature in an unbounded medium is given by:

$$G\left(\omega, \boldsymbol{x}, \boldsymbol{x}_0\right) = \frac{e^{-\mathrm{i} k_c r_0}}{4\pi \lambda r_0} , \tag{2.10}$$

which depends on the relative distance from point $\boldsymbol{x}$ to the placement of the virtual loads $\boldsymbol{x}_0$ which is given by $r_0 = \sqrt{\left(x - x_0\right)^2 + \left(y - y_0\right)^2 + \left(z - z_0\right)^2}$. By deriving this equation, we obtain Green's function for heat flux:

$$H\left(\omega, \boldsymbol{x}, \boldsymbol{x}_0, \mathbf{n}_{n1}\right) = \frac{e^{-\mathrm{i} k_c r_0} \left(-\mathrm{i} k_c r_0 - 1\right)}{4\pi \lambda r_0^2} \frac{\partial r_0}{\partial \mathbf{n}_{n1}} . \tag{2.11}$$

In this study, the thickness of the inclusion being modelled is considered to be null, therefore the boundary integral equation is given solely by the expression in (2.6). Also, since null heat fluxes are imposed along the boundary *S*, the boundary integral equation is further reduced to:

$$b\hat{T}(\omega, \boldsymbol{x}_0) = -\int_S H(\omega, \boldsymbol{x}, \boldsymbol{x}_0, \mathbf{n}_{n1}) \hat{T}(\omega, \boldsymbol{x}) \mathrm{d}s + \hat{T}_{inc}(\omega, \boldsymbol{x}_0, \boldsymbol{x}_s) . \tag{2.12}$$

This equation cannot be solved using the conventional BEM since the final system of equations degenerates. Therefore, in order to handle the null thickness of the inclusion, the formulation can be written in terms of the normal derivative integral equation (TBEM), which is derived by applying the gradient operator to the boundary integral equation in (2.12) assuming the existence of dipole heat loads. In this case, only one side of the inclusion requires discretization. When the boundary of the inclusion is loaded with dipoles (dynamic doublets) the required integral equation is expressed as:

$$a\hat{T}(\omega,\boldsymbol{x}_0)=-\int_S \bar{H}(\omega,\boldsymbol{x},\boldsymbol{x}_0,\mathbf{n}_{n1},\mathbf{n}_{n2})\hat{T}(\omega,\boldsymbol{x})\,\mathrm{ds}+\bar{T}_{inc}(\omega,\boldsymbol{x}_0,\boldsymbol{x}_s,\mathbf{n}_{n2}), \tag{2.13}$$

in which $\bar{H}$ is obtained by applying the gradient operator to H, $\mathbf{n}_{n2}$ is the unit outward normal to the boundary at the collocation points $\boldsymbol{x}_0$, and a is null for piecewise planar boundary elements.

The Green's functions required in (2.13) take the following form:

$$\bar{H}(\omega,\boldsymbol{x},\boldsymbol{x}_0,\mathbf{n}_{n1},\mathbf{n}_{n2})=\frac{\partial H}{\partial x}\frac{\partial x}{\partial \mathbf{n}_{n2}}+\frac{\partial H}{\partial y}\frac{\partial y}{\partial \mathbf{n}_{n2}}+\frac{\partial H}{\partial z}\frac{\partial z}{\partial \mathbf{n}_{n2}}, \tag{2.14}$$

with

$$\frac{\partial H}{\partial x}(\omega,\boldsymbol{x},\boldsymbol{x}_0,\mathbf{n}_{n1})=\frac{1}{4\pi}\left\{A\left[\left(\frac{\partial r_0}{\partial x}\right)^2\frac{\partial x}{\partial \mathbf{n}_{n1}}+\frac{\partial r_0}{\partial x}\frac{\partial r_0}{\partial y}\frac{\partial y}{\partial \mathbf{n}_{n1}}+\frac{\partial r_0}{\partial x}\frac{\partial r_0}{\partial z}\frac{\partial z}{\partial \mathbf{n}_{n1}}\right]+B\left[\frac{\partial x}{\partial \mathbf{n}_{n1}}\right]\right\},$$

$$\frac{\partial H}{\partial y}(\omega,\boldsymbol{x},\boldsymbol{x}_0,\mathbf{n}_{n1})=\frac{1}{4\pi}\left\{A\left[\frac{\partial r_0}{\partial x}\frac{\partial r_0}{\partial y}\frac{\partial x}{\partial \mathbf{n}_{n1}}+\left(\frac{\partial r_0}{\partial y}\right)^2\frac{\partial y}{\partial \mathbf{n}_{n1}}+\frac{\partial r_0}{\partial y}\frac{\partial r_0}{\partial z}\frac{\partial z}{\partial \mathbf{n}_{n1}}\right]+B\left[\frac{\partial y}{\partial \mathbf{n}_{n1}}\right]\right\},$$

$$\frac{\partial H}{\partial z}(\omega,\boldsymbol{x},\boldsymbol{x}_0,\mathbf{n}_{n1})=\frac{1}{4\pi}\left\{A\left[\frac{\partial r_0}{\partial x}\frac{\partial r_0}{\partial z}\frac{\partial x}{\partial \mathbf{n}_{n1}}+\frac{\partial r_0}{\partial y}\frac{\partial r_0}{\partial z}\frac{\partial y}{\partial \mathbf{n}_{n1}}+\left(\frac{\partial r_0}{\partial z}\right)^2\frac{\partial z}{\partial \mathbf{n}_{n1}}\right]+B\left[\frac{\partial z}{\partial \mathbf{n}_{n1}}\right]\right\},$$

$$A=-\frac{k_c^{\,2}e^{-\mathrm{i}k_c r_0}}{r_0}+\frac{3\mathrm{i}k_c e^{-\mathrm{i}k_c r_0}}{r_0^{\,2}}+\frac{3e^{-\mathrm{i}k_c r_0}}{r_0^{\,3}} \text{ and } B=-\frac{\mathrm{i}k_c e^{-\mathrm{i}k_c r_0}}{r_0^{\,2}}-\frac{e^{-\mathrm{i}k_c r_0}}{r_0^{\,3}}.$$

The incident heat field in equation (2.13) is computed by:

$$\bar{T}_{inc}(\omega,\boldsymbol{x},\boldsymbol{x}_s,\mathbf{n}_{n2})=\frac{Pe^{-\mathrm{i}k_c r_s}\left(-\mathrm{i}k_c r_s-1\right)}{2\lambda r_s^{\,2}}\left(\frac{\partial r_s}{\partial x}\frac{\partial x}{\partial \mathbf{n}_{n2}}+\frac{\partial r_s}{\partial y}\frac{\partial y}{\partial \mathbf{n}_{n2}}+\frac{\partial r_s}{\partial z}\frac{\partial z}{\partial \mathbf{n}_{n2}}\right). \tag{2.15}$$

In order to solve the boundary integral equation in (2.13), the surface S is discretised into N_B planar boundary elements with one nodal point at the centre of each element. These integrations can be performed using a Gaussian quadrature scheme when the element to be integrated is not the loaded element. However, when the element being integrated is the loaded element, the integration of $\bar{H}$ leads to a hypersingular term. In order to handle these hypersingular elements, the integration can be carried out in closed form by following the procedure described next, which is based on an analytical solution proposed and validated by Tadeu *et al.* [26].

Considering a rectangular hypersingular element with width W in the x direction and length L in the z direction, and with the axes origin at its centre (see Figure 2.5), the integration $\int_{-L/2}^{L/2}\int_{-W/2}^{W/2} \overline{H}(\omega, \boldsymbol{x}, \boldsymbol{x}_0, \mathbf{n}_{n1}, \mathbf{n}_{n2})\,\mathrm{d}x\,\mathrm{d}z$ leads to a hypersingular term when $\mathbf{n}_{n2} = \mathbf{n}_{n1}$.

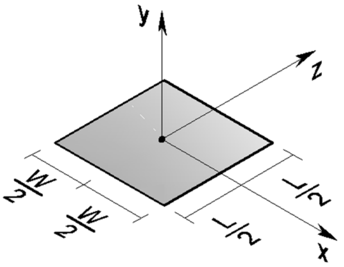

Figure 2.5: Scheme of a planar boundary element.

In a system where the geometry is constant along one of the directions, it is possible to pose the 3D heat diffusion problem as a sum of 2D problems with different spatial wavenumbers along that direction. In this case, the 3D Green's functions can be written as a sum of 2D solutions for line heat sources whose amplitudes vary sinusoidally in the direction of the z axis. This is accomplished by applying a spatial Fourier transform along the z direction to 3D Green's functions, leading to:

$$\hat{G}(\omega,x,y,x_0,y_0,k_z)=\frac{-\mathrm{i}}{8\pi\lambda}\mathrm{H}_0\left(k\bar{r}_0\right), \tag{2.16}$$

in which $\mathrm{H}_\alpha\left(\ \right)$ are Hankel functions of the second kind and order α, $k=\sqrt{-\mathrm{i}\omega/K-k_z^2}$ where $\mathrm{Im}\left(k\right)<0$ and k_z is the wavenumber in the z direction, and $\bar{r}_0=\sqrt{\left(x-x_0\right)^2+\left(y-y_0\right)^2}$.

By deriving the former equation, the following is obtained:

$$\hat{H}(\omega,x,y,x_0,y_0,\mathbf{n}_{n1},k_z)=\frac{\mathrm{i}k}{8\pi\lambda}\mathrm{H}_1\left(k\bar{r}_0\right)\left(\frac{\partial\bar{r}_0}{\partial x}\frac{\partial x}{\partial\mathbf{n}_{n1}}+\frac{\partial\bar{r}_0}{\partial y}\frac{\partial y}{\partial\mathbf{n}_{n1}}\right). \tag{2.17}$$

Assuming the presence of an infinite set of equally spaced virtual heat sources in the *z* direction, the 3D Green's function for heat flux can be written as:

$$H(\omega,\boldsymbol{x},\boldsymbol{x}_0,\mathbf{n}_{n1})=\frac{2\pi}{L_{vs}}\sum_{m=-\infty}^{\infty}\hat{H}(\omega,x,y,x_0,y_0,\mathbf{n}_{n1},k_z)\,e^{-\mathrm{i}k_{zm}z}\,, \tag{2.18}$$

where $k_{zm}=\left(2\pi/L_{vs}\right)m$ and L_{vs} is the spacing between virtual heat sources, which must be big enough so as to avoid spatial contamination. The influence of neighbouring virtual heat sources is further reduced by the use of complex frequencies.

Equation (2.18) converges and can be approximated by a finite sum of terms. The 3D Green's function $\bar{H}$ can then be obtained by applying the gradient operator to *H*, leading to the following expression:

$$\bar{H}\left(\omega,x,y,x_0,y_0,\mathbf{n}_{n1},\mathbf{n}_{n2},k_z\right)=\frac{\mathrm{i}\,k}{8\pi\lambda}\left[-k\,\mathrm{H}_2\left(k\,\bar{r}_0\right)\left(\frac{\partial\bar{r}_0}{\partial x}\frac{\partial x}{\partial\mathbf{n}_{n1}}+\frac{\partial\bar{r}_0}{\partial y}\frac{\partial y}{\partial\mathbf{n}_{n1}}\right)^2+\frac{\mathrm{H}_1\left(k\,\bar{r}_0\right)}{\bar{r}_0}\right]. \tag{2.19}$$

This allows the integration of the hypersingular element to be obtained by:

$$\int_{-L/2}^{L/2}\int_{-W/2}^{W/2}\bar{H}\left(\omega,\boldsymbol{x},\boldsymbol{x}_0,\mathbf{n}_{n1},\mathbf{n}_{n2}\right)\mathrm{d}x\,\mathrm{d}z=\frac{2\pi}{L_z}\sum_{m=-M}^{M}\int_{-L/2}^{L/2}I(k\bar{r}_0)\,e^{-\mathrm{i}k_{zm}z}\mathrm{d}z\,, \tag{2.20}$$

in which,

if m=0:

$$\int_{-L/2}^{L/2}I(k\bar{r}_0)\,e^{-\mathrm{i}k_{zm}z}\mathrm{d}z=L\int_{-W/2}^{W/2}\frac{\mathrm{i}\,k}{8\pi\lambda}\left[-k\,\mathrm{H}_2\left(k\,\bar{r}_0\right)\left(\frac{\partial\bar{r}_0}{\partial x}\frac{\partial x}{\partial\mathbf{n}_{n1}}+\frac{\partial\bar{r}_0}{\partial y}\frac{\partial y}{\partial\mathbf{n}_{n1}}\right)^2+\frac{\mathrm{H}_1\left(k\,\bar{r}_0\right)}{\bar{r}_0}\right]\mathrm{d}x\,,$$

if m ≠ 0:

$$\int_{-L/2}^{L/2}I(k\bar{r}_0)\,e^{-\mathrm{i}k_{zm}z}\mathrm{d}z=\frac{2\sin(k_{zm}\,L/2)}{k_{zm}}\int_{-W/2}^{W/2}\frac{\mathrm{i}\,k}{8\pi\lambda}\left[-k\,\mathrm{H}_2\left(k\,\bar{r}_0\right)\left(\frac{\partial\bar{r}_0}{\partial x}\frac{\partial x}{\partial\mathbf{n}_{n1}}+\frac{\partial\bar{r}_0}{\partial y}\frac{\partial y}{\partial\mathbf{n}_{n1}}\right)^2+\frac{\mathrm{H}_1\left(k\,\bar{r}_0\right)}{\bar{r}_0}\right]\mathrm{d}x\,.$$

The integration of $I(k\overline{r}_0)$ can be performed indirectly by isolating a semi-cylinder just above the boundary element and by considering its thermal equilibrium, which leads to:

$$I(k\overline{r}_0) = \frac{\mathrm{i}k^2}{4\pi\lambda}\left[\int_0^{W/2} \mathrm{H}_0\left(k\,\overline{r}_0\right)\mathrm{d}\overline{r}_0 - \frac{1}{k}\mathrm{H}_1\left(k\frac{W}{2}\right)\right]. \tag{2.21}$$

2.3.4 Phase contrast

Phase results are computed directly in the frequency domain. Frequency domain temperature responses are computed considering harmonic sources with unitary amplitude, which corresponds to assuming an ideal Dirac pulse in the time domain, that, in turn, has an infinite flat spectrum in the frequency domain. Thermal wave phase is given by the arctangent of the imaginary part of the frequency domain temperature response divided by the real part.

In IRT tests, phase contrast is the term that refers to the difference between phase recorded in a defective zone and a sound (without defects) area of the thermal image. While in real experiments a sound zone needs to be selected to be used as a reference, in this numerical study the thermal wave phase can be computed for any point in a medium without defects. Hence two calculations are performed, for a medium with defects and for a medium without defects, and phase contrast is given by the difference between the two, which is expressed by the following:

$$\Delta\phi\left(\omega,\boldsymbol{x}\right) = \phi_d\left(\omega,\boldsymbol{x}\right) - \phi_s\left(\omega,\boldsymbol{x}\right) \tag{2.22}$$

in which $\Delta\phi\left(\omega,\boldsymbol{x}\right)$ is phase contrast, $\phi_d\left(\omega,\boldsymbol{x}\right)$ is phase anywhere in a defective medium and $\phi_s\left(\omega,\boldsymbol{x}\right)$ is phase anywhere in a sound medium.

Additionally, a graphical representation of the variation of the phase contrast response for one pixel in the thermal image along the frequency spectrum is known as a phase contrast curve. As mentioned, these can be used to characterize defects and their interpretation and comparison can provide useful information.

2.3.5 Temperature in time

Unlike thermal wave which is computed directly, time domain temperature results are obtained by applying an inverse fast Fourier transform to the temperature response calculated in the frequency domain.

The problem of aliasing occurring is minimized by introducing complex frequencies with a small imaginary part into the computations. These take the form $\omega_c = \omega - \mathrm{i}\eta$ where $\eta = 0.7\Delta\omega$ and the frequency step is $\Delta\omega$. Then, in order to reverse this, an exponential window is used in the time domain by applying $e^{\eta t}$ to the response.

The heat source is allowed to have any time variation and the frequency domain solution can range from 0.0 Hz to quite high frequencies. However, generally there is no need to compute the highest frequencies in the range since the response falls rapidly for higher frequencies. The null frequency (0.0 Hz) corresponds to the static response. The computation of this response is possible due to the use of complex frequencies since the argument of the Hankel functions in the integral equations is $-\mathrm{i}\eta$, which is different than zero.

2.4 Verification of the 3D TBEM solution

The verification of the proposed algorithm was performed using a circular cylindrical cavity for which analytical solutions are known, using a mirror image source technique to enable a comparison between the proposed 3D TBEM model results and analytically generated results.

Consider the cavity in Figure 2.6 which has radius r_c and length L_t aligned along the direction of the z axis. This inclusion is subjected to a 3D heat source placed at $\boldsymbol{x}_s = (x_s, y_s, z_s)$ and null heat fluxes are prescribed all along its boundary. The length of the cavity is limited by enforcing null heat fluxes at sections $z = 0.0$ m and $z = L_t$.

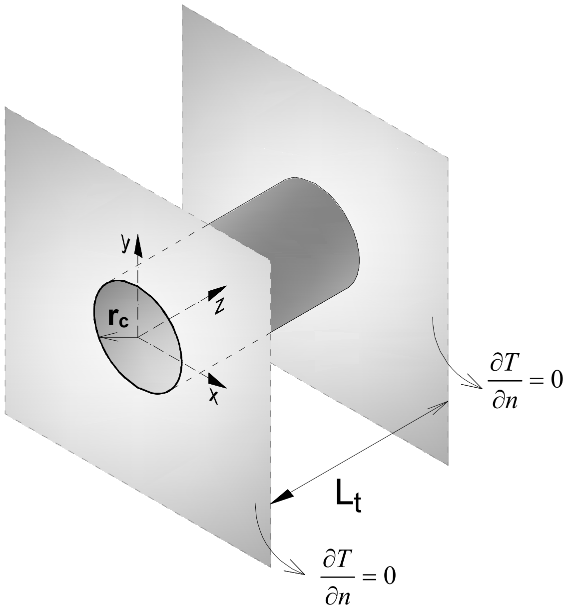

Figure 2.6: Cylindrical inclusion in an unbounded medium.

Since the cylindrical inclusion being modelled has a geometry which is constant along the direction of the *z* axis, the 3D problem may be written as a sum of 2D solutions with a varying spatial wavenumber in the direction *z*. The analytical solution for the problem is therefore obtained by applying a spatial Fourier transform in the *z* direction to the 3D Green's functions.

The imposition of null normal heat flux at sections $z = 0.0$ m and $z = L_t$ is obtained by adding to the field generated by the heat source a heat field produced by virtual sources which are located in the *z* direction in such a way that they act as mirrors of the real source and, therefore, guarantee the required boundary condition of null heat fluxes.

In this case, the heat field can be expressed as:

$$T(\omega,\boldsymbol{x},\boldsymbol{x}_s)=\frac{2\pi}{L_{vs}}\sum_{m=-\infty}^{\infty}\left[\hat{T}(\omega,x,y,x_s,y_s,k_{zm})\left(e^{-\mathrm{i}k_{zm}z_{m0}}+\sum_{m=1}^{N_S}\sum_{j=1}^{4}e^{-\mathrm{i}k_{zm}z_{mj}}\right)\right], \tag{2.23}$$

where again $k_{zm}=\left(2\pi/L_{vs}\right)m$, L_{vs} is the distance between virtual heat sources, and $z_{m0}=z-z_s$, $z_{m1}=z+z_0-2L_t m$, $z_{m2}=z+z_0+2L_t\left(m-1\right)$, $z_{m3}=z-z_0-2L_t m$ and $z_{m4}=z-z_0+2L_t m$.

The number of virtual sources N_S used is such that it allows for the signal response to be correctly computed after reaching a small variation threshold. Each 2D problem is solved using the separation of variables procedure for the Helmholtz equation and by enforcing the boundary conditions along the surface using the Bessel series form.

Considering that the axes origin is located at the centre of the circle defined by the cross section of the cylinder, and that the source is placed somewhere along the *x* axis, the following equation is obtained:

$$\hat{T}(\omega,x,y,x_s,y_s,k_z) = -\frac{\mathrm{i}}{4\lambda}\mathrm{H}_0(k\bar{r}_0) + \sum_{\alpha=0}^{\infty} A_\alpha \mathrm{H}_\alpha(k\bar{r})\cos(\alpha\theta), \tag{2.24}$$

in which $A_\alpha = \dfrac{\dfrac{\mathrm{i}}{4\lambda}(-1)^\alpha \beta_\alpha \mathrm{H}_\alpha(k\bar{r}_{00})\left[\dfrac{\alpha}{r_c}\mathrm{J}_\alpha(kr_c) - k\,\mathrm{J}_{\alpha+1}(kr_c)\right]}{\left[\dfrac{\alpha}{r_c}\mathrm{H}_\alpha(kr_c) - k\,\mathrm{H}_{\alpha+1}(kr_c)\right]}$, $\bar{r} = \sqrt{x^2+y^2}$, and $\theta = \arctan\left(x/y\right)$

where $\mathrm{J}_\alpha(\ldots)$ are Bessel functions of order *α*, $\bar{r}_{00} = |x_0|$ and $\beta_\alpha = 1$ if $\alpha = 0$ or $\beta_\alpha = 2$ otherwise.

Temperature responses are computed for a cylindrical inclusion with radius $r_c = 0.5$ m and $L_t = 2.0$ m. The 3D point heat source is placed at (−1.5, 0.0, 1.0) m. The thermal properties assigned to the medium are: c = 780.0 J/(kg.°C), ρ =1860.0 kg/m^3 and λ = 0.72 W/(m.°C). L_{vs} is assumed to be 60.0 m. Computations are performed for a frequency step of $\Delta f = 0.5\times10^{-7}$ Hz in a frequency range that goes from 0.0 Hz to 1×10^{-5} Hz. The responses are computed for complex frequencies $\omega_c = \omega - \mathrm{i}\eta$ (with $\eta = 0.7\Delta\omega$ and $\Delta\omega = 2\pi\,\Delta f$).

Results were calculated both analytically and using the 3D TBEM formulation proposed. To further understand the performance of the two solutions, two different amounts of boundary elements were used to discretise the inclusion: 30×20 (20 in the *z* direction) and 50×32 (32 in the *z* direction).

Figure 2.7 shows the real and imaginary parts of the analytical response at a receiver located at (−0.8, 0.0, 1.0) m and illustrates the error when the problem is solved using the proposed 3D TBEM algorithm.

From the results shown in Figure 2.7 it can be observed that the solution improves as the number of boundary elements increases.

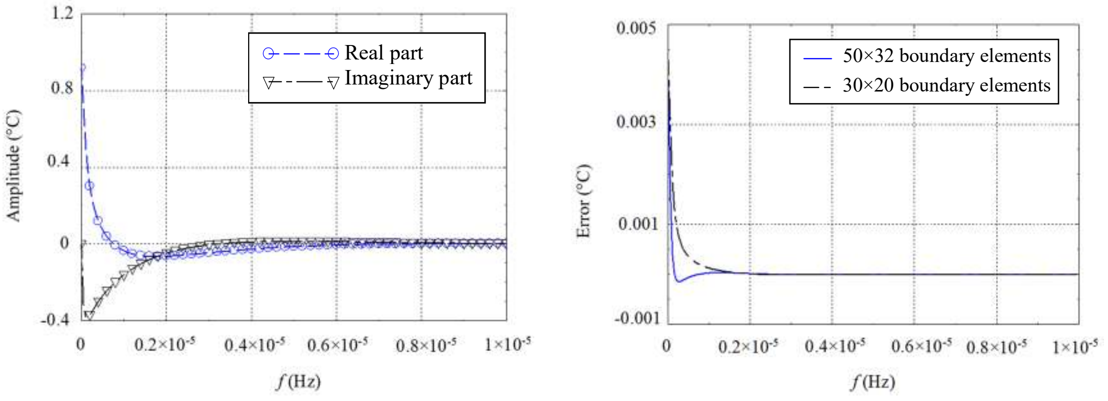

a) b)

Figure 2.7: Verification results: a) analytical response; b) error obtained using the 3D TBEM considering different amounts of boundary elements.

2.5 Numerical application results

In order to illustrate the applicability and usefulness of the proposed solution for defect characterization studies using active IRT, the model was used to simulate 3D heat diffusion around a null thickness planar inclusion embedded in an unbounded solid isotropic medium. Several variations of an initial case study, in which defect characteristics and test parameters are varied, were computed in order to study the influence that changing such parameters can have on the computed heat field. In particular, the defect's size, geometry, location and position, as well as the placement of the heat source were changed in the simulations. In this section, first the initial case study used for the application is presented and then the simulation results for transient heat field and phase contrast are reported and discussed for each variation of the case study modelled.

2.5.1 Initial case study

Figure 2.8 illustrates a null thickness inclusion located within an unbounded isotropic solid medium and provides a representation of the grid of receivers for which the results were computed. Responses were obtained for three fine grids of receivers: two grids (G1 and G2) which are placed parallel to the *yz* plane and another (G3) which is parallel to *xy* plane. In this system, the grid of receivers G1 corresponds to the hypothetical surface of an object from which thermographic data recorded in IRT test are obtained.

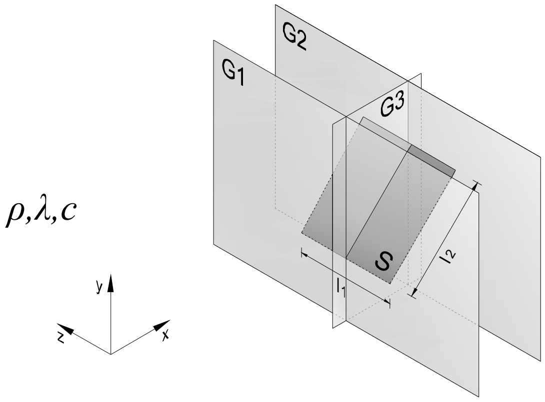

Figure 2.8: 3D view of the system modelled.

The thermal properties of the medium are $\rho = 2300.0$ kg/m^3, $\lambda = 1.4$ W/(m.°C) and $c = 880.0$ J/(kg.°C). Grid G1 is placed at $x = 0.5325$ m and G2 is placed at $x = 0.6725$ m. Both are parallel to the yz plane and to the defect. G1 and G2 are 0.6×0.4 m^2 and each have 6565 receivers spaced at equal intervals of $\Delta y = 0.00625$ m and $\Delta z = 0.006$ m. G3 is 0.2×0.4 m^2 and has its 2665 receivers spaced at equal intervals of $\Delta x = 0.005$ m and $\Delta y = 0.00625$ m. The inclusion is discretized into 800 elements: 20 along the y axis direction by 40 in the z direction. The heat source which is placed at the origin of the axes is either a 3D point heat source or a 1D planar heat source.

Consider that initially the defect is a 0.2×0.2 m^2 plane which is placed vertically (parallel to the yz plane) with its centre at (0.6, 0.0, 0.0) m. This initial case study is represented in Figure 2.9.

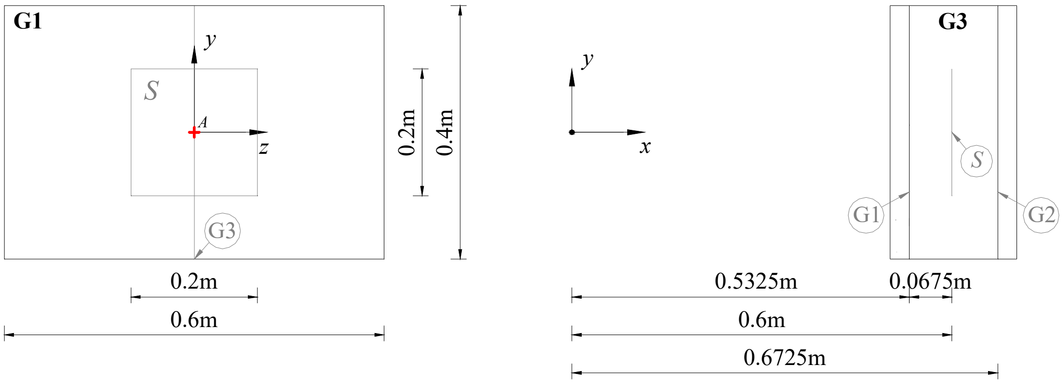

a) b)

Figure 2.9: Geometry of the system modelled: a) front view with placement of receiver A; b) vertical cross section.

Figure 2.9 a) represents a front view of the system, facing the grid that corresponds to an object's surface, and includes a specific receiver A located at (0.5325, 0.0, 0.0) m. Figure 2.9 b) illustrates a vertical cross section of the system modelled.

Heat field results

Following the procedure described in section 2.3.5 of this chapter, computations were performed in the frequency range of 0.0 Hz to 1.024×10^{-3} Hz, using an increment of $\Delta f = 0.5\times10^{-6}$ Hz, which corresponds to a total time window available for analysis of 555.56 h. This frequency range was selected in a way that ensures a negligible contribution from the frequencies above a defined threshold. The imaginary part of the frequency is defined by $\eta = 0.7\Delta\omega$ and $\Delta\omega = 2\pi\,\Delta f$.

The medium was assumed to be initially at a temperature of 20.0 °C. The source emitted energy from instant $t = 0.5$ h to $t = 1.5$ h following a rectangular heating function with amplitude P. This amplitude was defined so that the maximum temperature increase recorded at the centre of grid G1 (receiver A) in the medium without defects is 15.0 °C. This resulted in an amplitude of $P = 1843.2$ in the case of stimulation considering a 3D point energy source, and $P = 2015.9$ in the case of a 1D planar heat source.

In order to illustrate the temperature pattern disturbances observed in IRT experiments, transient temperature computations were performed twice, once for any point of the defective medium and then for any point of a sound medium in which the defect is absent. The responses are shown in Figure 2.10 and Figure 2.11. In both figures the results on the left are for the case when there is a defect within the medium, while the central plot shows the results obtained when the medium is sound (no defect). The difference between the two results is given in the plot on the right. Figure 2.10 shows a snapshot of the time domain temperature distribution recorded on the grids of receivers (G1, G2 and G3), obtained when the system is modelled considering a 3D point source located at $\left(x_s, y_s, z_s\right)$= (0.0, 0.0, 0.0) m while Figure 2.11 corresponds to the results obtained for a 1D planar heat source located at x_s = 0.0 m.

Both Figure 2.10 and Figure 2.11 were taken at the instant when the thermal response peaked. This corresponds to the moment when, in the sound medium, a temperature of 35 °C was recorded at receiver A (see Figure 2.9). It is visible that both heat sources were able to produce significant temperature differences as a result of the presence of the defect. However, the thermal pattern observed in the two cases is different. It can be said that a 3D point heat source produced a more concentrated thermal response, while the 1D planar source gave a more disperse response. Furthermore, the temperature difference generated by the 3D source was more significant and made the defect more visible.

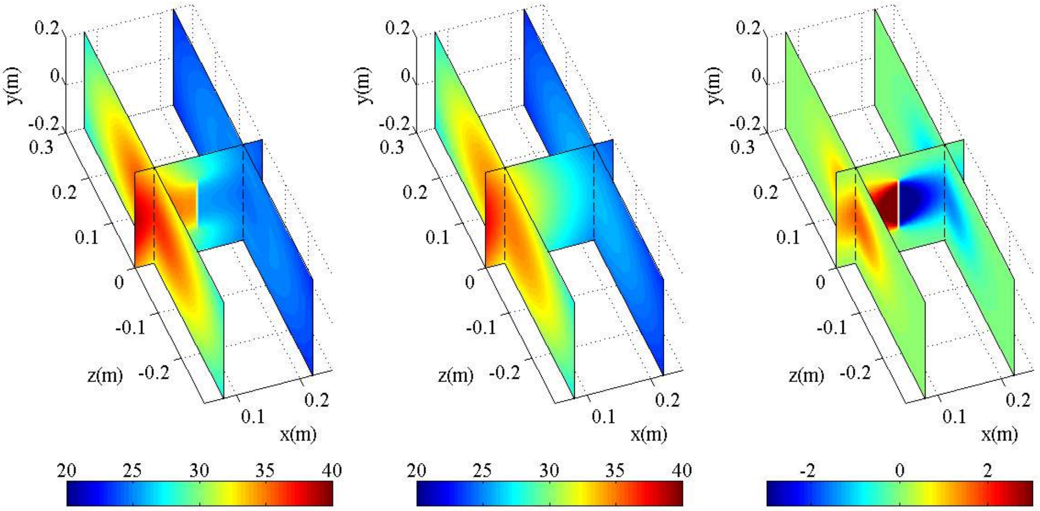

a) b) c)

Figure 2.10: Snapshot of the temperature distribution, in °C, taken at $t = 20$ h in a medium subjected to a 3D heat source containing a 0.2×0.2 m^2 vertical inclusion: a) defect is present; b) medium is without any defects; c) difference between results obtained in a) and b).

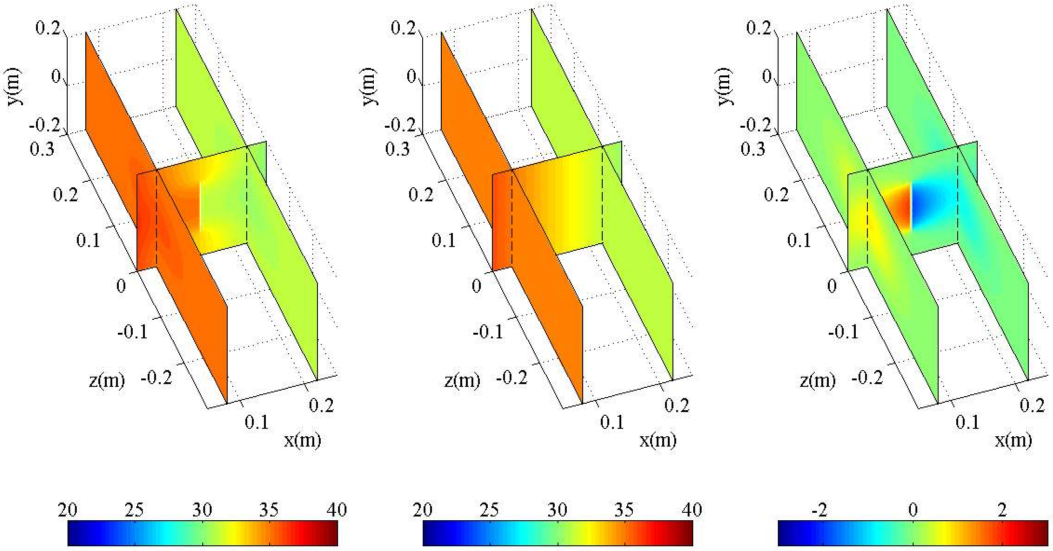

a) b) c)

Figure 2.11: Snapshot of the temperature distribution, in °C, taken at $t = 58$ h in a medium subjected to a 1D heat source containing a 0.2×0.2 m^2 vertical inclusion: a) defect is present; b) medium is without any defects; c) difference between results obtained in a) and b).

Phase contrast results

The curves presented in Figure 2.12 show the phase contrast results obtained for the receiver located at the centre of grid G1 (receiver A) for this initial case study, when subjected to either a 3D point heat source or a 1D planar heat source. Calculations were performed according to the procedure explained in 2.3.4.

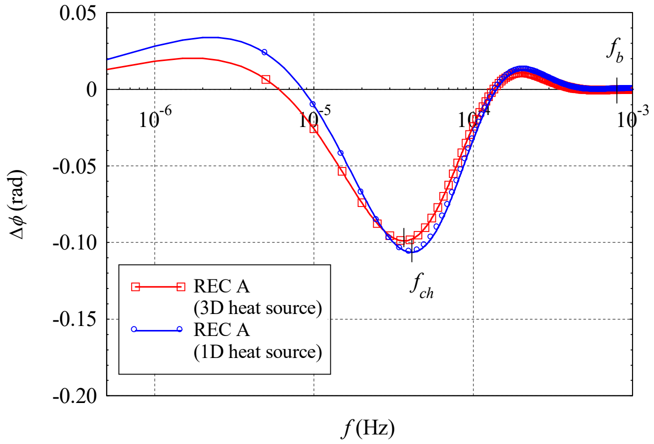

Figure 2.12: Phase contrast curves obtained in receiver A for a 0.2×0.2 m^2 vertical inclusion subjected to a 3D and a 1D heat source.

Both these curves show a defined peak in the frequency spectrum. The frequency that corresponds to this peak of maximum absolute phase contrast ($|\Delta\phi_{\max}|$) is known in defect detection studies as the characteristic frequency (f_{ch}). Then, at a certain frequency the phase contrast amplitude becomes null. This frequency, which is often referred to as the blind frequency (f_b) indicates the defect detection threshold in the frequency domain.

Even though the characteristic frequency and maximum absolute phase contrast values shown in Figure 2.12 for the 3D and 1D heat sources are not identical – maximum phase contrast was slightly higher when the planar heat source was considered – it can be said that they are very approximate, indicating that, for this case study, the characteristic frequency of the defect might not be heavily influenced by the consideration of a point or planar heat source. Also, the blind frequency did not change significantly, and consequently neither did the detection threshold of the defect.

Figure 2.13 and Figure 2.14 contain snapshots of phase contrast images computed for the grid of receivers G1 for the 0.2×0.2 m^2 vertical defect. The image in the central plot was obtained at the frequency which corresponds to maximum phase contrast obtained at receiver A, the characteristic frequency ($f_{ch}^{A} = 3.70\times10^{-5}$ Hz for the 3D source and $f_{ch}^{A} = 4.10\times10^{-5}$ Hz for the 1D source). The images on the left and right correspond to frequencies which were randomly selected to illustrate the evolution of the phase contrast image along the frequency spectrum.

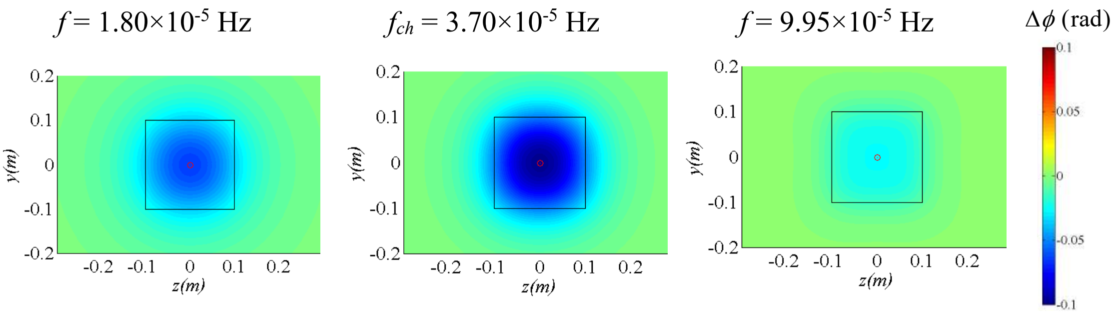

$$\Delta\phi_{\max}^{A} = -9.89\times10^{-2} \text{ rad}$$

Figure 2.13: Phase contrast images of grid G1 for a 0.2×0.2 m^2 vertical inclusion subjected to a 3D heat source taken at several frequencies.

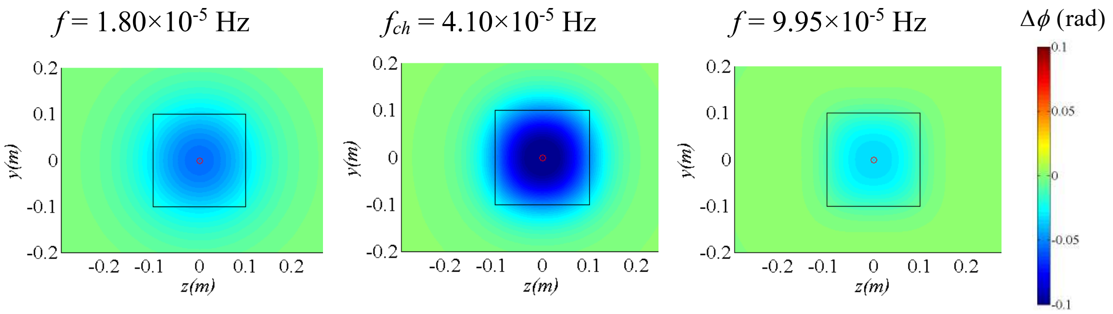

$$\Delta\phi_{\max}^{A} = -1.06\times10^{-1} \text{ rad}$$

Figure 2.14: Phase contrast images of grid G1 for a 0.2×0.2 m^2 vertical inclusion subjected to a 1D heat source taken at several frequencies.

For both the planar and point sources, the phase contrast snapshots demonstrate the ability to detect the presence of the defect. It can also be clearly seen that outside the limits of the defect phase contrast tends to zero because the effect of the reflected heat field is diminished.

2.5.2 Influence of defect size and shape

In order to assess the influence of the dimensions of the defect on temperature distribution and phase contrast, three other defect sizes were considered: 0.1×0.1 m^2; 0.3×0.3 m^2 and 0.05×0.2 m^2.

Each inclusion was discretized into a total of 800 elements (20 along the y axis direction by 40 in the z axis direction): 0.05×0.2 m^2 (spaced by $\Delta y = 0.0025$ m and $\Delta z = 0.005$ m); 0.1×0.1 m^2 ($\Delta y = 0.005$ m and $\Delta z = 0.0025$ m); 0.2×0.2 m^2 ($\Delta y = 0.01$ m and $\Delta z = 0.005$ m) and 0.3×0.3 m^2 ($\Delta y = 0.015$ m and $\Delta z = 0.0075$ m).

To further comprehend how the geometry of each defect affects the results, specific receivers placed at the extremities of different sized defects were selected for analysis: receiver B at (0.5325, 0.0, 0.1) m; receiver C at (0.5325, 0.0, 0.2) m; receiver D at (0.5325, 0.0, 0.3) m; receiver E at (0.5325, 0.1, 0.1) m and receiver F at (0.5325, 0.2, 0.2) m.

Figure 2.15 a) shows a front view of the case study system with the different defect sizes that were considered, as well as the specific placement of receivers A to F. Figure 2.15 b) illustrates a vertical cross section of the system modelled. In addition to these geometries, an inclusion with infinitely large dimensions in two directions was also simulated. This was achieved by means of a mirror image source technique, in which an additional virtual source is placed in the domain to act as a mirror image of the real source in relation to the surface of the inclusion. This infinitely sized inclusion is henceforth referred to as the reference curve.

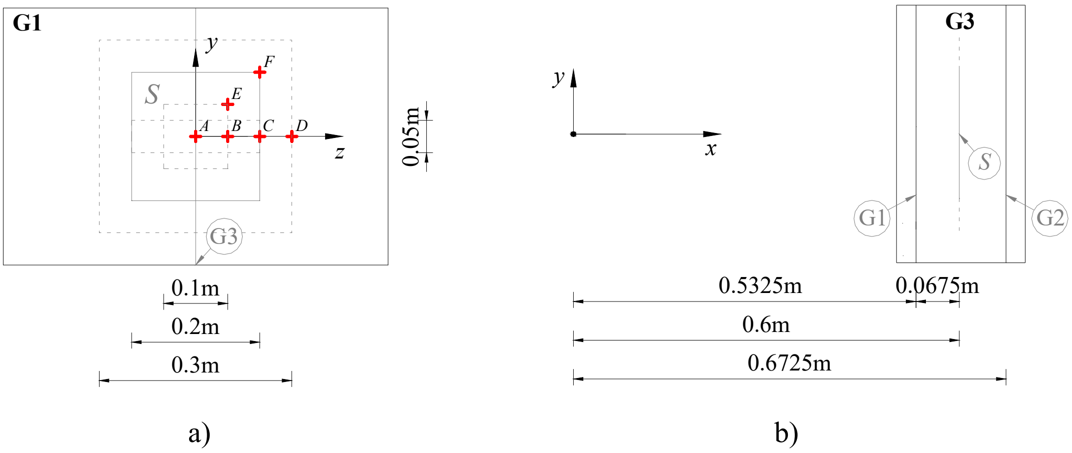

Figure 2.15: Geometry of the system modelled: a) front view with placement of receiver A to F; b) vertical cross section.

Heat field results

Figure 2.16 contains several snapshots of the transient temperature obtained for a defective medium, considering the different defect sizes. In these snapshots, it is evidenced that changing the geometry of a defect highly influences the heat field. The larger the defect being modelled, the more energy is concentrated between the surface (G1) and the defect.

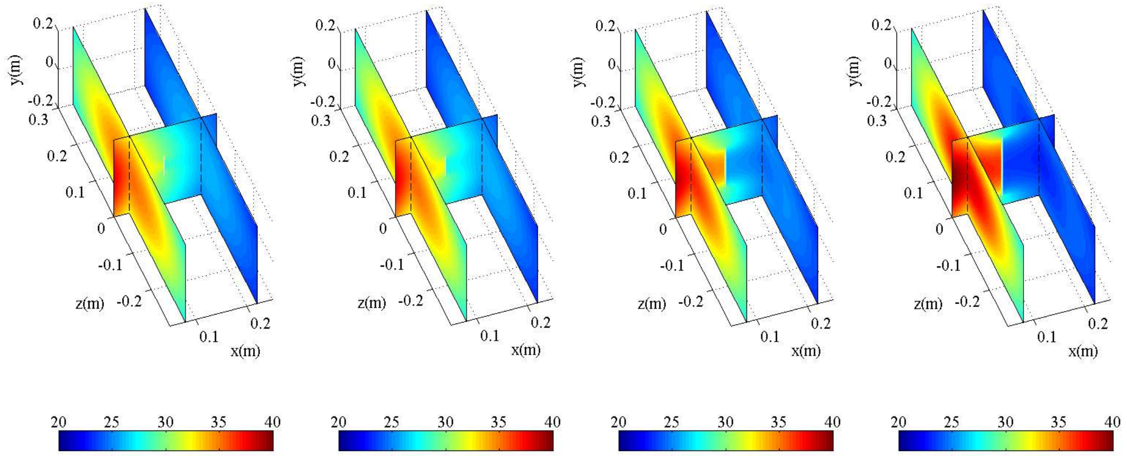

a) b) c) d)

Figure 2.16: Snapshot taken at $t = 20$ h of the temperature distribution, in °C, in a defective medium subjected to a 3D point heat source containing a defect with dimensions of: a) 0.05×0.2 m^2; b) 0.1×0.1 m^2; c) 0.2×0.2 m^2 and d) 0.3×0.3 m^2.

Phase contrast results

The graphs in Figure 2.17 and Figure 2.18 show the phase contrast curves obtained at receivers A and D (see Figure 2.15 a)) for the four different sizes, as well as for the infinitely sized defect (curve REF).

These results show that, as size of the defect increases, there is a decrease in the characteristic frequency f_{ch} and an increase in the corresponding absolute maximum phase contrast value $\left|\Delta\phi_{\max}\right|$. Figure 2.17 also shows that the amplitude of phase contrast decreases when the shape of the inclusion changes from the 0.1×0.1 m^2 to the 0.05×0.2 m^2 geometry one. As expected, as size increases, results become closer to those obtained for the infinite sized defect defined by curve REF. In no case does the blind frequency f_b suffer significant alterations, hence it can be said that the detection threshold changes very little with the variation of size.

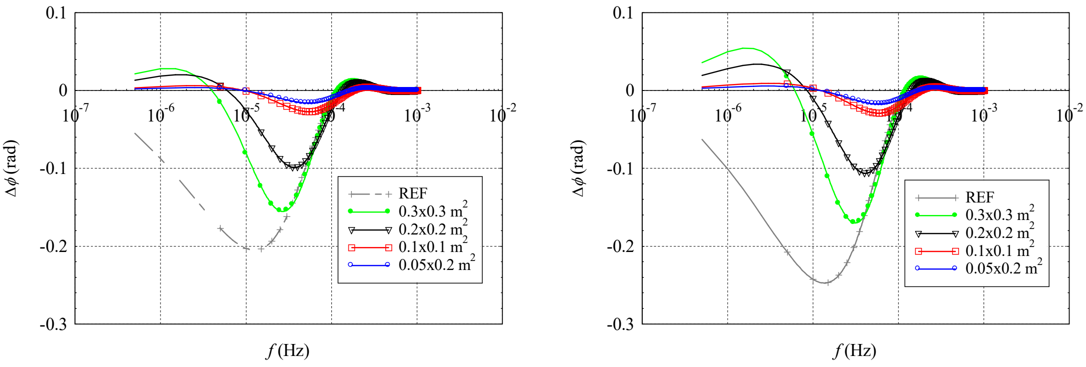

a) b)

Figure 2.17: Phase contrast curves obtained for receiver A, for a defect with varying size embedded in a medium subjected to a: a) 3D point heat source; b) 1D heat source.

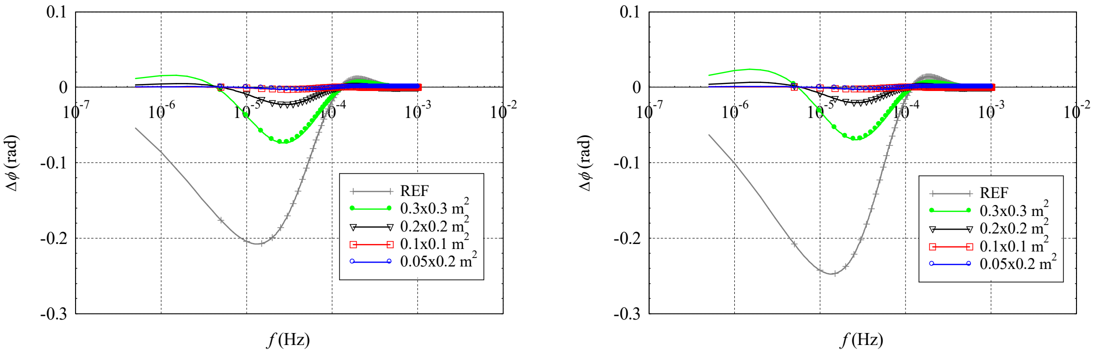

a) b)

Figure 2.18: Phase contrast curve results obtained for receiver D for a defect with varying size embedded in a medium subjected to a: a) 3D point heat source; b) 1D heat source.

By comparing Figure 2.17 with Figure 2.18 it may be said that the maximum phase contrast is slightly greater when subjected to a planar heat source and that, as size increases, so does this difference between point and planar sources. As shown in Figure 2.18, for receiver D (placed outside the limits of the 0.05×0.2 m^2, 0.1×0.1 m^2, and 0.2×0.2 m^2), phase contrast is significantly reduced for receivers which are placed outside the limits of the defect under study, indicating the potential that phase contrast curves have for detecting and outlining a defect's boundaries.

Figure 2.19 illustrates these results in terms of phase contrast images by containing snapshots of phase contrast computed at the grid of receivers G1 for defects with varying size (0.05×0.2 m^2, 0.1×0.1 m^2, 0.2×0.2 m^2 and 0.3×0.3 m^2) placed within a medium subjected to a 3D point heat source. These snapshots are taken at three different frequencies which correspond to the maximum phase contrast $|\Delta\phi_{\max}|$ obtained for receiver A (the peaks in the curves shown in Figure 2.17 a) for the cases of 0.1×0.1 m^2 ($f_{ch} = 5.5\times10^{-5}$ Hz), 0.2×0.2 m^2 ($f_{ch} = 3.7\times10^{-5}$ Hz) and 0.3×0.3 m^2 ($f_{ch} = 2.7\times10^{-5}$ Hz) defects. The characteristic frequency for the 0.05×0.2 m^2 defect is not pictured here because it is 5.45×10^{-5} Hz, which is very near to the one obtained for the 0.1×0.1 m^2 defect.

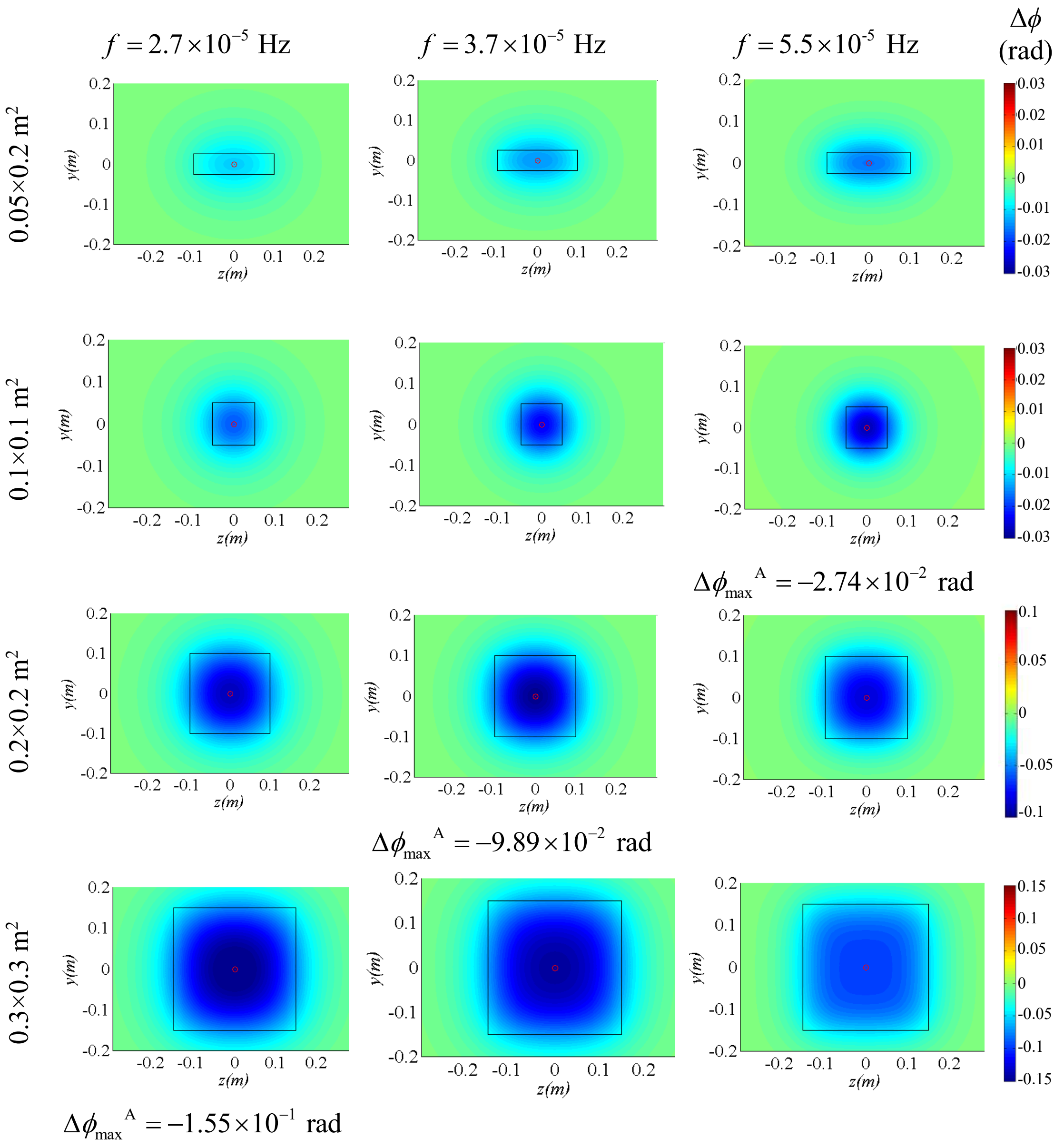

Figure 2.19: Snapshots of phase contrast images computed for the grid of receivers G1 for different size defects contained in a medium subjected to 3D heat source taken at several frequencies.

The images in Figure 2.19 clearly illustrate how results are strongly influenced by the size of the defect, confirming the potential for defect characterization using IRT. The snapshots for the results obtained in the case of the system subjected to a 1D planar source are not shown here since their appearance is very similar.

2.5.3 Influence of defect position

In order to study the influence that the position of the defect has on heat diffusion, the initial 0.2×0.2 m^2 defect was rotated 15° and 40° on an axis that is parallel to the *z* direction and intersects the centre of the defect. The tilt angle α and the rotation axis are represented in the cross section in Figure 2.20 b).

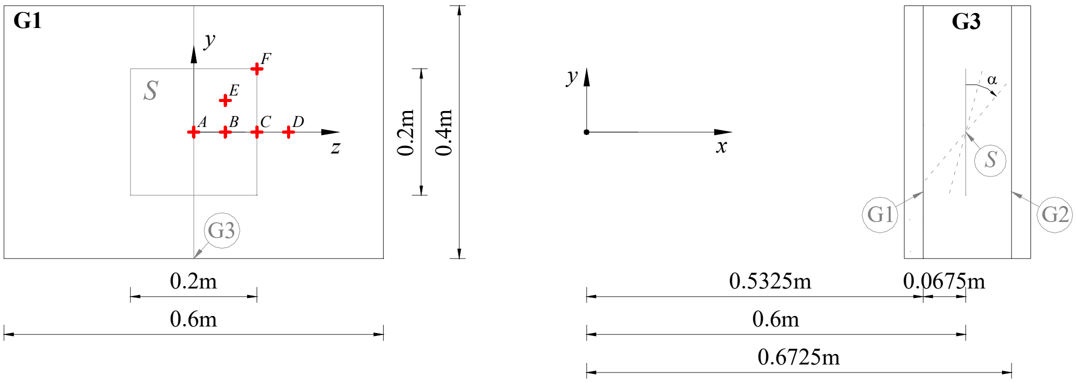

a) b)

Figure 2.20: Geometry of the system modelled: a) front view with placement of receiver A to F; b) vertical cross section.

The graphs in Figure 2.21 give the phase contrast curves obtained for the receiver E for three different tilt angles: $\alpha = 0°$; $\alpha = 15°$ and $\alpha = 40°$. Figure 2.22 shows phase contrast results recorded at receiver F. Again, results were computed considering both a point and a planar heat source.

When comparing heat sources, the graphs in Figure 2.21 and Figure 2.22 reveal similar characteristic and blind frequency results. In receiver E, located in front of the upper part of the defect, the maximum phase contrast is slightly greater for the planar heat source. In receiver F, the peak phase contrast occurs at higher characteristic frequency.

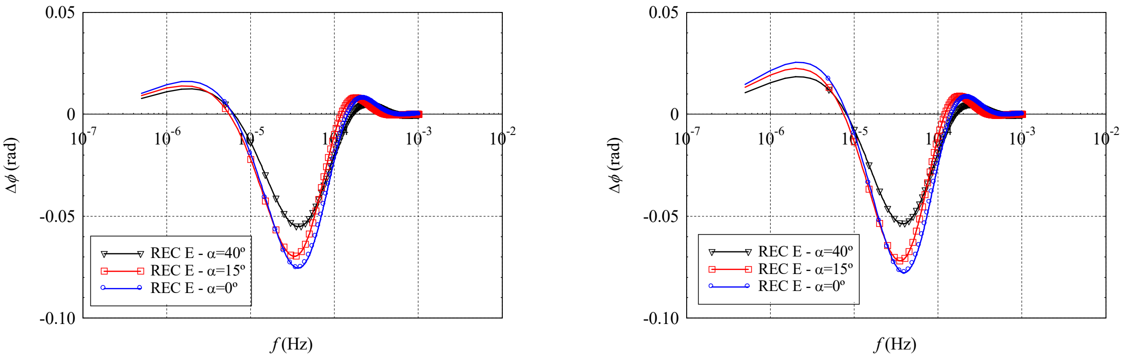

a) b)

Figure 2.21: Phase contrast curves obtained for receiver E for a 0.2×0.2 m^2 tilted defect subjected to a: a) 3D point heat source; b) 1D heat source.

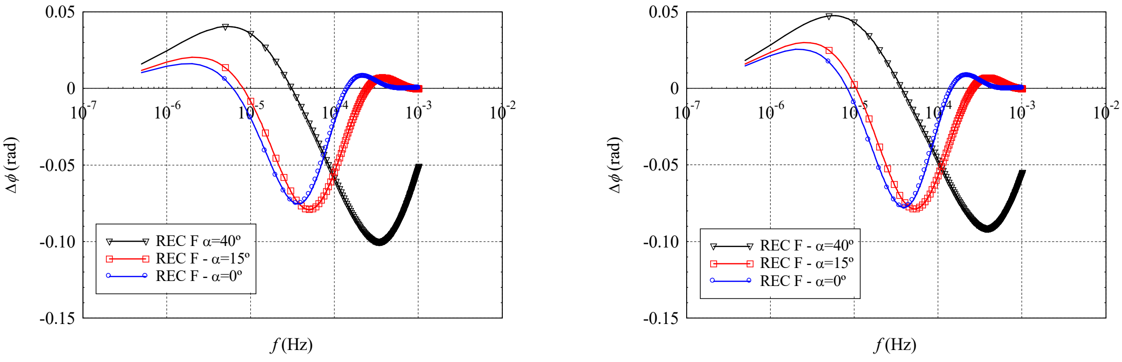

a) b)

Figure 2.22: Phase contrast curves obtained for receiver F for a 0.2×0.2 m^2 tilted defect subjected to a: a) 3D point heat source; b) 1D heat source.

Figure 2.23 shows the phase contrast images recorded at the grid of receivers G1 for the 0.2×0.2 m^2 defect tilted 15° and 40° on its rotation axis (see Figure 2.20 b)) for the case in which the system is subjected to a 3D heat source. Snapshots were taken at three different frequencies corresponding to the maximum phase contrast recorded at either receiver E or F. The images show that, as the defect is tilted, the amplitude of phase contrast is reduced at the lower frequencies and the maximum phase contrast occurs at higher frequencies. Furthermore, as seen for $\alpha = 40°$, the positive phase contrast is recorded at receiver F for more of the lower frequencies.

Again the snapshots for the case of the 1D heat source are not presented here because they look be very similar to the ones shown in Figure 2.23.

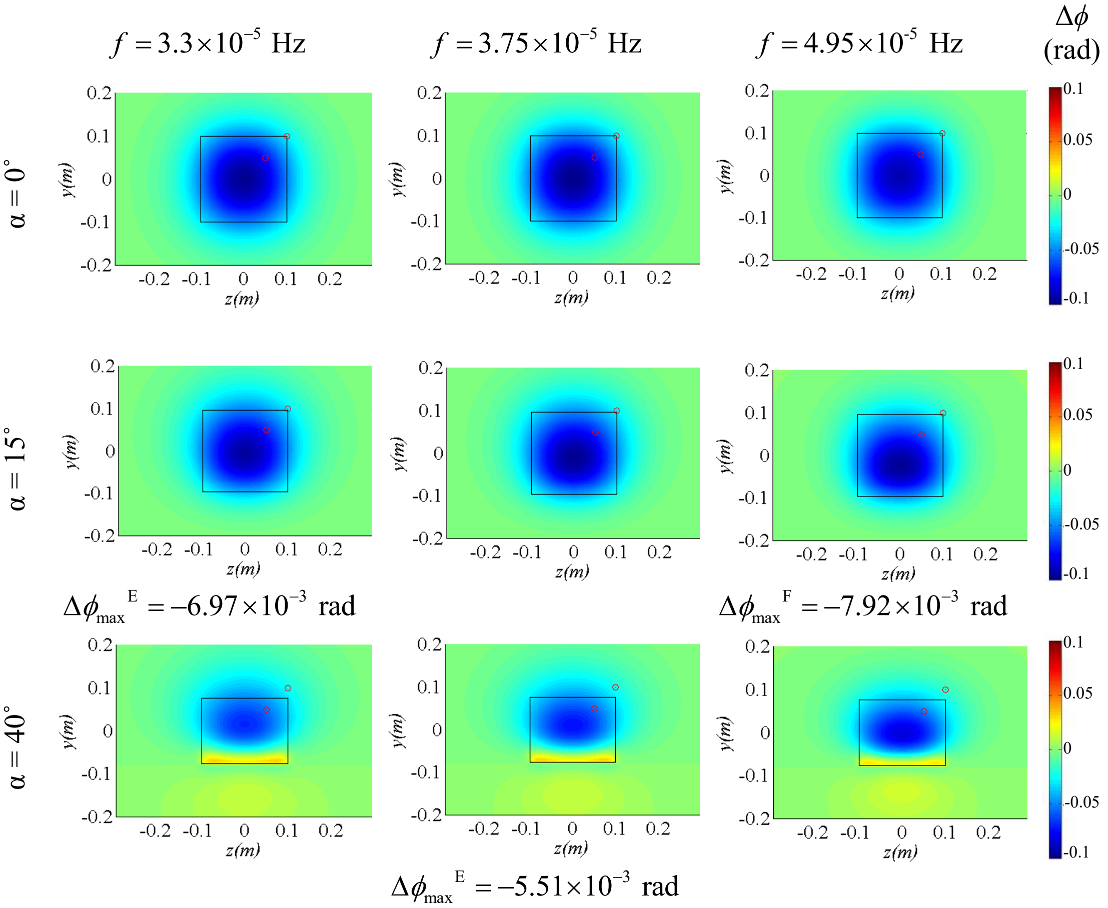

Figure 2.23: Snapshots of the phase contrast images obtained for the grid of receivers G1 for a 0.2×0.2 m^2 defect tilted 15° and 40°, subjected to a 3D point heat source.

These images indicate that, when the defect is tilted so that the lower part of the defect is closer to the surface and the upper part is further away, the results show a mixed response. Therefore, phase contrast images taken at a specific frequency can no longer provide conclusive information regarding the size and shape of the defect. A wide range of frequencies needs to be analysed in order to enable a full assessment of the defect's size and shape.

2.5.4 Influence of defect depth

In order to study the influence that changing the depth of the defect has on the heat field, the grid of receivers G1 is moved along the *x* axis closer to the defect. As shown in Figure 2.24 b) the defect depth is reduced from 0.0675 m to 0.0275 m.

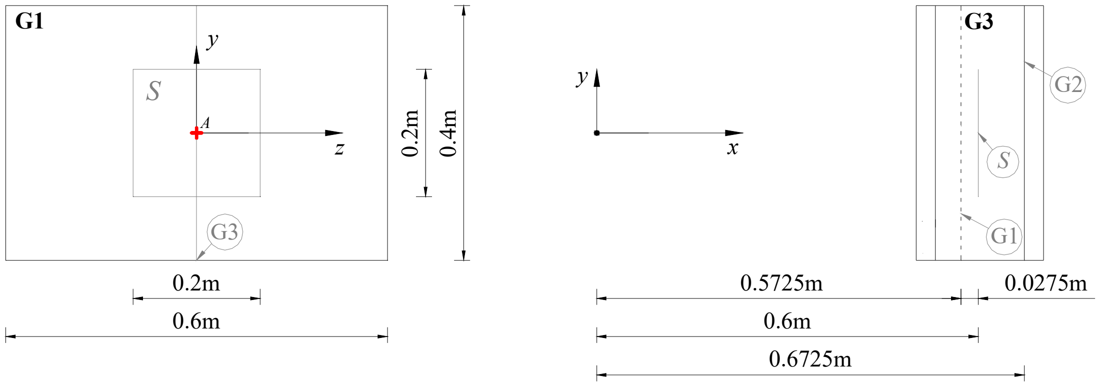

a) b)

Figure 2.24: Geometry of the system modelled: a) front view with placement of receiver A; b) vertical cross section.

The graphs in Figure 2.25 show the phase contrast results obtained for receiver A located at (0.5325, 0.0, 0.0) m and at (0.5725, 0.0, 0.0) m in the presence of a 0.2×0.2 m^2 vertical defect, which simulates a reduction in the depth of the defect from 0.0675 m to 0.0275 m. Figure 2.25 also includes the reference curves obtained for the infinite sized defect with the grid of receivers in these same two positions.

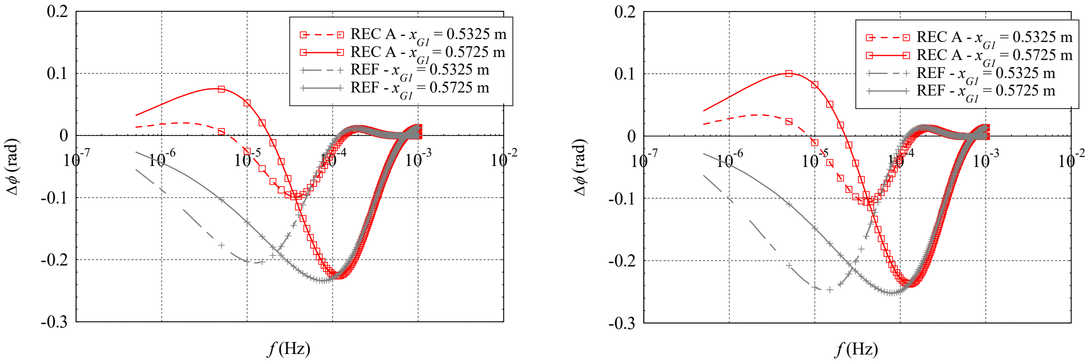

a) b)

Figure 2.25: Phase contrast curves for a 0.2×0.2 m^2 defect and reference curves for infinite size defect for receiver A at x_{G1} = 0.5325 m and placed at x_{G1} = 0.5725 m subjected to a: a) 3D point heat source; b) 1D heat source.

For both the 0.2×0.2 m^2 and the infinite sized defect, the results show that reducing the depth of the defect increased the phase contrast peak and the corresponding characteristic frequency. Furthermore, as the defect depth is reduced, it can also be said that the blind frequency increased as well. Comparison between point and planar heat source results show that, as the depth of the defect is reduced, results for a receiver located at the centre of the defect become more similar in terms of characteristic frequency f_{ch} and absolute maximum phase contrast $\left|\Delta\phi_{\max}\right|$.

In Figure 2.26, the phase contrast images obtained for G1 recorded at several frequencies are shown for the case of the 3D heat source. Results for the 1D planar heat source are similar and therefore are not shown. The selected frequencies correspond to the characteristic frequencies obtained for receiver A for both cases and to an initial arbitrary lower frequency.

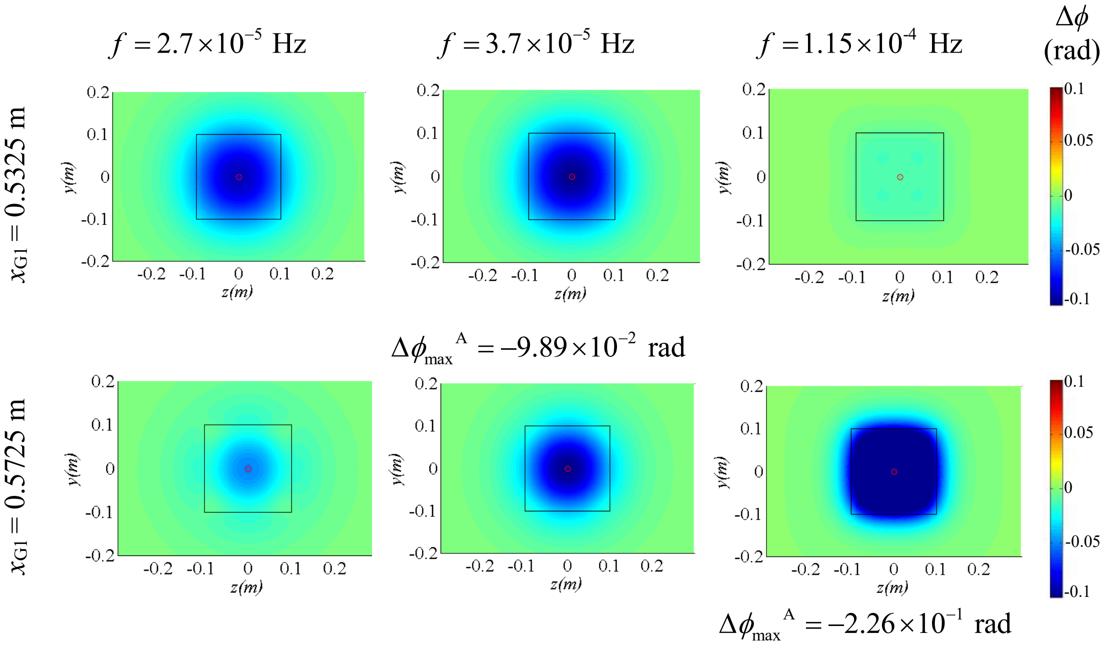

Figure 2.26: Snapshots of phase contrast images obtained for the grid of receivers G1 located at x_{G1} = 0.5325 m and x_{G1} = 0.5725 m, in the presence of a 0.2×0.2 m^2 defect, subjected to a 3D point heat source.

The phase contrast results generated demonstrate that the defect depth parameter has a great influence on the heat field generated between a surface and a defect, and therefore also on the patterns recorded at the surface. Changing a defect depth is shown to have a significant effect on the characteristic frequency which supports the use of phase contrast analysis to characterize defects and, in particular, to determine the depth at which a defect is located.

2.5.5 Influence of source position

The influence of changing the source position was demonstrated by moving the source away from the origin, and closer to the defect, to $x_s = 0.4525$ m, thus reducing the initial distance between source and defect from 0.6 m to 0.1475 m.

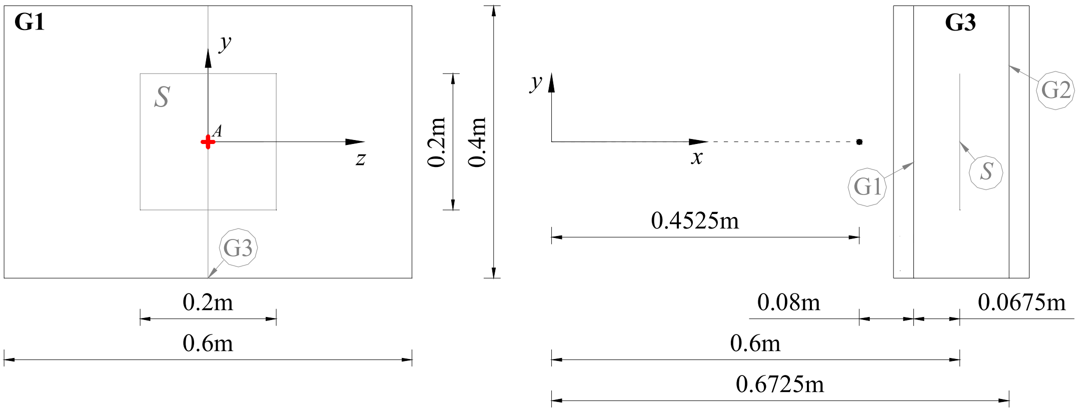

a) b)

Figure 2.27: Geometry of the system modelled: a) front view with placement of receiver A; b) vertical cross section.

To illustrate the main results, phase contrast computations for receiver A located at (0.5325, 0.0, 0.0) m in the presence of a 0.2×0.2 m^2 vertical defect are shown in Figure 2.28.

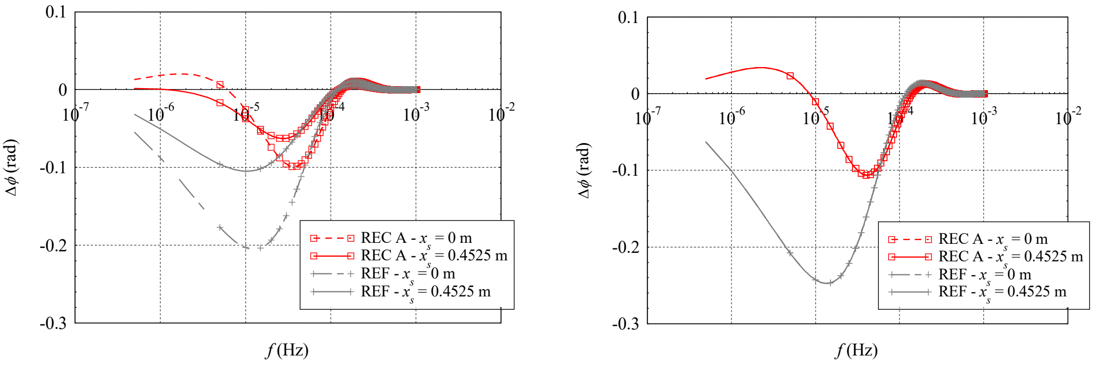

a) b)

Figure 2.28: Phase contrast results at receiver A when heat source is moved from $x_s = 0.0$ m to $x_s = 0.4525$ m, for a: a) 3D point heat source; b) 1D planar heat source.

Figure 2.28 a) indicates that, for a receiver located at the centre, when the distance to the 3D point source is shortened, the characteristic frequency f_{ch} value decreases, as well as the corresponding maximum absolute phase contrast value $|\Delta\phi_{\max}|$. The blind frequency f_b does not change significantly, therefore the detection threshold is not influenced by changing the source distance either. For a planar energy source, the values of f_{ch} and f_b are not influenced by changing the source distance, as shown in Figure 2.28 b). In this case, the heat front does not lose power as the thermal waves propagate and the difference between the incident and reflected field does not change when its source position changes.

Figure 2.29 provides snapshots of the phase contrast image results obtained for G1 for the case of changing the distance to the 3D point heat source taken at several frequencies: the characteristic frequencies for receiver A and an initial arbitrary lower frequency.

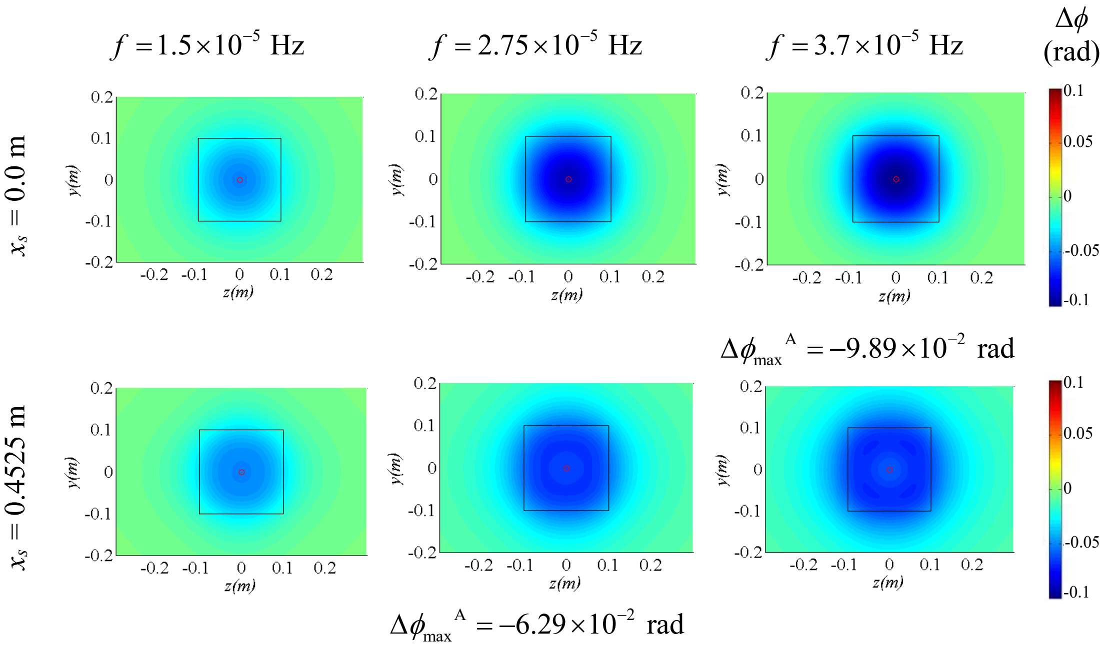

Figure 2.29: Snapshots of phase contrast images obtained for the grid of receivers G1, in the presence of a 0.2×0.2 m^2 defect, subjected to a 3D point heat source $x_s = 0.0$ m and $x_s = 0.4525$ m.

The characteristic frequency occurs at a lower frequency when the source is moved closer to the surface and the corresponding maximum phase contrast has a weaker amplitude. From these images, it is also apparent that the defect's geometry is less defined if the source is moved closer.

2.6 Final statements

A boundary elements method formulated in the frequency domain using the normal derivative integral equation (TBEM) was used to simulate 3D heat diffusion by conduction that occurs around a very thin defect embedded in an otherwise homogeneous unbounded isotropic solid medium. The proposed numerical model is intended to make a contribution to defect detection studies using active IRT as a non-destructive technique (NDT) used in building inspections by allowing for the calculation of transient heat field and thermal wave phase results in specimens containing thin defects such as cracks, voids or thin material inclusions. The model presented here is applicable to any medium that can be deemed homogeneous and where the heat conduction phenomena can be governed by the Helmholtz equation. Such media may include concrete, mortar, rock, polymers, steel, etc.

In this chapter, first the 3D TBEM formulation was presented and verified against known analytical solutions for cylindrical inclusions. Because the defect being modelled is a planar inclusion, which is assumed to have null thickness, the numerical model was written in terms of the normal derivative integral equation, since the classical BEM formulation is not able to handle very thin or null thickness defects. An analytical solution to solve the hypersingular elements that appear when using the TBEM technique was also presented for when the boundary element being integrated is also the loaded element and hypersingular integrals need to be solved.

A numerical application using the 3D TBEM model was then performed to simulate temperature and phase contrast results in the proximity of a null thickness defect logged in an unbounded space. Parameters which are relevant features in NDT using active IRT, such as the depth at which the defect is located beneath the surface, the defect's size, shape, position, and distance to heat source were analysed. Additionally, the influence of considering either a 3D point energy source or a 1D planar source in the modelling results was also studied.

Temperature difference and phase contrast responses were obtained by computing the difference between the heat field generated in a medium containing an inclusion (defective medium) and in the same medium but without defects (sound medium). The numerical results obtained in this study showed that defect characteristics have a great influence on active IRT data results. Furthermore, results clearly indicate the usefulness of the proposed formulation for understanding heat diffusion in defective media, both in the time and the frequency domains, and for interpreting experimental IRT results. Finally, although the results were found to be highly influenced by the

3D nature of the defect, it may be said that, for the cases in which the source is aligned with the centre of the defect, the results were not that much influenced by the type of heat source. In fact, the influence of changing the defect's size, depth and position did not alter significantly when the type of heat source was changed. However, planar source results were found to have the advantage of not being influenced by the distance between the defect and the heat source.

References

[1] Maldague X., Introduction to NDT by Active Infrared Thermography, Materials Evaluation, Vol. 6 (9), pp. 1060-1073, 2002.

[2] Maldague X., Theory and Practice of Infrared Technology for Non-destructive Testing, John Wiley & Sons, 2001.

[3] Ibarra-Castanedo C., González D., Klein M., Pilla M., Vallerand S., Maldague X., Infrared image processing and data analysis, Infrared Physics & Technology, Vol. 46 (1-2), pp. 75-83, 2004.

[4] Vavilov V., Modelling thermal NDT problems, International Journal of Heat and Mass Transfer, Vol. 72, pp. 75-86, 2014.

[5] Jarny Y. Introduction to heat transfer and inverse analysis. In: AVT/VKI-117 Lecture Series, Rhode-St-Genèse, April 2004.

[6] Orlande H.B., Inverse problems in heat transfer: new trends on solution methodologies and applications, Journal of Heat Transfer, Vol. 134 (3), pp.1–13, 2012.

[7] Alifanov O.M., Inverse heat transfer problems, Berlin, Springer, 1994.

[8] Jarny Y., Ozisik M.N., Bardon J.P., A general optimization method using adjoint equation for solving multidimensional inverse heat conduction, International Journal of Heat and Mass Transfer, Vol. 34 (11), pp. 2911–919, 1991.

[9] Carslaw H.S., Jaeger J.C., Conduction of Heat in Solids, Oxford University Press, Vivian Ridler, Walton Street, Oxford, 2nd edition, 1959.

[10] Bathe K.J., Numerical Methods in Finite Element Analysis, Prentice-Hall, New Jersey, 1976.

[11] Özişik M.N., Finite Difference Methods in Heat Transfer, CRC Press Inc., USA, 1994.

[12] Juncu G.h., Unsteady conjugate forced convection heat/mass transfer from a finite flat plate, International Journal of Thermal Sciences, Vol. 47, pp. 972–984, 2008.

[13] Brebbia C.A., Telles J.C., Wrobel L.C., Boundary Elements Techniques: Theory and Applications in Engineering, Springer-Verlag, Berlin-New York, 1984.

[14] Ochiai Y., Steady heat conduction analysis in orthotropic bodies by triple-reciprocity BEM, Computer Modelling in Engineering and Sciences, Vol. 2 (4), pp. 435-446, 2001.

[15] Šarler B., Towards a mesh-free computation of transport phenomena, Engineering Analysis with Boundary Elements, Vol. 26 (9), pp. 731-738, 2002.

[16] Martin P.A., Rizzo F.J. Partitioning, boundary integral equations, and exact Green's functions, International Journal for Numerical Methods in Engineering, Vol. 38 (20), pp. 3483-3495.

[17] Rudolphi T.J., The use of simple solutions in the regularisation of hypersingular boundary integral equations, Mathematical and Computer Modelling, Vol. 15, pp. 269-278, 1991.

[18] Tadeu A., Mendes P., António J., The simulation of 3D elastic scattering produced by thin rigid inclusions using the traction boundary element method, Computers and Structures Vol. 84, pp. 2244–2253. 2006

[19] Cruse T.A., Boundary Element Analysis in Computational Fracture Mechanics, Kluwer Academic Publishers, 1987.

[20] Sládek V., Sládek J., Transient elastodynamics three-dimensional problems in cracked bodies, Applied Mathematical Modelling, Vol. 8, pp. 2-10, 1984.

[21] Prosper D., Modelling and Detection of Delaminations in Laminated Plates, PhD Thesis, MIT, Cambridge, 2001.

[22] Prosper D., Kausel E., Wave scattering by cracks in laminated media, in CD: Advances in Computational Engineering and Sciences, Proceedings of the international Conference on Computational Engineering and Science ICES'01, Puerto Vallarta, Mexico,19-25/08/2001. S.N. Atluri, T. Nishioka, M. Kikuchi (eds.), Tech Science Press, 2001.

[23] Mendes P.A, Tadeu A., Wave propagation in the presence of empty cracks in an elastic medium, Computational Mechanics, Vol 38 (3), pp. 183-199, 2006.

[24] Srivastava R., Contractor D.N., Efficient evaluation of integrals in three-dimensional boundary element method using linear shape functions over plane triangular elements, Applied Mathematical Modelling, Vol. 16 (6), pp. 282-290, 1992.

[25] Niu Z., Wendland W.L., Wang X.X., Zhou H.L., A semi-analytical algorithm for the evaluation of the nearly singular integrals in three-dimensional boundary element methods, Computer Methods in Applied Mechanics and Engineering, Vol. 194, pp. 1057-1074, 2005.

[26] Tadeu A., Prata J., Simões N., Closed form integration of singular and hypersingular integrals in 3D BEM formulations for heat conduction, Mathematical Problems in Engineering, Vol. 2012, Article ID 647038, 2012.

CHAPTER 3

MODELLING OF HEAT DIFFUSION IN MEDIA WITH MULTIPLE INCLUSIONS USING AN ITERATIVE 3D TBEM APPROACH

3 MODELLING OF HEAT DIFFUSION IN MEDIA WITH MULTIPLE INCLUSIONS USING AN ITERATIVE 3D TBEM APPROACH

3.1 Introduction

As previously mentioned, the development of numerical modelling tools is paramount to advance the application of infrared thermography (IRT) since the simulation of heat diffusion in solid media allows for a better understanding of the influence that the existence of defects has on temperature distribution and heat flow within the materials being evaluated. In order to achieve a quantitative characterization of the most relevant properties of subsurface defects, namely its thermal properties and the defect's depth, it is necessary to solve transient heat transfer problems. Furthermore, numerical simulations can be used to establish defect detection potential and define the limitations of using IRT [1]. However, this need to simulate transient diffusion still presents difficulties, one of which is the high computational effort associated with many modelling techniques.

The previous chapter dealt with three-dimensional (3D) heat diffusion modelling in an unbounded spatially uniform solid medium using the boundary element method (BEM) containing a thin 3D defect. While still having the definite advantage of only requiring the discretization of the inclusion being modelled, when presented with more complex problems, such as systems with more than one inclusion, the BEM can lead to high computational effort due to the 3D nature of the defects being modelled and the complexity of the heat transfer phenomena in transient regime. Motivated by a need to reduce the processing time involved with solving 3D heat diffusion simulation problems, this chapter presents an iterative approach to simulate 3D heat diffusion using the BEM formulated in the frequency domain in an unbounded solid medium that contains multiple inclusions subjected to a 3D heat source. This approach can also be used to reduce the computer processing time for one single inclusion if divided into several subdomains.

Conventionally, numerical modelling requires either the discretization of the domain of the problem, as in finite elements methods (FEM) [2] and finite differences methods (FDM) ([3],[4]), or the discretization of the boundary, in the case of the BEM ([5],[6]). Methods based on domain discretization are, however, better suited to deal with a bounded domain, since they require its full discretization. In the case of multiple inclusions, the space between them would also need to be discretized, which would require special attention. This becomes unfeasible if there is a very large number of inclusions embedded in an unbounded domain. As stated previously, of the available numerical methods for homogeneous unbounded or layered systems modelling, the BEM is the technique that automatically satisfies far field conditions and therefore only requires the discretization of the boundaries of the inclusions. However, the BEM results in fully populated systems of equations, while FDM and FEM techniques lead to sparse systems of equations.

The major drawback of the BEM is that for it to be applied to more general geometries and media it requires previous knowledge of the relevant fundamental solutions (Green's functions). Additionally, it is known that when using the BEM, boundary integrals may become singular or nearly singular, depending on the distance between the source point and the node being integrated. Also, when the thickness of the heterogeneity being modelled tends towards zero, as in the case of delaminations, cracks or thin defects, the conventional direct BEM degenerates and becomes inaccurate, and is no longer a valid basis for numerical modelling. Among the techniques that have been proposed to overcome this are the dual boundary element method (DBEM) [7] or the normal derivative integral equation (TBEM), which lead to hypersingular integrals. The correct integration of singular and hypersingular integrals is one of the big challenges of these techniques. Various numerical methods have been proposed to overcome difficulties posed by such singularities [8-12], and the BEM is still regarded as one of the most suitable tools for modelling 3D heat diffusion generated by heat sources in an unbounded spatially uniform solid medium.

In fact, there have been various studies dedicated to reducing the computational effort associated with these simulations. Ma *et al.* [13] used a BEM formulation to study transient heat conduction in 3D solids with fibre inclusions. Jablonski [14] proposed the analytical evaluation of the BEM surface integrals by means of 3D Laplace and Poisson equations. Qin *et al.* [15] implemented changes to the conventional distance transformation technique to evaluate nearly singular integrals on 3D boundary elements, including planar and curved surface elements and very irregular elements of slender shape.

Iterative solvers or multi-domain methods have also been suggested by authors to solve or avoid systems in 3D BEM problems with very large meshes. As described by Škerget and Rek [16] and Ramšak *et al.* [17], by using a multi-domain method the system matrix becomes sparse, thus considerably decreasing the amount of memory needed. By analysing subdomains separately, where independent discretization can be considered for each subdomain and suitable solvers can be used for their individual systems of equations, smaller and better conditioned systems of equations can be obtained. One disadvantage of 3D multi-domain BEM stems from the difficulties of applying interface conditions between subdomains with a highly sparse system matrix. To overcome this, Ramšak and Škerget have extended their previous work using discretization of mixed elements ([16],[17]) to 3D problems, and proposed a 3D BEM formulation for very large meshes using a multi-domain method where each element is itself a subdomain [18]. Valente and Pina [19] explored iterative techniques based on conjugate gradient type methods as an alternative to the direct solution techniques for large scale 3D problems. They concluded that these methods are competitive for BEM algebraic systems of equations, especially if used with an appropriate preconditioner [20]. Researchers such as Marburg and Schneider [21], Ylä-Oijala and Järvenpää [22] and Alia *et al.* [23] have proposed iterative approaches for acoustics problems.

In the present chapter, an iterative approach and domain decomposition method are presented, driven by the need to reduce the computer memory requirements and computation time needed to model 3D heat diffusion in an unbounded spatially uniform solid medium containing multiple inclusions subjected to a 3D heat source using the full 3D TBEM formulation in the frequency domain [24] presented in the previous chapter. In the sections that follow, first the problem is defined, then the iterative approach to the normal derivative integral equations formulation of the frequency domain boundary elements method is proposed. Analytical solutions [25] are used to solve the hypersingular integrals that appear in this 3D TBEM formulation when the element being integrated is the loaded element. The performance of the proposed iterative method is studied by performing a set of numerical applications, determining the computer processing time and number of iterations required. Processing time results for the full 3D TBEM and the iterative approach are compared. Finally, the method employed to obtain time domain responses from the frequency domain calculations is described and transient temperature results are presented in order to illustrate the heat field results.

3.2 Problem definition

The problem being studied is the computation of heat diffusion in the presence of multiple inclusions subjected to a 3D point heat source. The inclusions are embedded in an unbounded spatially uniform solid medium of density ρ, thermal conductivity λ and specific heat c. To illustrate the numerical formulation used in the study, consider the system of two 3D inclusions embedded in the medium represented in Figure 3.1. The thin inclusions with surfaces S_1 and S_2 are subjected to a 3D point heat source located at $\boldsymbol{x}_s = (x_s, y_s, z_s)$. These are assumed to be of null thickness, and null heat fluxes are prescribed along S_1 and S_2.

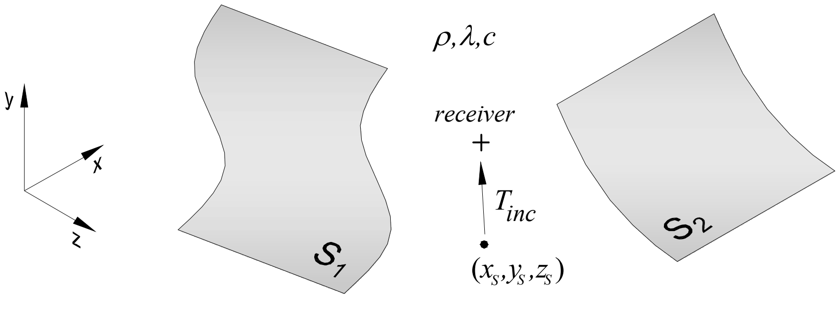

Figure 3.1: 3D view of the geometry of the problem.

3.3 Problem formulation

In an unbounded spatially uniform solid medium with thermal diffusivity K, the following equation can be used to express 3D heat diffusion in cartesian coordinates:

$$\left(\frac{\partial^2}{\partial x^2}+\frac{\partial^2}{\partial y^2}+\frac{\partial^2}{\partial z^2}\right)T\left(t,\boldsymbol{x}\right)=\frac{1}{K}\frac{\partial T}{\partial t}, \tag{3.1}$$

in which $T\left(t,\boldsymbol{x}\right)$ is transient temperature, t is time and $K=\lambda/\left(\rho c\right)$.

The former can be written as a Helmholtz equation by applying the Fourier transform to (3.1), leading to the following equation expressing frequency domain heat diffusion:

$$\left(\frac{\partial^2}{\partial x^2}+\frac{\partial^2}{\partial y^2}+\frac{\partial^2}{\partial z^2}+\left(\sqrt{-\frac{\mathrm{i}\omega}{K}}\right)^2\right)\hat{T}\left(\omega,\boldsymbol{x}\right)=0, \tag{3.2}$$

where $\hat{T}\left(\omega,\boldsymbol{x}\right)$ is temperature in the frequency domain, ω is angular frequency and $\mathrm{i}=\sqrt{-1}$.

Equation (3.2) allows heat diffusion to be studied as the propagation of harmonic waves. Hence, considering a harmonic heat source placed at $\boldsymbol{x}_s=\left(x_s,y_s,z_s\right)$ expressed as $p\left(t,\boldsymbol{x},\omega\right)=P\delta\left(x-x_s\right)\delta\left(y-y_s\right)\delta\left(z-z_s\right)e^{\mathrm{i}\omega t}$, where P is heat source amplitude and $\delta\left(x-x_s\right)$, $\delta\left(y-y_s\right)$ and $\delta\left(z-z_s\right)$ are Dirac delta functions, the generated heat field incident at $\boldsymbol{x}=\left(x,y,z\right)$ is given by :

$$\hat{T}_{inc}(\omega,\boldsymbol{x},\boldsymbol{x}_s)=\frac{Pe^{-\mathrm{i}\sqrt{-\frac{\mathrm{i}\omega}{K}}r_s}}{2\lambda r_s}, \tag{3.3}$$

in which $\hat{T}_{inc}$ is the incident heat field anywhere in the domain which is generated by the 3D heat source oscillating at a frequency of ω located at a distance of $r_s=\sqrt{\left(x-x_s\right)^2+\left(y-y_s\right)^2+\left(z-z_s\right)^2}$.

The sections that follow describe an iterative approach to a 3D TBEM formulation which can be used to simulate 3D heat diffusion generated by a 3D point heat source in the presence of more than one 3D inclusion.

3.3.1 Iterative normal derivative integral equation (iterative 3D TBEM)

The heat diffusion equation (3.2) can also be expressed as:

$$\left(\frac{\partial^2}{\partial x^2}+\frac{\partial^2}{\partial y^2}+\frac{\partial^2}{\partial z^2}\right)\hat{T}(\omega,\boldsymbol{x})+{k_c}^2\,\hat{T}(\omega,\boldsymbol{x})=0\,, \tag{3.4}$$

in which $k_c=\sqrt{-\mathrm{i}\omega/K}$.

<u>Iteration 0 - Step 1</u>

First consider that the field generated by the heat source given in (3.3) reaches the inclusion S_1 while S_2 is assumed to be absent, as represented in Figure 3.2 a).

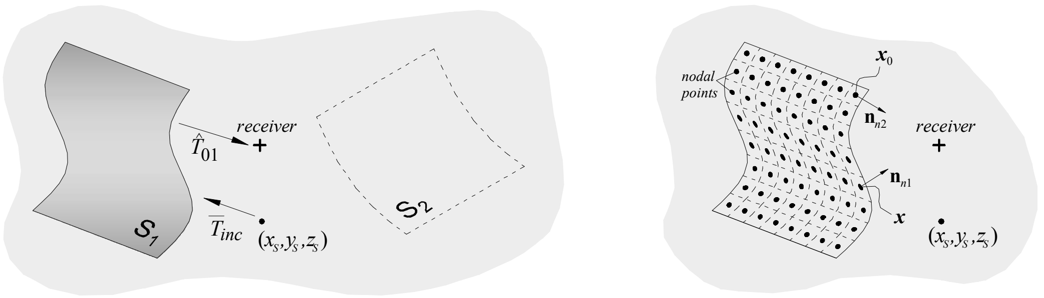

a) b)

Figure 3.2: Step 1 of iteration 0: a) geometry of the problem; b) discretization of the first inclusion into boundary elements and nodal points.

To overcome the limitations of the classical BEM formulation related to modelling null thickness inclusions, this problem is formulated using the normal derivative integral equation (TBEM), which is obtained by applying the gradient operator to the following reduced boundary integral equation:

$$b\,\hat{T}^{(0)}(\omega,\boldsymbol{x}_0)=-\int_{S_1}H(\omega,\boldsymbol{x},\boldsymbol{x}_0,\mathbf{n}_{n1})\,\hat{T}^{(0)}(\omega,\boldsymbol{x})\,\mathrm{d}s+\hat{T}_{inc}(\omega,\boldsymbol{x}_0,\boldsymbol{x}_s)\,. \tag{3.5}$$

In Equation (3.5) the superscript (0) indicates the number of the iteration; H is the required fundamental solution (Green's function for heat flux) at any point $\boldsymbol{x}$ of the boundary of the inclusion S_1 subjected to a virtual heat load at a collocation point $\boldsymbol{x}_0=(x_0,y_0,z_0)$; $\mathbf{n}_{n1}$ is the unit outward normal along the boundary S_1; $\hat{T}_{inc}$ is the heat field incident at $\boldsymbol{x}_0$ generated by the heat source located at $\boldsymbol{x}_s$; and b is a constant defined by the shape of the boundary which is ½ if $\boldsymbol{x}_0 \in S_1$ or 1 otherwise.

The Green’s function for heat flux in an unbounded medium is given by:

$$H\left(\omega,\boldsymbol{x},\boldsymbol{x}_0,\mathbf{n}_{n1}\right)=\frac{e^{-\mathrm{i}k_c r_0}\left(-\mathrm{i}\,k_c r_0-1\right)}{4\pi\lambda r_0^{2}}\frac{\partial r}{\partial \mathbf{n}_{n1}}, \tag{3.6}$$

with $r_0=\sqrt{\left(x-x_0\right)^2+\left(y-y_0\right)^2+\left(z-z_0\right)^2}$.

By applying the gradient operator to Equation (3.5) and assuming the inclusion is loaded with dipole heat sources (dynamic doublets) we obtain the normal derivative integral equation which can be expressed as:

$$a\,\hat{T}^{(0)}(\omega,\boldsymbol{x}_0)=-\int_{S_1}\overline{H}(\omega,\boldsymbol{x},\boldsymbol{x}_0,\mathbf{n}_{n1},\mathbf{n}_{n2})\,\hat{T}^{(0)}(\omega,\boldsymbol{x})\,\mathrm{ds}+\overline{T}_{inc}(\omega,\boldsymbol{x}_0,\boldsymbol{x}_s,\mathbf{n}_{n2}) . \tag{3.7}$$

Green's function $\overline{H}$ is the derivative of the former Green's function for heat flux, which is obtained from applying the gradient operator to *H*; $\mathbf{n}_{n2}$ is the unit outward normal to the boundary at the collocation points $\boldsymbol{x}_0$; and the factor *a* is null for piecewise planar boundary elements.

The 3D Green’s function for an unbounded medium results in the following:

$$\overline{H}(\omega,\boldsymbol{x},\boldsymbol{x}_0,\mathbf{n}_{n1},\mathbf{n}_{n2})=\frac{\partial H}{\partial x}\frac{\partial x}{\partial \mathbf{n}_{n2}}+\frac{\partial H}{\partial y}\frac{\partial y}{\partial \mathbf{n}_{n2}}+\frac{\partial H}{\partial z}\frac{\partial z}{\partial \mathbf{n}_{n2}}, \tag{3.8}$$

with

$$\frac{\partial H}{\partial x}(\omega,\boldsymbol{x},\boldsymbol{x}_0,\mathbf{n}_{n1})=\frac{1}{4\pi}\left\{A\left[\left(\frac{\partial r_0}{\partial x}\right)^2\frac{\partial x}{\partial \mathbf{n}_{n1}}+\frac{\partial r_0}{\partial x}\frac{\partial r_0}{\partial y}\frac{\partial y}{\partial \mathbf{n}_{n1}}+\frac{\partial r_0}{\partial x}\frac{\partial r_0}{\partial z}\frac{\partial z}{\partial \mathbf{n}_{n1}}\right]+B\left[\frac{\partial x}{\partial \mathbf{n}_{n1}}\right]\right\},$$

$$\frac{\partial H}{\partial y}(\omega,\boldsymbol{x},\boldsymbol{x}_0,\mathbf{n}_{n1})=\frac{1}{4\pi}\left\{A\left[\frac{\partial r_0}{\partial x}\frac{\partial r_0}{\partial y}\frac{\partial x}{\partial \mathbf{n}_{n1}}+\left(\frac{\partial r_0}{\partial y}\right)^2\frac{\partial y}{\partial \mathbf{n}_{n1}}+\frac{\partial r_0}{\partial y}\frac{\partial r_0}{\partial z}\frac{\partial z}{\partial \mathbf{n}_{n1}}\right]+B\left[\frac{\partial y}{\partial \mathbf{n}_{n1}}\right]\right\},$$

$$\frac{\partial H}{\partial z}(\omega,\boldsymbol{x},\boldsymbol{x}_0,\mathbf{n}_{n1})=\frac{1}{4\pi}\left\{A\left[\frac{\partial r_0}{\partial x}\frac{\partial r_0}{\partial z}\frac{\partial x}{\partial \mathbf{n}_{n1}}+\frac{\partial r_0}{\partial y}\frac{\partial r_0}{\partial z}\frac{\partial y}{\partial \mathbf{n}_{n1}}+\left(\frac{\partial r_0}{\partial z}\right)^2\frac{\partial z}{\partial \mathbf{n}_{n1}}\right]+B\left[\frac{\partial z}{\partial \mathbf{n}_{n1}}\right]\right\},$$

$$A=-\frac{k_c^{\,2}e^{-\mathrm{i}k_c r_0}}{r_0}+\frac{3\mathrm{i}k_c e^{-\mathrm{i}k_c r_0}}{r_0^{\,2}}+\frac{3e^{-\mathrm{i}k_c r_0}}{r_0^{\,3}}\ \text{and}\ B=-\frac{\mathrm{i}k_c e^{-\mathrm{i}k_c r_0}}{r_0^{\,2}}-\frac{e^{-\mathrm{i}k_c r_0}}{r_0^{\,3}}.$$

The incident heat field in Equation (3.7) is given by:

$$\overline{T}_{inc}(\omega,\boldsymbol{x},\boldsymbol{x}_s,\mathbf{n}_{n2})=\frac{Pe^{-\mathrm{i}k_c r_s}\left(-\mathrm{i}k_c r_s-1\right)}{2\lambda r_s^{\,2}}\left(\frac{\partial r_s}{\partial x}\frac{\partial x}{\partial \mathbf{n}_{n2}}+\frac{\partial r_s}{\partial y}\frac{\partial y}{\partial \mathbf{n}_{n2}}+\frac{\partial r_s}{\partial z}\frac{\partial z}{\partial \mathbf{n}_{n2}}\right). \tag{3.9}$$

The solution is found by solving Equation (3.7), which requires the discretization of inclusion S_1 into N_1 planar boundary elements with one nodal point at the centre of each element (see Figure 3.2 b)). This leads to a system of $\left[N_1\times N_1\right]$ equations ($\underline{\underline{B}}\,\underline{\hat{T}}^{(0)}=\underline{\hat{T}}_{inc}^{(0)}$) in which $\underline{\underline{B}}$ is the matrix that compiles the integration of $\int_{S_1} H(\omega,\boldsymbol{x},\boldsymbol{x}_0,\mathbf{n}_{n1})\hat{T}^{(0)}(\omega,\boldsymbol{x})\,\mathrm{d}s$ along each boundary element (for each virtual source placed along the nodal points). This system can be expressed as:

$$\left[\overline{H}^{kl}\right]\left[\hat{T}^{(0)l}\right]=\left[\overline{T}_{inc}^{(0)k}\right], \tag{3.10}$$

in which *l* is the element being integrated and *k* is the element being loaded and $k,l=1$ to N_1; $\overline{H}^{kl}=\int_{A_l}\overline{H}(\omega,\boldsymbol{x}_l,\boldsymbol{x}_k,\mathbf{n}_{n1},\mathbf{n}_{n2})\,\mathrm{d}A_l$ is the Green's function for heat flux for a nodal point being integrated $\boldsymbol{x}_l=\left(x_l,y_l,z_l\right)$ subjected to a virtual heat source placed at $\boldsymbol{x}_k=\left(x_k,y_k,z_k\right)$ and A_l is the surface of boundary element *l*; $\hat{T}^{(0)l}$ is the nodal temperature at iteration 0; and $\overline{T}_{inc}^{(0)k}$ is the incident heat field at iteration 0.

The integrations in (3.10) are performed using a Gaussian quadrature scheme when the element to be integrated is not the loaded element. When the element being integrated is the loaded element, the integrands exhibit a singularity (hypersingular element), therefore, for the loaded element, the resulting hypersingular integrands of the Green's functions are solved analytically by following the procedure described in the previous chapter in section 2.3.3 and based on the work by Tadeu *et al.* [25]. The solution to the system of equations in (3.10) gives the nodal heat

$\hat{T}^{(0)}$ along the boundary S_1, allowing the heat diffusion field to be defined for a receiver placed anywhere in the domain $\boldsymbol{x}_{rec} = \left(x_{rec}, y_{rec}, z_{rec}\right)$ as:

$$\hat{T}_{01}(\omega, \boldsymbol{x}_{rec}) = -\int_{S_1} H(\omega, \boldsymbol{x}, \boldsymbol{x}_{rec}, \mathbf{n}_{n1}) \hat{T}^{(0)}(\omega, \boldsymbol{x}) \mathrm{ds}\,. \tag{3.11}$$

In Equation (3.11), the “01” in subscript in $\hat{T}_{01}$ is relative to the number of the iteration (0) and to the inclusion which is being considered (1 for inclusion *S*S_1).

<u>*Iteration 0 - Step 2*</u>

Now consider that a second inclusion is being reached by the heat field incident from the source and by the heat field generated by the presence of the first inclusion in the previous step (see Figure 3.3 a)).

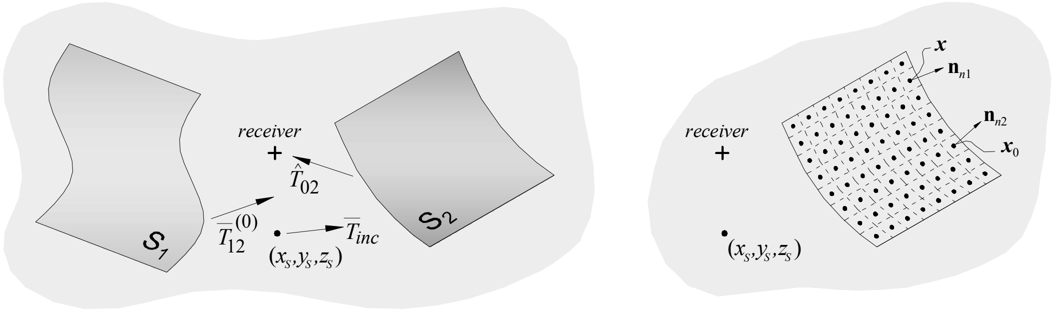

a) b)

Figure 3.3: Representation of step 2 of iteration 0: a) geometry of the problem; b) discretization of the second inclusion into boundary elements with nodal points.

The second null thickness inclusion is modelled in the same way as S_1 was in the previous step. S_2 is discretized into N_2 planar boundary elements with one nodal point at the centre of each element. Now, the heat field generated by the inclusion S_1 is taken into account. The heat field generated by the first inclusion defined in Step 1 is now viewed as a heat field that reaches the second inclusion:

$$\overline{T}_{12}^{(0)}(\omega, \boldsymbol{x}_0, \mathbf{n}_{n2}) = -\int_{S_1} \overline{H}(\omega, \boldsymbol{x}, \boldsymbol{x}_0, \mathbf{n}_{n1}, \mathbf{n}_{n2}) \hat{T}^{(0)}(\omega, \boldsymbol{x}) \mathrm{ds}\,, \tag{3.12}$$

in which the “12” in subscript gives the source of the heat field (1 for inclusion *S₁*) and the inclusion being reach (2 for inclusion *S₂*) in this step. The normal derivative integral equation can then be written as:

$$a\hat{T}^{(0)}(\omega,\boldsymbol{x}_0) = -\int_{S_2} \overline{H}(\omega,\boldsymbol{x},\boldsymbol{x}_0,\mathbf{n}_{n1},\mathbf{n}_{n2})\hat{T}^{(0)}(\omega,\boldsymbol{x})\,\mathrm{ds} + \overline{T}_{inc}(\omega,\boldsymbol{x}_0,\boldsymbol{x}_s,\mathbf{n}_{n2}) + \overline{T}_{12}^{(0)}(\omega,\boldsymbol{x}_0,\mathbf{n}_{n2})\,. \quad (3.13)$$

Once again the factor *a* is null for piecewise planar boundary elements.

This leads to a system of $[N_2 \times N_2]$ equations ($\underline{\underline{C}}\,\underline{\hat{T}}^{(0)} = \underline{\hat{T}}_{inc}^{(0)}$) which allows the unknown nodal amplitudes to be defined. The system is expressed as:

$$\left[\overline{H}^{kl}\right]\left[\hat{T}^{(0)l}\right] = \left[\overline{T}_{inc}^{(0)k}\right], \quad (3.14)$$

where $k,l = 1$ to N_2 and $\overline{T}_{inc}^{(0)}(\omega,\boldsymbol{x}_0,\mathbf{n}_{n2}) = \overline{T}_{inc}(\omega,\boldsymbol{x}_0,\boldsymbol{x}_s,\mathbf{n}_{n2}) + \overline{T}_{12}^{(0)}(\omega,\boldsymbol{x}_0,\mathbf{n}_{n2})$. The disturbance in the heat field at $\boldsymbol{x}_{rec}$ can then be expressed as:

$$\hat{T}_{02}(\omega,\boldsymbol{x}_{rec}) = -\int_{S_2} H(\omega,\boldsymbol{x},\boldsymbol{x}_{rec},\mathbf{n}_{n1})\hat{T}^{(0)}(\omega,\boldsymbol{x})\,\mathrm{ds}\,. \quad (3.15)$$

Again, in this equation, the “02” in subscript in $\hat{T}_{02}$ is relative to the number of the iteration (0) and to the inclusion which is now being modelled (2 for inclusion *S₂*).

At the end of this iteration, the total heat field recorded at a given receiver located at $\boldsymbol{x}_{rec}$ is given by the following:

$$\hat{T}(\omega,\boldsymbol{x}_{rec}) = \hat{T}_{inc}(\omega,\boldsymbol{x}_{rec},\boldsymbol{x}_s) + \sum_{m=1}^{M}\hat{T}_{0m}(\omega,\boldsymbol{x}_{rec})\,, \quad (3.16)$$

where M is the total number of inclusions, which is two in this case.

Iteration k - Step 1

Finally, consider the first step of an iteration *k* where the first inclusion S_1 is reached only by the field generated by the second inclusion S_2 which is obtained for the conditions defined by step 2 of the previous iteration (*k*−1) (see Figure 3.4).

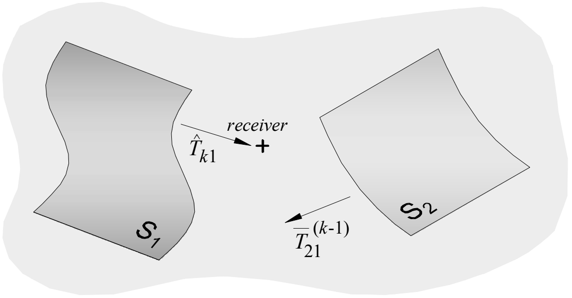

Figure 3.4: Step 1 of iteration *k*.

At this stage the incident heat field corresponds to the field generated by the second inclusion in the previous iteration, and is given by:

$$\overline{T}_{21}^{(k-1)}(\omega,\boldsymbol{x}_0,\mathbf{n}_{n2}) = -\int_{S_2} \overline{H}(\omega,\boldsymbol{x},\boldsymbol{x}_0,\mathbf{n}_{n1},\mathbf{n}_{n2})\,\hat{T}^{(k-1)}(\omega,\boldsymbol{x})\,\mathrm{ds}\,, \tag{3.17}$$

Again, in this equation the term “21” in subscript is relative to the source of the heat field (S_2) and the inclusion being reached (S_1) in this step, which leads to:

$$a\,\hat{T}^{(k)}(\omega,\boldsymbol{x}_0) = -\int_{S_1} \overline{H}(\omega,\boldsymbol{x},\boldsymbol{x}_0,\mathbf{n}_{n1},\mathbf{n}_{n2})\,\hat{T}^{(k)}(\omega,\boldsymbol{x})\,\mathrm{ds} + \overline{T}_{21}^{(k-1)}(\omega,\boldsymbol{x}_0,\mathbf{n}_{n2})\,. \tag{3.18}$$

The solution of this equation leads to a system of $\left[N_1 \times N_1\right]$ equations ($\underline{\underline{B}}\,\underline{\hat{T}}^{(k)} = \underline{\overline{T}}_{inc}^{(k)}$), similar to the one calculated previously, where only the constant matrix needs to be modified. In this equation (k) refers to the number of the iteration. If in iteration 0 the system has been solved by defining its inverse matrix $\underline{\underline{B}}^{-1}$, the new solution will not require the system to be solved, as $\underline{\hat{T}}^{(k)} = \underline{\underline{B}}^{-1}\underline{\overline{T}}_{inc}^{(k)}$. The heat field disturbance at the receiver $\boldsymbol{x}_{rec}$ is now to be computed as:

$$\hat{T}_{k1}(\omega,\boldsymbol{x}_{rec}) = -\int_{S_1} H(\omega,\boldsymbol{x},\boldsymbol{x}_{rec},\mathbf{n}_{n1})\,\hat{T}^{(k)}(\omega,\boldsymbol{x})\,\mathrm{ds}\,. \tag{3.19}$$

Iteration k - Step 2

In the second step of iteration k, the second inclusion is reached only by the heat field generated by the first inclusion subjected to the incident heat field defined in the previous step (see Figure 3.5).

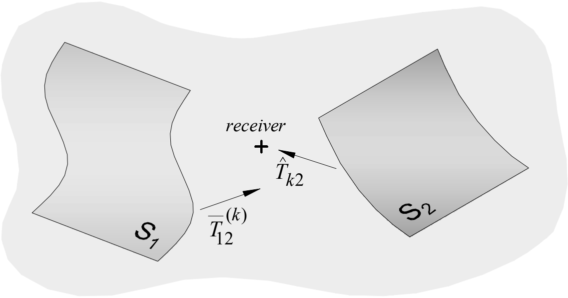

Figure 3.5: Step 2 of iteration *k*.

The heat field generated by the first inclusion in the previous step is assumed to be the only heat field which reaches the second inclusion, and is given by:

$$\overline{T}_{12}^{(k)}(\omega,\boldsymbol{x}_0,\mathbf{n}_{n2}) = -\int_{S_1} \overline{H}(\omega,\boldsymbol{x},\boldsymbol{x}_0,\mathbf{n}_{n1},\mathbf{n}_{n2})\,\hat{T}^{(k)}(\omega,\boldsymbol{x})\,\mathrm{ds}\,, \tag{3.20}$$

which leads to:

$$a\,\hat{T}^{(k)}(\omega,\boldsymbol{x}_0) = -\int_{S_2} \overline{H}(\omega,\boldsymbol{x},\boldsymbol{x}_0,\mathbf{n}_{n1},\mathbf{n}_{n2})\,\hat{T}^{(k)}(\omega,\boldsymbol{x})\,\mathrm{ds} + \overline{T}_{12}^{(k)}(\omega,\boldsymbol{x}_0,\mathbf{n}_{n2})\,. \tag{3.21}$$

This leads to a system of $\left[N_2 \times N_2\right]$ equations ($\underline{\underline{C}}\,\underline{\hat{T}}^{(k)} = \underline{\hat{T}}_{inc}^{(k)}$), similar to the one defined for (3.18) where the constant matrix needs to be replaced by $\hat{T}_{inc}^{(k)}(\omega,\boldsymbol{x}_0,\mathbf{n}_{n2}) = \overline{T}_{12}^{(k)}(\omega,\boldsymbol{x}_0,\mathbf{n}_{n2})$. $\hat{T}^{(k)}$ can be obtained since $\underline{\hat{T}}^{(k)} = \underline{\underline{C}}^{-1}\underline{\hat{T}}_{inc}^{(k)}$. The new heat field produced by this inclusion recorded at $\boldsymbol{x}_{rec}$ is expressed by:

$$\hat{T}_{k2}(\omega,\boldsymbol{x}_{rec}) = -\int_{S_2} H(\omega,\boldsymbol{x},\boldsymbol{x}_{rec},\mathbf{n}_{n1})\,\hat{T}^{(k)}(\omega,\boldsymbol{x})\,\mathrm{ds}\,. \tag{3.22}$$

At the end of iteration *k* the total heat field recorded at the receiver is given by:

$$\hat{T}(\omega,\boldsymbol{x}_{rec}) = \hat{T}_{inc}(\omega,\boldsymbol{x}_{rec},\boldsymbol{x}_s) + \sum_{k=0}^{k}\sum_{m=1}^{M}\hat{T}_{km}(\omega,\boldsymbol{x}_{rec})\,. \tag{3.23}$$

The iterative process will continue until the contribution of the last new field to the total heat field at a specific receiver reaches a predefined threshold.

The proposed iterative process requires only the individual linear system of equations related to each inclusion to be solved. Given the example used to illustrate the algorithm procedure, for two inclusions, this requires solving two individual systems of $\left[N_1 \times N_1\right]$ and $\left[N_2 \times N_2\right]$ equations only once. The full modelling process would require solving a system of $\left[(N_1 + N_2) \times (N_1 + N_2)\right]$ equations. The proposed iterative approach is more relevant as the number of inclusions increases. The size of the system of equations used by the full model becomes greater when compared with the system associated with each inclusion (as used in the proposed iterative model), which raises the interest in using this approach.

3.3.2 Temperature in time

The heat field in the time domain is determined by applying a numerical inverse fast Fourier transform to the frequency domain response. Aliasing phenomena are dealt with by introducing complex frequencies with a small imaginary part $\omega_c = \omega - \mathrm{i}\eta$, with $\eta = 0.7\Delta\omega$ and a frequency step of $\Delta\omega$. In the time domain this is taken into account by introducing an exponential window, by applying $e^{\eta t}$ to the response.

The heat source can have any time variation, and the frequency domain solution can be determined by applying a time Fourier transformation for frequencies ranging from 0.0 Hz to high frequencies. However, there is no need to compute the highest frequencies because the contribution to the response in the higher frequencies is very weak. The null frequency corresponds to the static response.

3.4 Results

Numerical results for a specific case study application are presented next. First the case study system is described. Then, in order to make an assessment of the performance of the iterative approach, the obtained frequency domain results are compared with the ones given by the full 3D TBEM formulation. Additionally, time domain responses are presented in order to illustrate the transient heat field found in a medium with multiple inclusions. Transient temperature results are also presented in order to illustrate the simulation of heat diffusion in the time domain in the defective medium containing multiple inclusions.

3.4.1 Case study

The proposed model is used to simulate heat diffusion around four 3D null thickness inclusions, which correspond to the four parallel planes represented in Figure 3.6. Computations are performed for two grids of receivers (G1 and G2) which, as shown, are perpendicular to the inclusions being modelled and to each other.

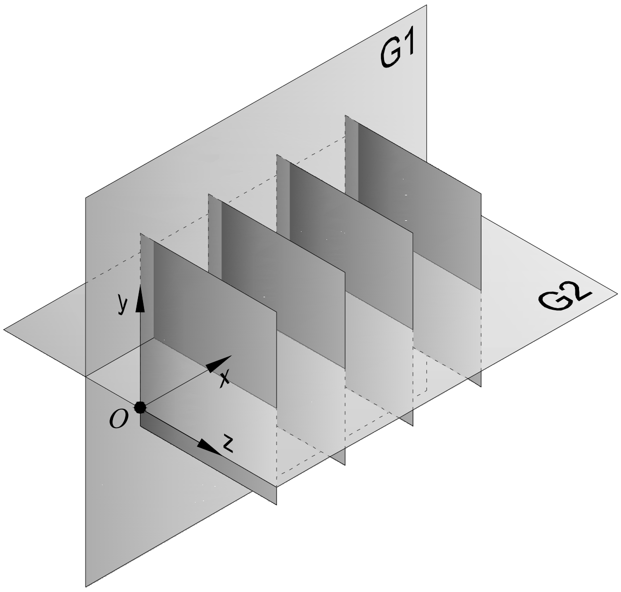

Figure 3.6: 3D view of the system modelled.

The uniform unbounded solid medium that contains the four inclusions has density $\rho = 2300.0$ kg/m^3, thermal conductivity $\lambda = 1.4$ W/(m.ºC) and specific heat $c = 880.0$ J/(kg.ºC), and is subjected to a 3D heat source located at the origin of the axes at $\boldsymbol{x}_s = (0.0, 0.0, 0.0)$ m. The two grids of receivers are 0.5×0.4 m^2 and each contain a total of 4141 receivers. As seen in Figure 3.6, grid G1 is placed parallel to the xy plane at $z = -0.08$ m and its receivers are spaced at equal intervals of $\Delta x = 0.005$ m and $\Delta y = 0.01$ m. G2 is placed parallel to the xz plane at $y = 0.0$ m with receivers located at intervals of $\Delta x = 0.005$ m and $\Delta z = 0.01$ m.

As shown in Figure 3.7, the four thin inclusions are 0.2×0.2 m^2 and parallel to the yz plane, placed away from the source along the x axis and 0.1 m apart from each other. Each plane is discretized into 800 elements: 40 in the z axis direction by 20 in the y direction.

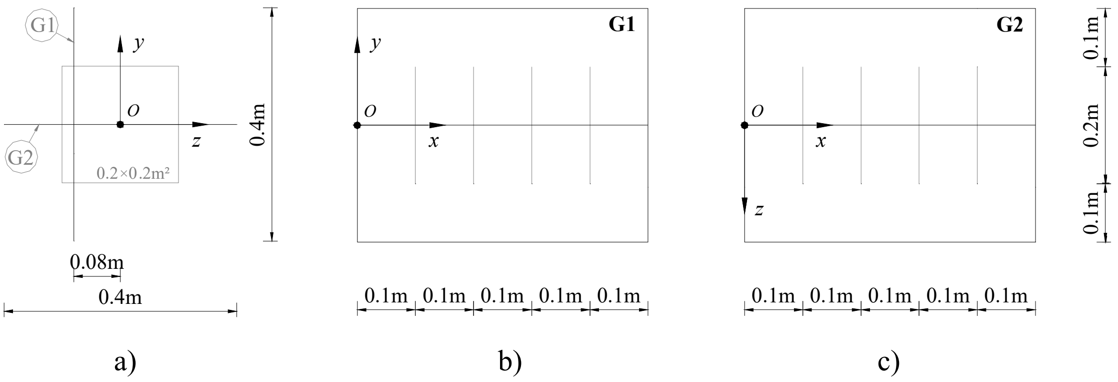

Figure 3.7: Geometry of the system modelled: a) *yz* plane; b) *xy* plane; c) *xz* plane.

3.4.2 Iterative 3D TBEM performance

In this section, the performance of the proposed iterative 3D TBEM is assessed by making a comparison between results obtained for modelling heat diffusion in the presence of four 3D inclusions using the full 3D normal derivative equation formulation presented previously (3D TBEM) with those obtained by using the iterative approach. Furthermore, two variations of the iterative approach were considered. In one, a domain decomposition method in which two sub-domains containing each a pair of inclusions are defined, is used. In the other the iterative approach is used considering each inclusion separately.

All computations where performed using a 2.30 GHz Intel® Core™ i5-2410M CPU with 4.00 GB RAM. The time taken to compute the generated heat field (CPU time) is compared using the following three distinct approaches:

I) *Simulation of 3D heat diffusion in a medium containing multiple inclusions using the full 3D TBEM;*

II) *Definition of two sub-domains containing two inclusions (pairing of inclusions) followed by the computation of 3D heat diffusion in each subdomain containing a pair of inclusions using the iterative 3D TBEM;*

III) *Simulation of 3D heat diffusion in a medium containing multiple inclusions using the iterative 3D TBEM approach (considering each inclusion separately).*

The number of iterations needed to solve the problem using the proposed iterative model is also recorded. The iteration loop is stopped and the number of iterations N_I is registered when the temperature at each individual receiver does not change by more than a predefined threshold (τ) when compared to the former iteration, according to the following equation:

$$\frac{\left|\sum_{k=0}^{N_I}\sum_{m=1}^{M}\hat{T}_{km}(\boldsymbol{x}_{rec},\omega)-\sum_{k=0}^{N_I-1}\sum_{m=1}^{M}\hat{T}_{km}(\boldsymbol{x}_{rec},\omega)\right|}{\left|\sum_{k=0}^{N_I}\sum_{m=1}^{M}\hat{T}_{iter\,m}(\boldsymbol{x}_{rec},\omega)\right|}\leq\tau\,. \tag{3.24}$$

Three excitation frequencies were selected to illustrate the main findings: $f = 0.0$ Hz; $f = 0.5\times10^{-6}$ Hz and $f = 6.4\times10^{-5}$ Hz. Figure 3.8 shows the real part of the frequency domain temperature results recorded at the receivers in grid G1 using the full 3D TBEM and Figure 3.9 provides the imaginary part of this response, also recorded at G1. Due to the geometry of the system and the placement of the heat source, results encountered at the receivers located in G2 are similar and therefore are not shown here.

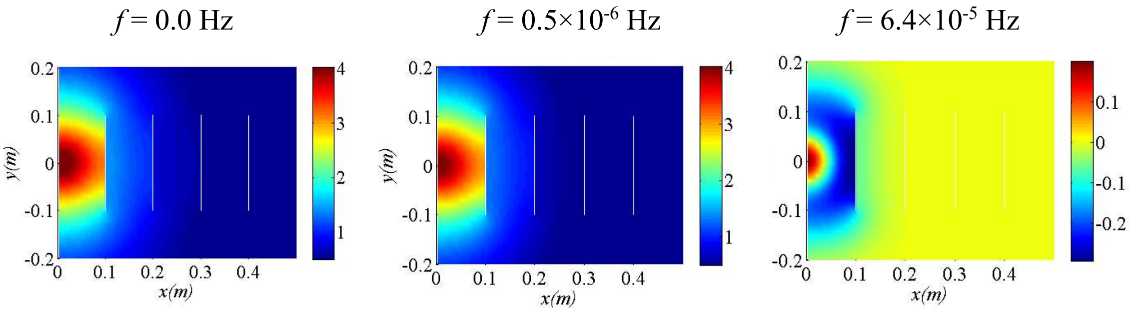
$f = 0.0$ Hz

$f = 0.5\times10^{-6}$ Hz

$f = 6.4\times10^{-5}$ Hz

Figure 3.8: Snapshots of the real part of the temperature response, in ° C, computed using the full 3D TBEM, taken at several frequencies.

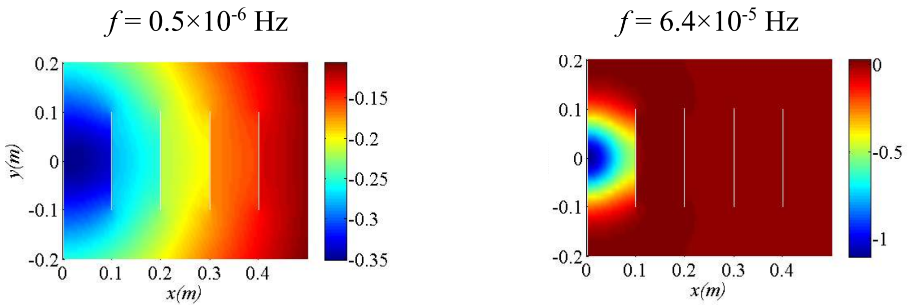
$f = 0.5\times10^{-6}$ Hz

$f = 6.4\times10^{-5}$ Hz

Figure 3.9: Snapshots of the imaginary part of the temperature response, in °C, computed using the full 3D TBEM, taken at several frequencies.

The response computed for null frequency corresponds to the static response and does not have an imaginary part, therefore no response for null frequency is given in Figure 3.9.

<u>*Computer processing time*</u>

When using the full 3D TBEM formulation, the average time required to compute the solution for the null frequency was 308 min. For $f = 0.5\times10^{-6}$ Hz calculations took an average of 321.9 min, and for $f = 6.4\times10^{-5}$ Hz the average CPU time was 322.0 min. In Figure 3.10, the average CPU time needed for the iterative 3D TBEM approach with domain decomposition (pairing of two inclusions) to yield results is given along with snapshots illustrating the variations on all the receivers in G1. In a similar fashion, Figure 3.11 presents the CPU time for the iterative 3D TBEM approach when the inclusions are considered separately.

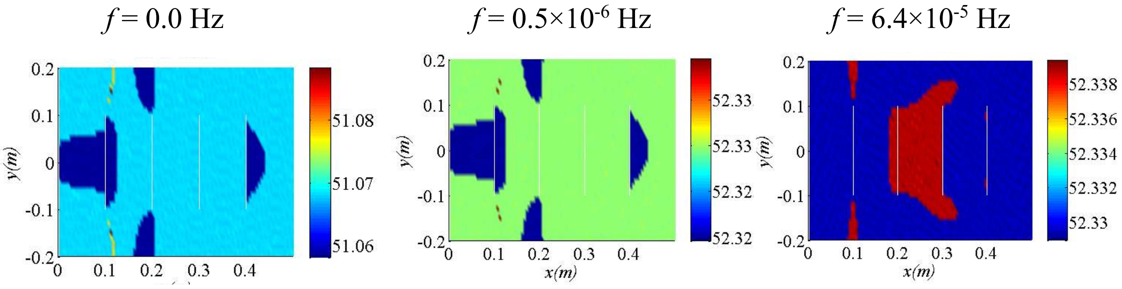

average CPU time = 51.1 min average CPU time = 52.3 min average CPU time = 52.3 min

Figure 3.10: Snapshots of CPU time, in minutes, using an iterative 3D TBEM approach with pairing of inclusions, taken at several frequencies.

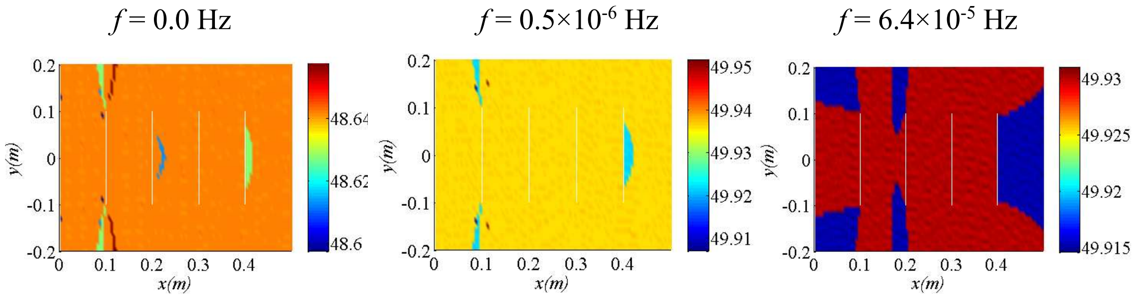

average CPU time = 48.6 min average CPU time = 49.9 min average CPU time = 49.9 min

Figure 3.11: Snapshots of CPU time, in minutes, using an iterative 3D TBEM approach considering separate inclusions, taken at several frequencies.

These results clearly indicate that, for any frequency, using an iterative method greatly reduces CPU time when compared to the full 3D TBEM method. The performance of the iterative method is slightly better when each inclusion is considered individually (approach III) as CPU time is further reduced.

Number of iterations

Figure 3.12 provides a representation of the number of iterations required for the iterative 3D TBEM approach with domain decomposition along all the receivers in G1, and Figure 3.13 gives the number of iterations required for the iterative 3D TBEM approach considering each inclusion separately.

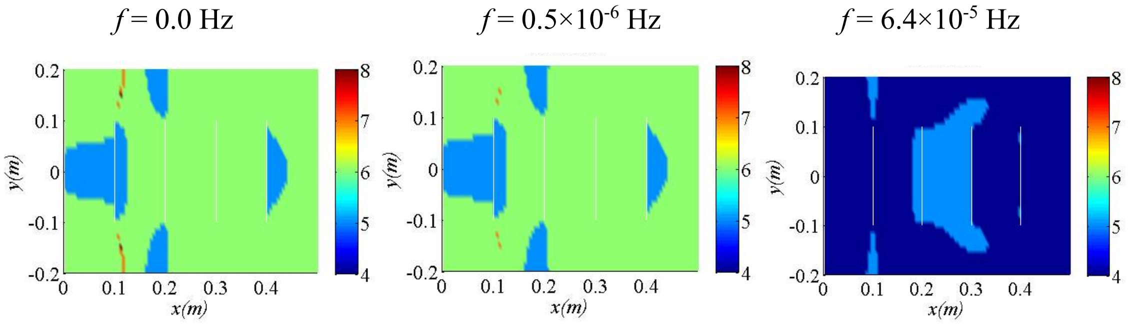
$f = 0.0$ Hz

$f = 0.5\times10^{-6}$ Hz

$f = 6.4\times10^{-5}$ Hz

Figure 3.12: Snapshots of the number of iterations required using iterative 3D TBEM with domain decomposition, taken at several frequencies.

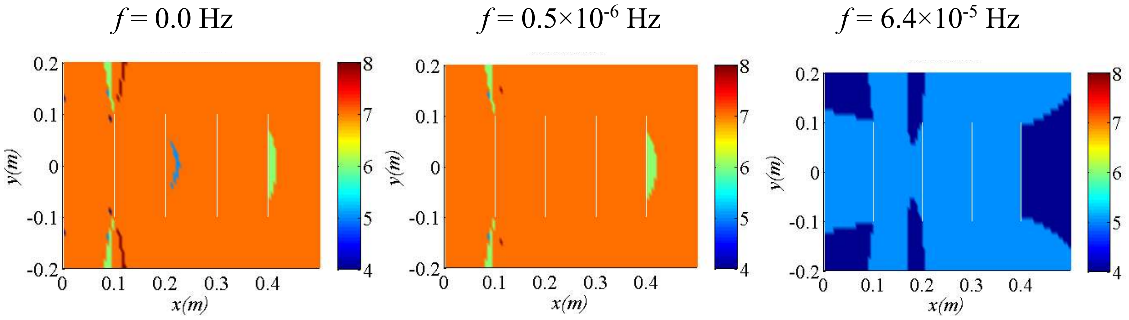
$f = 0.0$ Hz

$f = 0.5\times10^{-6}$ Hz

$f = 6.4\times10^{-5}$ Hz

Figure 3.13: Snapshots of the number of iterations required for using iterative 3D TBEM considering separate inclusions, taken at several frequencies.

The results show that the number of iterations varies for each receiver (as does the CPU time). Fewer iterations are required in zones which are less affected by disturbances in the heat field, which, for approach III (iterative 3D TBEM considering each inclusion separately) corresponds to the areas behind the inclusions placed at $x = 0.2$ m and $x = 0.4$ m. In the case of the inclusion pairing approach (II), it is the zone before the first inclusion and after the last inclusion. In both iterative approaches, the number of iterations diminishes as the frequency increases, however CPU time increases slightly.

3.4.3 Heat field in time domain

Transient temperature computations are performed in the frequency range of 0.0 Hz to 1.024×10^{-3} Hz with a frequency increment of $\Delta f = 0.5\times10^{-6}$ Hz, which results in a time window of 555.56 h. The imaginary part of the frequency is given by $\eta = 0.7\Delta\omega$ and $\Delta\omega = 2\pi\Delta f$. The host medium is assumed to be initially at 20.0 ºC. The source starts emitting energy at instant $t = 0.5$ h and continues for 9.5 h. The heat source time dependence is assumed to be rectangular with an amplitude of $P = 6.27$. This amplitude is defined so that a maximum temperature increase of 15.0 ºC is registered by a receiver located in grid G2 at $(x, y, z) =$ (0.1, 0.0, 0.0) m within a sound medium, meaning a medium without any defects (inclusions).

In order to illustrate heat propagation in the defective medium, snapshot images taken at different instants are shown in Figure 3.14. In order to make a comparison, Figure 3.15 shows the results obtained in a sound medium which does not contain any inclusions.

Figure 3.14 clearly illustrates the effect that the first inclusion has on temperature diffusion. By instant $t = 9.9$ h the heat source has stopped emitting energy and the temperature at $(x, y, z) =$ (0.1, 0.0, 0.0) m, immediately in front of the centre of the first inclusion, reaches its peak. The snapshot on the right shows the instant when the temperature is maximum in the zone immediately before the second inclusion.

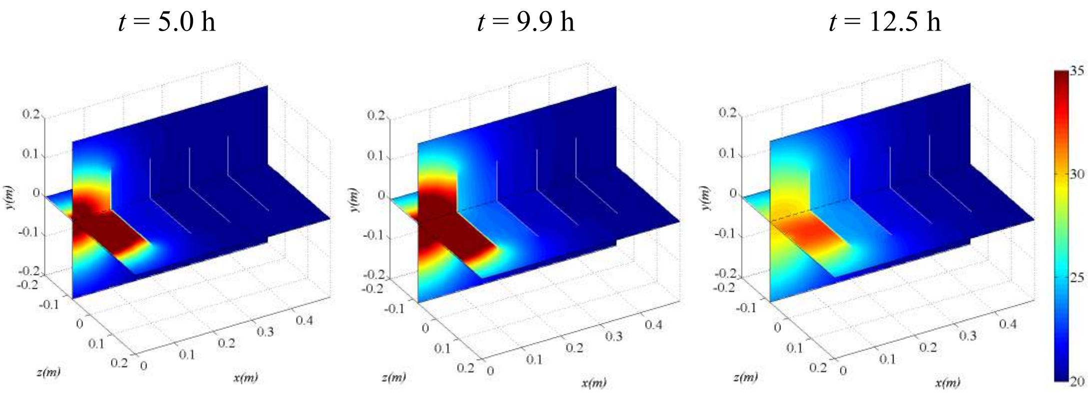

Figure 3.14. Snapshots of transient heat field, in °C, in a defective medium containing four plane inclusions, taken at several instants.

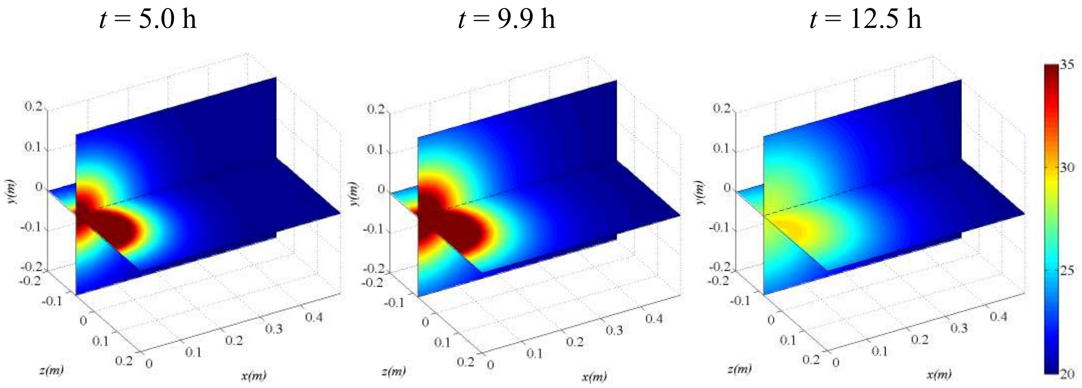

Figure 3.15. Snapshots of transient heat field, in °C, in a sound medium containing four plane inclusions, taken at several instants.

3.5 Final statements

This chapter presents an iterative model to simulate 3D heat diffusion in an unbounded spatially uniform solid medium with multiple inclusions subjected to a 3D point heat source. The resulting heat field in the presence of multiple inclusions was computed using a normal derivative integral equation (TBEM) formulation. An iterative approach to the 3D TBEM formulation was described, as well as the method to obtain time domain responses from frequency domain calculations.

The performance of the proposed iterative 3D TBEM was assessed by comparing the results generated using the full 3D normal derivative equation formulation (3D TBEM) with those obtained using the iterative model. Two different iterative approaches were considered: solving each inclusion separately or considering sub-domains by pairing inclusions and solving two at each turn. By solving each inclusion separately, only one inclusion is computed at a time, at each step of the iterative approach. Employing this method required solving a lower number of small systems of equations rather than one large system, and led to a significant decrease in CPU time (for both iterative approaches). For a given frequency, the CPU time and the number of iterations required for each receiver varied in both iterative approaches. The number of iterations required fell as the analysed frequency increased, though the average CPU time increased slightly. Considering each inclusion separately generated only slightly better results than when sub-domains of pairs of inclusions were considered. It is concluded that using the proposed iterative model greatly reduces the computational effort needed to simulate 3D heat diffusion generated by a point heat source in an unbounded uniform medium with multiple inclusions.

In order to further demonstrate the applicability of the method, a numerical application to time domain temperature calculations was also presented.

References

[1] Maldague X., Introduction to NDT by Active Infrared Thermography, Materials Evaluation, Vol. 6 (9), pp. 1060-1073, 2002.

[2] Bathe K.J., Numerical Methods in Finite Element Analysis, Prentice-Hall, New Jersey, 1976.

[3] Özişik M.N., Finite Difference Methods in Heat Transfer, CRC Press Inc, USA, 1994.

[4] Juncu Gh., Unsteady conjugate forced convection heat/mass transfer from a finite flat plate, International Journal of Thermal Sciences, Vol. 47 (12), pp. 972–984, 2008.

[5] Brebbia C.A., Telles J.C., Wrobel L.C., Boundary Elements Techniques: Theory and Applications in Engineering, Springer-Verlag, Berlin-New York, 1984.

[6] Ochiai Y., Steady heat conduction analysis in orthotropic bodies by triple-reciprocity BEM, Computer Modelling in Engineering and Sciences, Vol. 2 (4), pp. 435-446, 2001.

[7] Rudolphi T.J., The use of simple solutions in the regularisation of hypersingular boundary integral equations, Mathematical and Computer Modelling, Vol. 15, pp. 269-278, 1991.

[8] Zhou H., Niu Z., Cheng C., Guan Z., Analytical integral algorithm applied to boundary layer effect and thin body effect in BEM for anisotropic potential problems, Computers & Structures, Vol. 86, pp. 1656-1671, 2008.

[9] Telles J.C.F., A self-adaptive co-ordinates transformation for efficient numerical evaluation of general boundary element integrals, International Journal for Numerical Methods in Engineering, Vol. 24, pp. 959-973, 1987.

[10] Chen X.L., Liu Y.J., An advanced 3-D Boundary Element Method for characterizations of composite materials, Engineering Analysis with Boundary Elements, Vol. 29, pp. 513-523, 2005.

[11] Hayami K., Variable transformations for nearly singular integrals in the boundary element method, Publications of the Research Institute for Mathematical Sciences, Vol. 41, pp. 821-842, 2005.

[12] Ma H., Kamiya N., Distance transformation for the numerical evaluation of near singular boundary integrals with various kernels in boundary element method, Engineering Analysis with Boundary Elements, Vol. 26, pp. 329-339, 2002.

[13] Ma F., Chatterjee J., Henry D.P., Banerjee P.K., Transient heat conduction analysis of 3D solids with fibre inclusions using the boundary element method, International Journal for Numerical Methods in Engineering, Vol. 73 (8), pp. 1113-1136, 2008.

[14] Jablonski P., Integral and geometrical means in the analytical evaluation of the BEM integrals for a 3D Laplace equation, Engineering Analysis with Boundary Elements, Vol. 34 (3), pp. 264-273, 2010.

[15] Qin X., Zhang J., Xie G., Zhou F., Li G., A general algorithm for the numerical evaluation of nearly singular integrals on 3D boundary element, Journal of Computational and Applied Mathematics, Vol. 235 (14), pp. 4174-4186, 2011.

[16] Škerget L., Rek Z., Boundary-domain integral method using a velocity-vorticity formulation, Engineering Analysis with Boundary Elements, Vol. 15 (4), pp. 359–370, 1995.

[17] Ramšak M., Škerget L., Hriberšk M., Zunič Z., A multidomain Boundary Element Method for unsteady laminar flow using stream function - vorticity equations, Engineering Analysis with Boundary Elements, Vol. 29, pp. 1–14, 2005.

[18] Ramšak M., Škerget L., 3D multidomain BEM for solving the Laplace equation, Engineering Analysis with Boundary Elements, Vol. 31 (6), pp. 528-538, 2007.

[19] Valente F.P., Pina H.L., Iterative techniques for 3-D boundary element method systems of equations, Engineering Analysis with Boundary Elements, Vol. 25 (6), pp. 423–429, 2001.

[20] Van der Vorst H.A., Dekker K., Conjugate gradient type methods and preconditioning, Journal of Computational and Applied Mathematics, Vol. 24 (1-2), pp. 73-87, 1988.

[21] Marburg S., Schneider S., Performance of iterative solvers for acoustic problems. Part I. Solvers and effect of diagonal preconditioning, Engineering Analysis with Boundary Elements, Vol. 27 (7), pp. 727–750, 2003.

[22] Ylä-Oijala P., Järvenpää S., Iterative solution of high-order Boundary Element Method for acoustic impedance boundary value problems, Journal of Sound and Vibration, Vol. 291 (3-5), pp. 824-843, 2006.

[23] Alia A., Sadok H., Souli M., CMRH method as iterative solver for boundary element acoustic systems, Engineering Analysis with Boundary Elements, Vol. 36 (3), pp. 346-350, 2012.

[24] Serra C., Tadeu A., Prata J., Simões N., Application of 3D heat diffusion to detect embedded 3D empty cracks, Applied Thermal Engineering, Vol. 61 (2) pp. 596-605, 2013.

[25] Tadeu A., Prata J., Simões N., Closed form integration of singular and hypersingular integrals in 3D BEM formulations for heat conduction, Mathematical Problems in Engineering, Vol 2012, Article ID 647038.

CHAPTER 4

MODELLING OF HEAT DIFFUSION IN MULTILAYERED MEDIA FOR IRT APPLICATIONS

4 MODELLING OF HEAT DIFFUSION IN MULTILAYERED MEDIA FOR IRT APPLICATIONS

4.1 Introduction

Active infrared thermography (IRT) refers to the technique that consists in using an artificial heat source to enhance the temperature difference between defective and sound areas of thermal images, making possible the detection of defects which would not otherwise be visible by IRT cameras [1]. Additionally, if the stimulus and the subsequent heat transfer phenomena that occur within the material are known, it is possible to obtain further information regarding the defect's characteristics (quantitative IRT analysis). For some time now, active infrared IRT techniques have been successfully used for defect evaluation and quality control in industrial non-destructive testing (NDT), mostly in the fields of aeronautics, electronics and mechanics [2]. However, in the buildings sector most IRT applications have been focused on performing a qualitative assessment of the building envelope and generally use a passive approach with the building elements in their natural thermal state and with no additional thermal stimulation [3]. However, as in the other areas in which this technique has thrived, there is also great potential to characterize defects by using active thermography in building applications. As stated by Grinzato *et al*. [4], through the combination of IRT test results with in-depth knowledge of heat transfer phenomena, the characterization of hidden defects in building elements can also be achieved.

Active thermography techniques are based on the following working principle: a thermal front reaches the surface of a specimen and proceeds to propagate through the material until a defect, which acts as a barrier, is encountered. This disturbance ultimately changes the thermal response recorded at the surface by the IRT camera. The available active IRT techniques are commonly categorized based on the type of thermal stimulation and the data processing methods required to extract information from the thermal images recorded over time [1]. One of the most popular techniques is known as pulse thermography (PT) [5], in which a test specimen is heated briefly (flash or pulse heating) using lamps, light beams or a laser, and the consequent temperature decrease is recorded. Usually the response is then analysed using simple thermal contrast, which is the difference between the temperature response decrease observed in a defective area of the thermal image and a sound area where there aren’t any defects.

Another widely used technique is lock-in thermography (LT) ([6],[7]), in which a specimen is subjected to a modulated stimulus using lamps, thermal emitters, microwave, ultrasound or eddy current, and thermal wave phase results are obtained by applying a Fourier transform to the time domain temperature response. Both these methods present advantages and disadvantages. Phase images generally offer benefits over thermal images since they are less affected by external factors such as reflections, surface emissivity changes and non-uniform surface heating [8], which are some of the weaknesses of PT. Another drawback of PT is that it requires a high-power heat source to generate the flash heating. On the other hand, the sinusoidal waves in LT emit at a given modulation frequency ω until a steady state is achieved, and are able to penetrate deeper without demanding such high-power energy, as well as without unnecessarily increasing the temperature of the specimen. Nonetheless, LT requires prior knowledge of the modulation frequency which depends on the properties of the specimen. LT has the capacity to reach deeper defects [9], however in each test only defects within a certain depth range are reached (fixed depth resolution) which may require several tests to be performed. In order to combine the advantages of both LT and PT, pulsed phase thermography (PPT), in which a specimen is pulse heated but thermal wave phase results are extracted, was introduced by Maldague and Marinetti [10] and later reviewed by Ibarra-Castanedo and Maldague [11]. However, this type of technique relies heavily on processing methods that involve complex algorithms [12].

Over the years, both LT and PT techniques have been successfully used to inspect defects in thin specimens made of highly conductive materials. However, because most construction materials generally exhibit lower conductivity and require a greater depth of inspection than metals, the use of active IRT in buildings has been limited [13]. Nonetheless, various approaches have been made, attempting to use active thermography to evaluate concrete [14-18] and masonry structures [19], as well as to characterize the thermal behaviour of building elements ([20],[21]) and the presence of moisture ([22],[23]).

More recently, Arndt [24] proposed that a variation of PPT, where a long pulse is used to stimulate an object's surface and frequency domain phase results are extracted, known as square pulse thermography (SPT) in the frequency domain, could be used in buildings applications to allow the long response of building materials and to enable the probing of deeper defects. In SPT, long recording periods (in the time domain) are able to generate phase results in the frequency domain with clear amplitude. However, this requires sufficient recording time and frequency resolution. Even though theoretical conditions may diverge from experimental ones due to uneven surface emissivity, non-uniform heating of the test specimen and heterogeneities in the material, numerical simulations are essential to define setup parameters and estimate the limit of depth at which defects are detectable, while avoiding the carrying out of a large number of experiments. This consideration attests to the interest in solving heat transfer problems for IRT applications in buildings.

The solution to transient heat transfer by conduction is only known analytically for simple geometries in isotropic solid media [25]. In the presence of complex geometries, numerical modelling tools based on the discretization of either the domain [26], the boundaries [27] or finite differences [28] are required.

Heat diffusion studies considering building elements as multilayered systems are becoming increasingly relevant in thermal building envelope analysis. Heat transfer in multilayered systems has been widely researched such as in the works of Özisik [29] and Haji-Sheikh and Beck [30] which are based on Green's functions. Green's functions provide fundamental solutions to the differential heat diffusion equation and allow for the calculation of temperature and heat flux generated by a heat source without the need to discretize the domain or the boundaries. More recently Tadeu *et al.* ([31],[32]) proposed analytical solutions incorporating Green's functions for 3D heat diffusion in unbounded, half-space, slab or multilayered media formulated in the frequency domain that allows the use of any amplitude time evolution of the heat source. An experimental validation of these analytical solutions can be found by Simões *et al*. [33].

In this chapter these analytical models are manipulated in order to enable comparisons with experimental IRT results. A system of infinite parallel layers is modified so as to impose a prescribed temperature along one of the boundary interfaces in order to simulate surface heating of a specimen in IRT tests. This model can be used to simulate IRT applications by considering one of its layers to be a logged defect with infinite dimensions, and the surrounding layers to be the host material. By calculating the heat field when the layer (corresponding to the defect) is present and when the layer is not present, it is possible to study the influence of a defect being present. It is worth noting that this model can be used in other applications beyond IRT to evaluate the influence that any given layer may have in the transient heat diffusion in a system following a multilayered configuration, which is the case in many building elements and construction products.

In this study, to benefit from the advantages shown by phase images in IRT studies, a phase contrast approach to defect detection is used. The model is formulated in the frequency domain, therefore phase results can be computed directly and phase contrast is obtained by modelling both the thermal wave phase for the case when the layer under study is present, and for when it is absent (and it is given the same thermal properties of the neighbouring layers), and by computing the difference between these two responses. Then, phase contrast curves are extracted for specific points in the thermal contrast image, which in IRT tests corresponds to a certain pixel within the camera field of view (FOV), *i.e.* the image captured by an infrared camera.

In order to assess the influence that certain crucial parameters have on the phase contrast results obtained in IRT studies, this chapter contains analytical and experimental applications in which several defect characteristics and test conditions are varied. Another factor that highly influences the quality of thermal images and which needs to be taken into account is presence of noise. Even though noise can be reduced, it cannot be avoided in IRT experiments. The main causes for noise are the random arrival of photons onto the infrared detector, the temperature sensitivity of the IRT camera, the presence of background reflections and material emissivity variations [34].

Over the next few sections, first, the basis for the proposed analytical model is established in Section 4.2, where analytical solutions for multilayered media using Green's functions are presented. Then, in Section 4.3, the model is used to simulate simple applications in order to study the influence of the number of layers in the system, the material properties, and thickness of the layers. Section 4.4 presents an experimental IRT campaign performed on a test specimen that resembles a building element containing a defect. These experiments are performed using an active IRT technique with a long pulse (based on SPT). Both the experimental setup and the case study test specimen are thoroughly described in this section. Also in this section is an application of the analytical model to simulate the experimental results. The influence of the presence of noise on the recorded data is also analysed. The experimental and analytical results are compared The main conclusions are drawn with focus on the effects of varying parameters related to the defect layer (depth, thickness and thermal properties) and to the experimental test (frequency resolution or recording time).

4.2 Analytical model

This section presents the Green's functions required to analytically model 3D heat diffusion in multilayered media. In order to reduce the complexity of the 3D problem, it is assumed that the interfaces in the multilayered system are parallel and the geometry is constant along one direction (z), and the solution is posed as a sum of 2D problems with linear sources that vary sinusoidally along that direction according to a wavenumber k_z. This formulation is then manipulated to consider a specific temperature t_{0b} prescribed at a boundary interface, so as to simulate uniform planar heating achieved at the specimen's surface in IRT tests, which further reduces the problem to a 1D model.

4.2.1 Heat diffusion in unbounded solid media

First consider an unbounded spatially uniform solid medium of density ρ, thermal conductivity λ and specific heat c. In cartesian coordinates, 3D transient heat diffusion is described by the following equation:

$$\left(\frac{\partial^2}{\partial x^2}+\frac{\partial^2}{\partial y^2}+\frac{\partial^2}{\partial z^2}\right)T(t,x,y,z)=\frac{1}{K}\frac{\partial T}{\partial t}, \tag{4.1}$$

in which $T(t,x,y,z)$ is transient temperature, t is time and the thermal diffusivity of the medium is given by $K = \lambda/(\rho c)$.

By applying a Fourier transform to the previous equation, transient heat transfer by conduction can be seen as the propagation of harmonic waves and expressed by the following Helmholtz equation:

$$\left(\frac{\partial^2}{\partial x^2}+\frac{\partial^2}{\partial y^2}+\frac{\partial^2}{\partial z^2}+{k_c}^2\right)\hat{T}(\omega,x,y,z)=0\,, \qquad (4.2)$$

where $\hat{T}(\omega,x,y,z)$ is temperature in the frequency domain, ω is angular frequency of the harmonic waves, $\mathrm{i}=\sqrt{-1}$ and $k_c=\sqrt{-\mathrm{i}\omega/K}$.

Considering a heat source given by $p(t,x,y,x,\omega)=P\,\delta(x-x_s)\delta(y-y_s)\delta(z-z_s)e^{\mathrm{i}\omega t}$, where P is its amplitude, $\delta(x-x_s)$, $\delta(y-y_s)$ and $\delta(z-z_s)$ are Dirac delta functions, and (x_s,y_s,z_s) is the location of the source, the resulting heat field incident anywhere in the unbounded domain is expressed as:

$$\hat{T}_{inc}(\omega,x,y,z,x_s,y_s,z_s)=\frac{Pe^{-\mathrm{i}\sqrt{-\frac{\mathrm{i}\omega}{K}}r_s}}{2\lambda r_s}\,, \qquad (4.3)$$

in which $r_s=\sqrt{(x-x_s)^2+(y-y_s)^2+(z-z_s)^2}$ is the distance from the source to a point (x,y,z) placed anywhere in the domain.

Often, since the computation of the 3D solution demands high computational effort, in systems where the geometry is constant along one of the directions, it is preferable to express the 3D heat diffusion problem as a sum of 2D problems with different spatial wavenumbers along that direction. This type of problem is referred to as 2.5D since heat transfer occurs in 3D but the system follows a 2D geometry.

Consider a system which is constant along the z axis direction. By applying a spatial Fourier transform along the z direction to Equation (4.2), heat diffusion is expressed as:

$$\left(\frac{\partial^2}{\partial x^2}+\frac{\partial^2}{\partial y^2}+\left(\sqrt{-\frac{\mathrm{i}\omega}{K}-k_z^{\,2}}\right)^2\right)\tilde{T}(\omega,x,y,k_z)=0\,, \tag{4.4}$$

where k_z is the spatial wavenumber in the direction of the *z* axis.

The solution to the former 3D problem can be obtained by adding the solutions of 2D problems subjected to a spatially varying linear harmonic heat source. For each problem, a linear source with origin in (x_s, y_s) given by $\hat{p}(t,\omega,x,y,k_z)=\delta(x-x_s)\delta(y-y_s)\delta e^{\mathrm{i}\omega t-k_z z}$ varies sinusoidally along the *z* axis with different wavenumber k_z (assuming unitary amplitude). The fundamental solution becomes:

$$\tilde{T}(\omega,x,y,k_z)=\frac{-\mathrm{i}}{4\lambda}\mathrm{H}_0\left(\sqrt{\frac{-\mathrm{i}\omega}{K}-k_z^{\,2}}\,\bar{r}_s\right), \tag{4.5}$$

in which $\mathrm{H}_\alpha(\ )$ are Hankel functions of the second kind and order α and $\bar{r}_s=\sqrt{(x-x_s)^2+(y-y_s)^2}$. The solution to the initial 3D problem is obtained by applying an inverse Fourier transform in the *z* direction. Considering the existence of virtual sources equally spaced along the *z* axis at a distance of L_z , this inverse transformation is expressed as the following discrete sum:

$$\hat{T}(\omega,x,y,z)=\frac{2\pi}{L_z}\sum_{m=-M}^{M}\tilde{T}(\omega,x,y,k_{zm})e^{-\mathrm{i}k_{zm}z}\,, \tag{4.6}$$

in which the axial wavenumber is $k_{zm}=(2\pi/L_z)m$ and L_z must be big enough so that the heat sources do not influence each other. The solution is obtained by solving a limited number ($2\times M+1$) of 2D problems. Notice that if $k_{zm}=0$ this problem corresponds to the 2D problem.

The 3D problem can also be posed as the heat diffusion generated by the continuous superposition of planar heat sources, in which case Equation (4.5) takes instead the following form:

$$\tilde{T}(\omega,x,y,k_z)=\frac{-\mathrm{i}}{4\pi\lambda}\int_{-\infty}^{\infty}\frac{e^{-\mathrm{i}\nu|y-y_s|}}{\nu}e^{-\mathrm{i}k_x(x-x_s)}\mathrm{d}k_x \tag{4.7}$$

where k_x is the spatial wavenumber in the direction of the x axis and $v=\sqrt{\frac{-\mathrm{i}\omega}{K}-k_z^{\,2}-k_x^{\,2}}$ with $\operatorname{Im}(v)\le 0$.

Considering the existence of an infinite number of virtual heat sources equally spaced along the x axis by a distance of L_x , the integration in (4.7) can be performed along the x axis, resulting in the expression:

$$\tilde{T}(\omega,x,y,k_z)=E_0\sum_{n=-\infty}^{n=+\infty}\left(\frac{E}{v_n}\right)E_d\ , \tag{4.8}$$

where $E_0=-\mathrm{i}/(2\lambda L_x)$, $E=e^{-\mathrm{i}v_n|y-y_s|}$, $E_d=e^{-\mathrm{i}k_{xn}(x-x_s)}$, $v_n=\sqrt{-\mathrm{i}\omega/K-k_z^{\,2}-k_{xn}^{\,2}}$ with $\operatorname{Im}(v)\le 0$ and $k_{xn}=(2\pi/L_x)n$. This equation can in turn be approximated by a finite sum of N equations. In this case, if k_z= 0 and k_{xn}= 0, this corresponds to a 1D problem.

4.2.2 Heat diffusion in multilayered systems

In multilayered media, in addition to the heat field incident from the heat source, the disturbances that appear at each interface that separates layers with different thermal properties must also be taken into account. At each interface, surface terms are generated to ensure the continuity of heat flux and temperature along the layers.

To illustrate this type of problem, consider the system given in Figure 4.1, which consists of m planar layers parallel to each other, bounded by two semi-infinite media (medium M_0 at the top and M_{m+1} at the bottom) and subjected to a 3D heat source placed anywhere in the domain. Each layer j may present a different thickness h_j and different thermal properties (thermal diffusivity K_j , thermal conductivity λ_j , density ρ_j and specific heat capacity c_j). Inside each layer, the thermal properties are considered constant and do not vary with temperature.

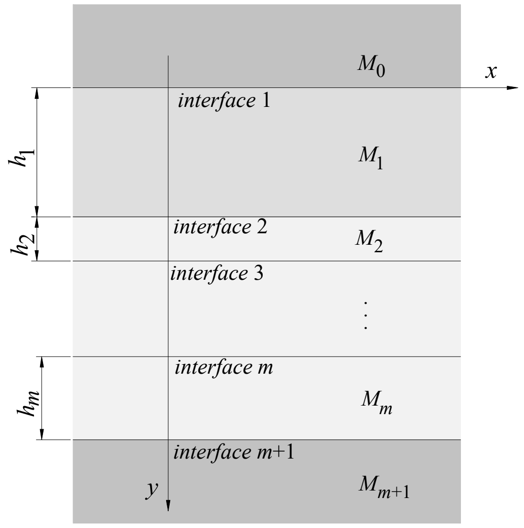

Figure 4.1: Geometry of a multilayered system bounded by semi-infinite media.

The surface terms that are generated at each interface in order to ensure the boundary conditions of continuity of heat flux and temperature between layers take a form similar to Equation (4.8) and are given by the following pair of expressions.

At the top of layer j*:*

$$\tilde{T}_{j1}\left(\omega,x,y,k_z\right)=E_{0j}\sum_{n=-\infty}^{n=+\infty}\left(\frac{E_{j1}}{\nu_{nj}}A_{nj}^{t}\right)E_d\ . \tag{4.9}$$

At the bottom of layer j*:*

$$\tilde{T}_{j2}\left(\omega,x,y,k_z\right)=E_{0j}\sum_{n=-\infty}^{n=+\infty}\left(\frac{E_{j2}}{\nu_{nj}}A_{nj}^{b}\right)E_d\ . \tag{4.10}$$

In these expressions $j=1,...,m$, $E_{0j}=-\mathrm{i}/\left(2\lambda_j L_x\right)$, $E_{j1}=e^{-\mathrm{i}\nu_{nj}\left|y-\sum_{l=1}^{j-1}h_l\right|}$ and $E_{j2}=e^{-\mathrm{i}\nu_{nj}\left|y-\sum_{l=1}^{j}h_l\right|}$, where h_l is the thickness of layer l and $\nu_{nj}=\sqrt{-\mathrm{i}\omega/K_j-k_z^{\,2}-k_{xn}^{\,2}}$, with $\mathrm{Im}\left(\nu_{nj}\right)\leq 0$ and $k_{xn}=\left(2\pi/L_x\right)n$. A_{nj}^{t} and A_{nj}^{b} are unknown coefficients that depend on the boundary conditions imposed at the top and bottom interfaces of each layer j.

Additionally, between the semi-infinite medium M_0 and layer M_1, and between layer M_m and M_{m+1} two other surface terms appear, which are given by the following expression.

At the bottom of medium M_0 (interface 1):

$$\tilde{T}_{02}\left(\omega,x,y,k_z\right)=E_{00}\sum_{n=-\infty}^{n=+\infty}\left(\frac{E_{02}}{v_{n0}}A_{n0}^{b}\right)E_d\ . \tag{4.11}$$

At the top of medium M_{m+1} (interface m+1):

$$\tilde{T}_{(m+1)1}\left(\omega,x,y,k_z\right)=E_{0(m+1)}\sum_{n=-\infty}^{n=+\infty}\left(\frac{E_{(m+1)1}}{v_{n(m+1)}}A_{n(m+1)}^{t}\right)E_d\ . \tag{4.12}$$

In which $E_{00}=-\mathrm{i}/\left(2\lambda_0 L_x\right)$, $E_{02}=e^{-\mathrm{i}v_{n0}y}$, $E_{0(m+1)}=-\mathrm{i}/\left(2\lambda_{(m+1)}L_x\right)$, $E_{(m+1)1}=e^{-\mathrm{i}v_{n(m+1)}\left|y-\sum_{l=1}^{j=m}h_l\right|}$, $v_{n0}=\sqrt{-\mathrm{i}\omega/K_0-k_z^{\ 2}-k_{xn}^{\ 2}}$ and $v_{n(m+1)}=\sqrt{-\mathrm{i}\omega/K_{(m+1)}-k_z^{\ 2}-k_{xn}^{\ 2}}$, with $\mathrm{Im}\left(v\right)\leq 0$ and $k_{xn}=\left(2\pi/L_x\right)n$, and A_{n0}^{b} and $A_{n(m+1)}^{t}$ are unknown potential amplitudes.

By assuming the continuity of heat flux and temperature along *m*+1 interfaces between *m* layers, the following system of 2×(*m*+1) equations and 2×(*m*+1) unknown variables is constructed:

$$\begin{bmatrix}
-1 & -1 & e^{-\mathrm{i}v_{n1}h_1} & \dots & 0 & 0 & 0 \\
\dfrac{1}{\lambda_0 v_{n0}} & -\dfrac{1}{\lambda_1 v_{n1}} & -\dfrac{e^{-\mathrm{i}v_{n1}h_1}}{\lambda_1 v_{n1}} & \dots & 0 & 0 & 0 \\
0 & e^{-\mathrm{i}v_{n1}h_1} & -1 & \dots & 0 & 0 & 0 \\
0 & \dfrac{e^{-\mathrm{i}v_{n1}h_1}}{\lambda_1 v_{n1}} & \dfrac{1}{\lambda_1 v_{n1}} & \dots & 0 & 0 & 0 \\
\dots & \dots & \dots & \dots & \dots & \dots & \dots \\
0 & 0 & 0 & \dots & -1 & e^{-\mathrm{i}v_{nm}h_m} & 0 \\
0 & 0 & 0 & \dots & -\dfrac{1}{\lambda_m v_{nm}} & -\dfrac{e^{-\mathrm{i}v_{nm}h_m}}{\lambda_m v_{nm}} & 0 \\
0 & 0 & 0 & \dots & e^{-\mathrm{i}v_{nm}h_{m1}} & -1 & -1 \\
0 & 0 & 0 & \dots & \dfrac{e^{-\mathrm{i}v_{nm}h_m}}{\lambda_m v_{nm}} & \dfrac{1}{\lambda_m v_{nm}} & \dfrac{1}{\lambda_{m+1}v_{n(m+1)}}
\end{bmatrix}
\begin{bmatrix}
A_{n0}^{b} \\ A_{n1}^{t} \\ A_{n1}^{b} \\ \dots \\ A_{nm}^{t} \\ A_{nm}^{b} \\ A_{n(m+1)}^{t}
\end{bmatrix}
=
\begin{bmatrix}
-e^{-\mathrm{i}v_{n1}y_s} \\ \dfrac{e^{-\mathrm{i}v_{n1}y_s}}{\lambda_1 v_{n1}} \\ -e^{-\mathrm{i}v_{n1}\left|h_1-y_s\right|} \\ -\dfrac{e^{-\mathrm{i}v_{n1}\left|h_1-y_s\right|}}{\lambda_1 v_{n1}} \\ \dots \\ 0 \\ 0 \\ 0 \\ 0
\end{bmatrix} \tag{4.13}$$

Solving the system of equations gives the amplitude of the surface terms (A_{nm}^{t} and A_{nm}^{b}).

Since the total heat field is expressed by the sum of the source term and surface terms, if a heat source located somewhere in layer 1 ($0 < y_s < h_1$) is considered, the heat field anywhere in the domain is given by the following expressions.

In the upper semi-infinite medium M_0 *(*$y < 0$*):*

$$\tilde{T}\left(\omega, x, y, k_z\right) = E_{00} \sum_{n=-\infty}^{n=+\infty} \left(\frac{E_{02}}{\nu_{n0}} A_{n0}^{b} \right) E_d \,. \tag{4.14}$$

In medium M_1 *(*$0 < y < h_1$*):*

$$\tilde{T}\left(\omega, x, y, k_z\right) = \frac{-\mathrm{i}}{4\lambda_1} \mathrm{H}_0 \left(\sqrt{\frac{-\mathrm{i}\omega}{K} - k_z{}^2}\, \overline{r_s} \right) + E_{01} \sum_{n=-\infty}^{n=+\infty} \left(\frac{E_{11}}{\nu_{n1}} A_{n1}^{t} + \frac{E_{12}}{\nu_{n1}} A_{n1}^{b} \right) E_d \,. \tag{4.15}$$

In any layer j≠1 ($\sum_{l=1}^{j=1} h_l < y < \sum_{l=1}^{j} h_l$*):*

$$\tilde{T}\left(\omega, x, y, k_z\right) = E_{0j} \sum_{n=-\infty}^{n=+\infty} \left(\frac{E_{j1}}{\nu_{nj}} A_{nj}^{t} + \frac{E_{j2}}{\nu_{nj}} A_{nj}^{b} \right) E_d \,. \tag{4.16}$$

In the lower semi-infinite medium M_{m+1} *(*$y > \sum_{l=1}^{j=m} h_l$*):*

$$\tilde{T}\left(\omega, x, y, k_z\right) = E_{0(m+1)} \sum_{n=-\infty}^{n=+\infty} \left(\frac{E_{(m+1)1}}{\nu_{n(m+1)}} A_{n(m+1)}^{t} \right) E_d \,. \tag{4.17}$$

The former equations (4.14) to (4.17) can be easily modified so as to accommodate the position of the source in any other layer, which is not shown.

4.2.3 Heat diffusion in a multilayered system bounded by an interface with prescribed temperature

In order to simulate the surface heating that occurs in active IRT experiments, a specific temperature t_{0b} is prescribed at interface *m* at the bottom (see in Figure 4.2). Since the geometry of the system is constant along the directions of the *x* and *z*, and the imposed temperature at the bottom is constant along the plane interface, heat diffusion in the system occurs unidimensionally. Therefore, this problem can be posed similarly to the 3D heat diffusion in multilayered media problem where $k_z = 0$ and $k_{xn} = 0$.

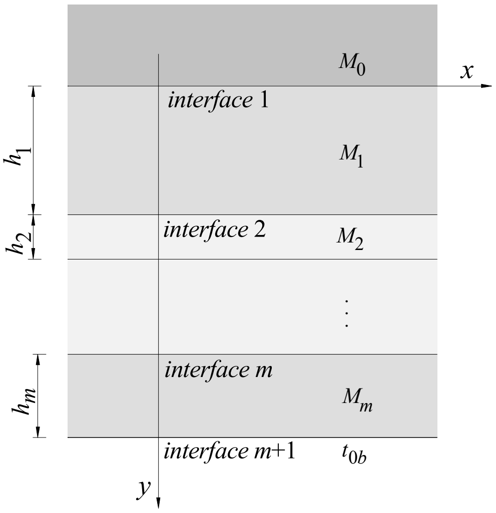

Figure 4.2: Geometry of the problem of a multilayered system bounded by a semi-infinite medium at the top and a prescribed temperature at the bottom.

There is no 3D heat source placed inside the medium, hence the total heat field is given by the sum of the surface terms that are generated at each interface between layers to ensure the continuity of heat flux and temperature. The problem is solved by prescribing a temperature of $\hat{t}_{0b}$, which is obtained by applying a Fourier transform to t_{0b}, at interface m+1 and by ensuring the boundary conditions at the other interfaces. This leads to following system of 2×m+1 equations and 2×m+1 variables:

$$\begin{bmatrix} -1 & -1 & e^{-\mathrm{i}\nu_{01}h_1} & \dots & 0 & 0 \\ \dfrac{1}{\lambda_0\nu_{00}} & -\dfrac{1}{\lambda_1\nu_{01}} & -\dfrac{e^{-\mathrm{i}\nu_{01}h_1}}{\lambda_1\nu_{01}} & \dots & 0 & 0 \\ 0 & e^{-\mathrm{i}\nu_{01}h_1} & -1 & \dots & 0 & 0 \\ 0 & \dfrac{e^{-\mathrm{i}\nu_{n1}h_1}}{\lambda_1\nu_{01}} & \dfrac{1}{\lambda_1\nu_{01}} & \dots & 0 & 0 \\ \dots & \dots & \dots & \dots & \dots & \dots \\ 0 & 0 & 0 & \dots & -1 & e^{-\mathrm{i}\nu_{0m}h_m} \\ 0 & 0 & 0 & \dots & -\dfrac{1}{\lambda_1\nu_{0m}} & -\dfrac{e^{-\mathrm{i}\nu_{0m}h_m}}{\lambda_m\nu_{0m}} \\ 0 & 0 & 0 & \dots & \dfrac{e^{-\mathrm{i}\nu_{0m}h_m}}{\lambda_m\nu_{0m}} & \dfrac{1}{\lambda_m\nu_{0m}} \end{bmatrix} \begin{bmatrix} A_{00}^b \\ A_{01}^t \\ A_{01}^b \\ \dots \\ A_{0m}^t \\ A_{0m}^b \end{bmatrix} = \begin{bmatrix} 0 \\ 0 \\ 0 \\ \dots \\ 0 \\ \hat{t}_{0b} \end{bmatrix}, \qquad (4.18)$$

A^t_{0j} and A^b_{0j} are obtained by solving the system of equations in (4.18). The total heat field in any layer of the domain is obtained by adding the surface terms and is expressed by:

$$\tilde{T}(\omega, y) = E_{0j}\left(\frac{E_{j1}}{\nu_{0j}}A^t_{0j} + \frac{E_{j2}}{\nu_{0j}}A^b_{0j}\right), \qquad (4.19)$$

in which $E_{0j} = 1/\lambda_j$, $\nu_{0j} = \sqrt{-\mathrm{i}\omega/K_j}$, $E_{j1} = e^{-\mathrm{i}\nu_{0j}\left|y-\sum_{l=1}^{j-1}h_l\right|}$ and $E_{j2} = e^{-\mathrm{i}\nu_{0j}\left|y-\sum_{l=1}^{j}h_l\right|}$, where h_l is the thickness of layer l.

4.3 Analytical phase contrast results

This section presents a number of simulations that serve to illustrate how the proposed model can be used to assess the influence that the existence of a given material layer has on the heat field inside a multilayered system. The analytical formulation presented in the previous section is applied to a number of case studies that are of increasing complexity, and for each case study, the effect caused by changing certain parameters (number of layers, defect thermal properties and defect thickness) is investigated.

This is done by modelling the following three distinct cases:

I. *Simple two-layered system of two different materials in which layer M_1 is the layer being studied. Calculations are performed for a receiver placed in layer M_2 at a distance d away from the interface between the two layers and d is changed in order to study the influence of changing the depth at which the layer M_1 is located;*

II. *System of four layers in which layer M_1 is under study. The receiver is placed at the interface between layers M_2 and M_3, and layer M_2 has variable thickness d to study the effect of changing the depth at which the material in layer M_1 is placed. Layer M_3 has a thickness of 0.003* m *and simulates surface thermal resistance. M_4 is an air layer;*

III. *System of seven layers simulating a multi-layered building element consisting of a core material (layer M_4) and a coating material on each side (layers M_3 and M_5). M_4 is the layer under study and layers M_2 and M_6 represent the surface thermal resistance. M_1 and M_7 are layers of air.*

These systems are illustrated in Figure 4.3:

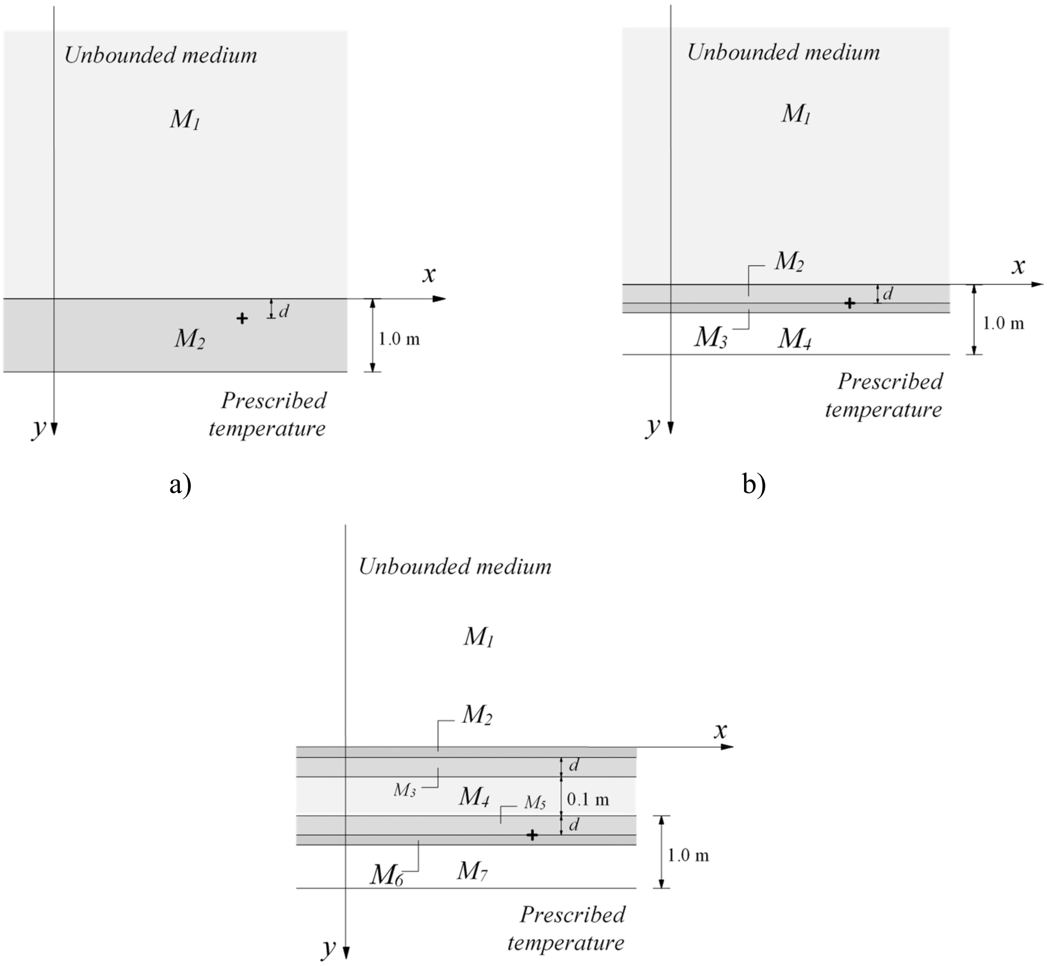

a) b)

c)

Figure 4.3: Geometries of the systems modelled: a) case I; b) case II and c) case III.

In all three cases, the thermal properties of the layer being investigated are changed according to the materials shown in Table 4.1, while the material properties of the rest of the layers remain constant. For each case, in order to simulate a change in the position of the layer under study relative to the surface where temperatures are prescribed, calculations were performed twice, once considering $d = 0.02$ m and then $d = 0.04$ m.

Table 4.1: Thermal properties of the materials considered for the layer being investigated.

Material	Conductivity λ (W/(m.ºC))	Specific heat c (J/(kg.ºC))	Density ρ (kg/m^3)
Insulation Cork Board (ICB)	0.038	1560	100
Medium Density Fibreboard (MDF)	0.12	1550	712
Wood	0.29	1340	900
Gypsum board	0.35	840	900
Basalt	1.6	840	2850
Granite	3.0	840	2600
Steel	55.0	460	7800
Copper	380.0	380	8900

Additionally, in order to better understand potential limits of the phase contrast analysis, calculations are performed for a non-existing material with very low conductivity by considering a material with thermal properties of $\lambda = 0.12\times10^{-4}$ W/(m.ºC), $c = 1550.0$ J/(kg.ºC) and $\rho = 712.0$ kg/m^3. A material with very high conductivity ($\lambda = 380.0\times10^{4}$ W/(m.ºC), $c = 380.0$ J/(kg.ºC) and $\rho = 8900.0$ kg/m^3) was considered. In all calculations, the layer M_2, in cases I and II, and M_3 and M_5, in case III, have the thermal properties of concrete ($\lambda = 1.4$ W/(m.ºC), $c = 880.0$ J/(kg.ºC) and $\rho = 2300.0$ kg/m^3). The air layers are considered to have $\lambda = 0.026$ W/(m.ºC), $c = 1000.0$ J/(kg.ºC) and $\rho = 1.293$ kg/m^3 [35].

Computations are performed considering harmonic sources with unitary amplitude which corresponds to an ideal Dirac pulse in the time domain with an infinite flat spectrum in the frequency domain for a frequency range between 0.0 Hz and 1.024×10^{-3} Hz. Phase results are calculated directly in the frequency domain and thermal wave phase is obtained by the arctangent of the quotient between the imaginary and the real parts of the frequency domain temperature response. Phase contrast in IRT tests is given by the difference between phase recorded in a defective area and a sound area of the thermal image. In this analytical study, phase contrast is obtained by computing the thermal wave phase response in a system containing the layer under study with the thermal properties shown in Table 4.1 (which corresponds to a defect) and a system in which the same layer does not exist, which implies that it is considered to have the same thermal properties of the neighbouring layers (concrete). Phase contrast images cannot be obtained for this application since the entirety of the corresponding surface is a defective zone because the defect is one of the layers with infinite size. Hence, results are presented graphically using phase contrast curves. The graphs in figures 4.4 to 4.6 show the phase contrast results obtained.

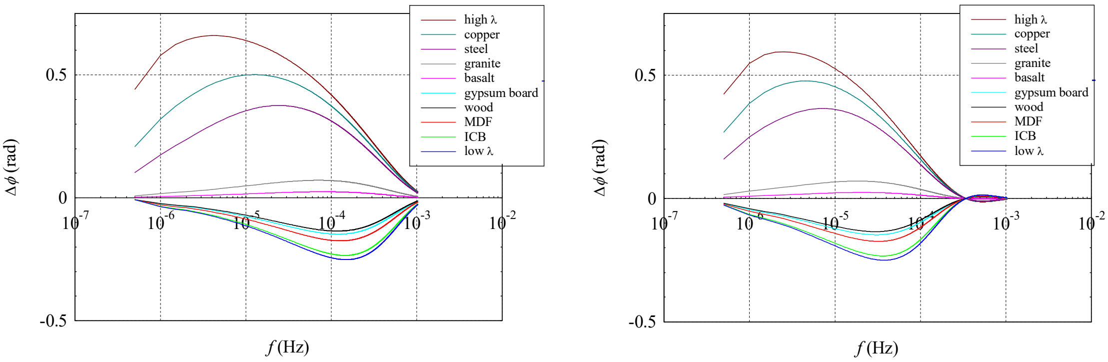

a) b)

Figure 4.4: Case I phase contrast results for: a) receiver placed at $d = 0.02$ m; b) receiver placed at $d = 0.04$ m.

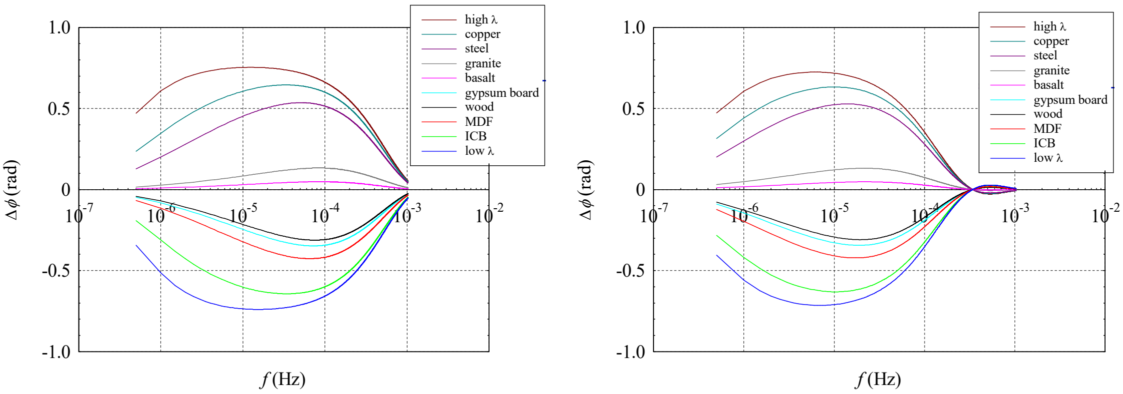

a) b)

Figure 4.5: Case II phase contrast results for: a) layer M_2 with thickness of $d = 0.02$ m; b) layer M_2 with thickness of $d = 0.04$ m.

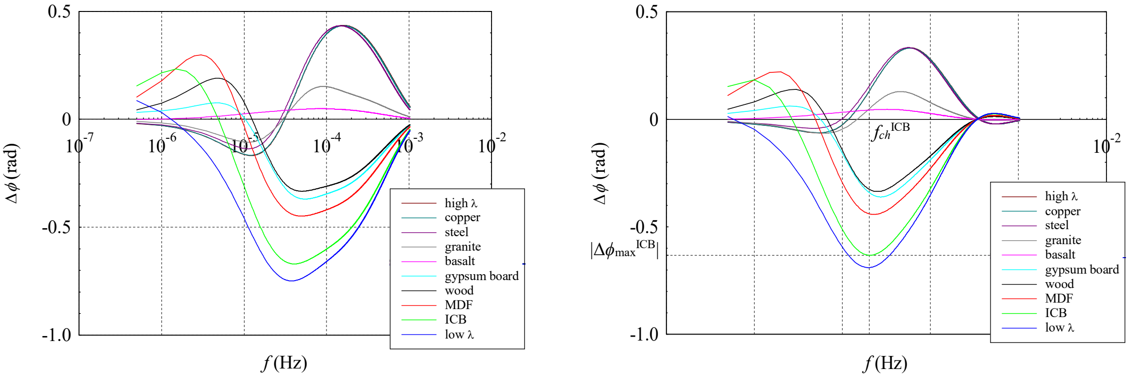

a) b)

Figure 4.6: Case III phase contrast results for: a) layer M_4 located at a depth of $d = 0.02$ m; b) layer M_4 located at a depth of $d = 0.04$ m.

The resulting curves show negative phase contrast for materials with lower conductivity than that of concrete (ICB, MDF, wood, gypsum board) and positive phase contrast for materials with a conductivity higher than that of concrete (basalt, granite, steel, copper). All curves present a peak at the absolute maximum phase contrast $|\Delta\phi_{\max}|$ which corresponds to the characteristic frequency f_{ch} used in experimental defect detection IRT studies to characterize a given defect (see Figure 4.6 for an example for the ICB material located at $d = 0.04$ m). The frequency at null phase contrast, which is referred to as the blind frequency f_b, provides the defect detection threshold in terms of phase image analysis. In particular, for case III, the peak in phase contrast $|\Delta\phi_{\max}|$ is clearly defined. The following table shows the maximum absolute phase contrast results and the corresponding characteristic frequency obtained for this case.

Table 4.2: Case III phase contrast results for the different material properties considered for layer M_4, located at a depth of $d = 0.02$ m and $d = 0.04$ m.

Material	$d = 0.02$ m		$d = 0.04$ m	
	Maximum phase contrast $\lvert\Delta\phi_{\max}\rvert$ (rad)	Characteristic frequency f_{ch} (Hz)	Maximum phase contrast $\lvert\Delta\phi_{\max}\rvert$ (rad)	Characteristic frequency f_{ch} (Hz)
Low λ	-0.749	3.75×10^{-5}	-0.690	1.95×10^{-5}
ICB	-0.670	4.05×10^{-5}	-0.632	2.05×10^{-5}
MDF	-0.449	4.95×10^{-5}	-0.442	2.30×10^{-5}
Wood	-0.333	5.05×10^{-5}	-0.336	2.50×10^{-5}
Gypsum board	-0.370	5.50×10^{-5}	-0.361	2.75×10^{-5}
Basalt	0.049	8.40×10^{-5}	0.046	3.20×10^{-5}
Granite	0.152	9.10×10^{-5}	0.129	4.60×10^{-5}
Steel	0.433	1.46×10^{-4}	0.333	5.65×10^{-5}
Copper	0.433	1.59×10^{-4}	0.331	5.90×10^{-5}
High λ	0.434	1.60×10^{-4}	0.332	5.90×10^{-5}

In the case shown in Table 4.2, as in all cases modelled, the change from $d = 0.02$ m to $d = 0.04$ m generally resulted in a decrease in the characteristic frequency and phase contrast amplitude values. The blind frequency values were also reduced by increasing the depth of the defect.

4.4 Experimental vs analytical results

An experimental campaign was carried out using a test specimen that contains a defect which can be located at varying depth and whose thickness and material properties can change. The frequency resolution of the tests was also changed by performing experiments with different recording times and different frequency of frame acquisition.

In this section, first, the experimental apparatus and test conditions are described, the case study test specimen is presented and then the procedure to obtain phase contrast results is explained. The active IRT tests were performed in a laboratory under controlled conditions and their initial setup was based on the results of preliminary repeatability and reproducibility tests that were carried out to verify the consistency of the results and which are not presented.

Finally, the presented analytical expressions are used to simulate the experimental results. A 1D model of the case study test specimen is used to generate analytical phase contrast curves, which are then compared with the experimental ones. The results are discussed with focus on understanding the effect that changing certain parameters has on phase contrast results obtained in IRT defect detection and characterization studies.

4.4.1 Experimental apparatus

The experiments were performed using a FLIR camera, model A615, which has the following specifications: 640×480 pixel resolution; 7.5-14 μm spectral range; 25°×19° field of view (FOV); 0.68 mrad spatial resolution; thermal sensitivity/noise equivalent temperature difference (NETD) under 0.05 °C at 30 °C and an accuracy of ±2 °C or 2 %. The IRT camera is connected to a control unit (IRX-Box by Automation Technology) and to a computer system with IR NDT 1.74 software. Figure 4.7 illustrates the experimental apparatus. The tests are performed in reflection mode with both the camera and the heat source placed 0.65 m away from the surface of the test specimen (see Figure 4.7). The thermal stimulation of the test specimen was achieved by using two 2500 W halogen lamps and following a rectangular heating function. In each test, thermal images were recorded at a specific rate for a length of time which includes an initial offset period, a heating period and a cooling down period.

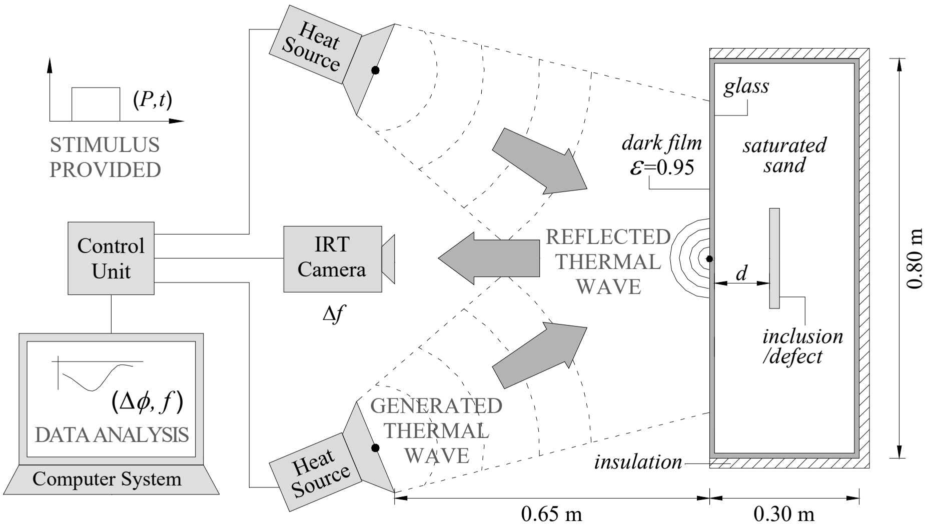

Figure 4.7: Scheme of the experimental apparatus.

4.4.2 Test specimen

A test specimen which simulates a defective building element with changeable features was prepared for the experiments. The specimen is a box made of glass panels (0.006 m thick) filled with saturated sand and containing an inclusion. The sand has thermal properties similar to those of concrete and the inclusion (or defect) is a foreign object made from a material with different thermal properties than those of the saturated sand. A dark film with an emissivity of $\varepsilon = 0.95$ covers the inspected surface of the box and an insulation material is placed along the rest of its boundaries in order to minimize heat flow exchange with the exterior environment. At a distance of 0.65 m, the image recorded by the camera, referred to as the field of view (FOV), is 0.275×0.212 m^2. The centre of the object placed inside the box is aligned with the centre of the field of view, as shown in Figure 4.8, which represents a view of the test specimen surface.

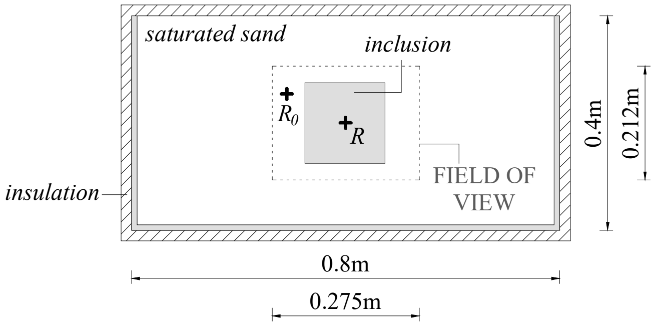

Figure 4.8: Schematic representation of the test specimen.

The sand allows the position of the inclusion to be changed (*i.e.* by changing the defect depth d shown in Figure 4.7) or the object to be easily replaced. Several inclusions of different sizes and made from materials with different thermal properties were used. Tests were conducted using inclusions made from extruded polystyrene foam (XPS), oriented strand board (OSB) and steel. Prior to the IRT experiments, thermal characterization tests were performed to determine the conductivity λ, specific heat c and density ρ of the materials used in the test specimen, except for glass and steel [35]. The guarded hot plate method according to EN 12664:2001 and EN 12667:2001 was used for thermal conductivity and the ratio method using differential scanning calorimetry was used to determine specific heat. The determination of density was performed from the measurements of linear dimensions and mass, after conditioning to constant mass at 23 ºC and 50 % relative humidity. These tests were performed for three different samples of each material, resulting in the average values given in Table 4.3.

Table 4.3: Properties of the test specimen materials.

Material	Conductivity λ (W/(m.ºC))	Specific heat c (J/(kg.ºC))	Density ρ (kg/m^3)
Glass	1.0	750	2500
XPS	0.033	1450	30
OSB	0.106	1700	423
Steel	55.0	460	7800
Saturated sand	1.840	1030	1850

4.4.3 Experimental data acquisition

A total of 128 thermal images were recorded for 4096 s in each test. Phase results were calculated for every pixel in the FOV, henceforth called receivers, by applying a Fourier transform to the temperature results recorded in the time domain. For each receiver, phase contrast was determined by computing the difference between the phase recorded at this receiver and the phase recorded at another receiver located in a sound area that is not influenced by the defect. For example, the phase contrast for a receiver R located at the centre of the recorded image (see Figure 4.8) is the difference between the thermal wave phase computations for receiver R and R_0.

4.4.4 Analytical simulation

In order to model the test specimen used in the experiments, the proposed analytical heat diffusion model based on Green's functions was used to simulate heat diffusion in a system of nine layers of infinite extent in the x and z directions. The system is represented in Figure 4.9. A layer located at the centre represents an inclusion (or defect) with thickness h which is bounded by two layers of sand with variable thickness. The dimension d represents the depth at which the inclusion is located, *i.e.* its distance from the glass. The layers of sand are enclosed by 0.006 m thick glass panels. The thermal properties used in the analytical study are those of the experimental case study, which were determined by characterization tests, and are shown in Table 4.3. Surface thermal resistance was taken into account by assuming a thin outer layer of air with the following thermal properties: $\lambda = 0.026$ W/(m.°C), $c = 1000.0$ J/(kg.°C) and $\rho = 1.293$ kg/m^3 [35].

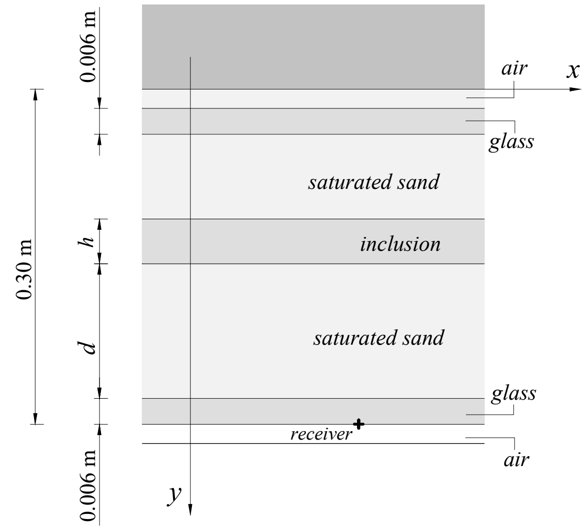

Figure 4.9: Geometry of the analytical model of the experimental IRT test specimen.

To mimic the results obtained in IRT experiments, calculations were performed for a receiver located in the interface between the glass and the surface air layer (see Figure 4.9) and by prescribing a temperature of 10 ºC at the bottom interface, which correspond to the test specimen's surface in IRT experiments.

4.4.5 Results and discussion

In the next few paragraphs the main results obtained in the analytical and experimental studies are compared. The experimental phase contrast curves were generated from the phase contrast results recorded by the receiver at the centre of the FOV (receiver R in Figure 4.8), since this is where phase contrast is likely to be greater. The influence that changing test parameters (defect depth, thickness and thermal properties, and test acquisition) has on the experimental results is compared with the one obtained analytically.

4.4.5.1 Influence of defect depth

The curves in Figure 4.10 a) show the phase contrast results of several tests with the defect located at different depths. In each test a 20×20×4 cm^3 XPS inclusion was placed away from the inner surface of the glass at $d = 0.005$ m, $d = 0.01$ m, $d = 0.015$ m, $d = 0.02$ m and $d = 0.04$ m. The acquisition rate was set to 0.03125 Hz and the specimen was heated for a period of 200 s.

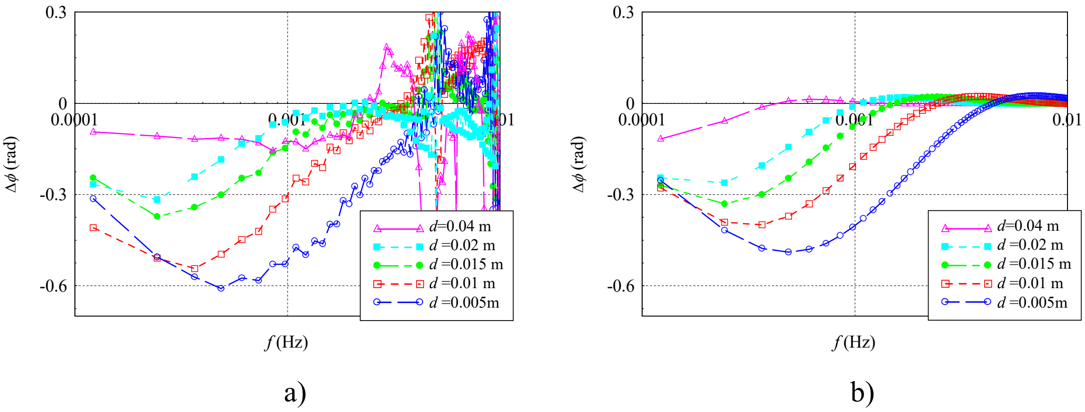

Figure 4.10: Phase contrast for an XPS inclusion located at varying depths: a) experimental results for a 20×20×4 cm^3 XPS board; b) analytical results for a 4 cm XPS layer.

The experimental results in Figure 4.10 a) show that increasing the depth of the inclusion leads to a decrease in the characteristic frequency f_{ch}, the maximum phase contrast $|\Delta\phi_{\max}|$ and the blind frequency f_b . This confirms the results obtained in the previous analytical study in 4.3. At higher frequencies, the results become irregular and the blind frequency value is more difficult to determine. These phase contrast oscillations at the higher frequencies are related to the presence of noise in the recorded experimental data. An analysis of the influence of noise is presented later on in this study in 4.4.5.5.

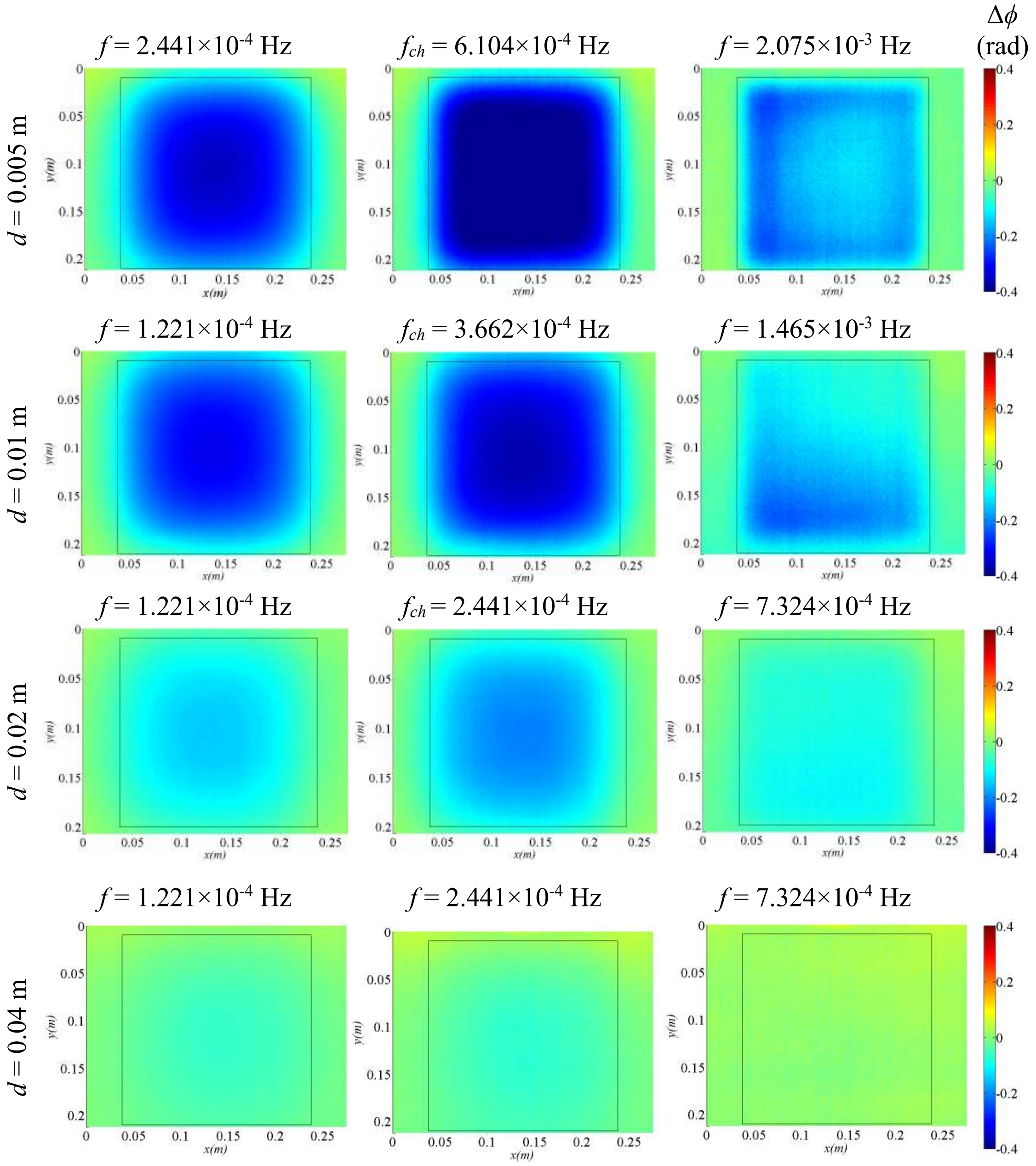

Figure 4.11: Experimental phase contrast image results, in radians, for a test specimen with a $20\times20\times4$ cm^3 XPS inclusion located at $d = 0.005$ m, $d = 0.001$ m, $d = 0.02$ m and $d = 0.04$ m, taken at several frequencies.

The curve for $d = 0.04$ m does not show a peak in phase contrast, which indicates that when a certain depth is reached the inclusion is no longer visible in the phase contrast images, meaning that the defect is no longer easily detected in the selected frequency range.

The curves in Figure 4.10 b) correspond to the results obtained using the analytical expressions, without taking into account any noise. The analytical results have a similar behaviour to the experimental ones in Figure 4.10 a) regarding the influence of changing the depth of the inclusion. Both the analytical and experimental results seem to indicate that defects which are closer to the surface are more visible, and that their peak occurs at higher frequencies.

To better perceive the experimental results, Figure 4.11 shows the phase contrast images that are at the origin of the phase contrast curves presented in Figure 4.10 a) for the inclusion placed at several different depths inside the specimen. The phase contrast images at the central plot correspond to the frequency for which the phase contrast peaked, and the other frequencies were selected arbitrarily to illustrate the phase contrast evolution along the frequency increment. For the case of the deeper defect the phase contrast signal is very reduced and the characteristic frequency could not be estimated.

4.4.5.2 Influence of defect thickness

Figure 4.12 illustrates the effect of changing the thickness of the inclusion. Tests were performed using two XPS boards of different thicknesses: one was 20×20×4 cm^3 and the other was 20×20×2 cm^3. Both were placed at a depth of $d = 0.005$ m and tested using an acquisition rate of 0.03125 Hz.

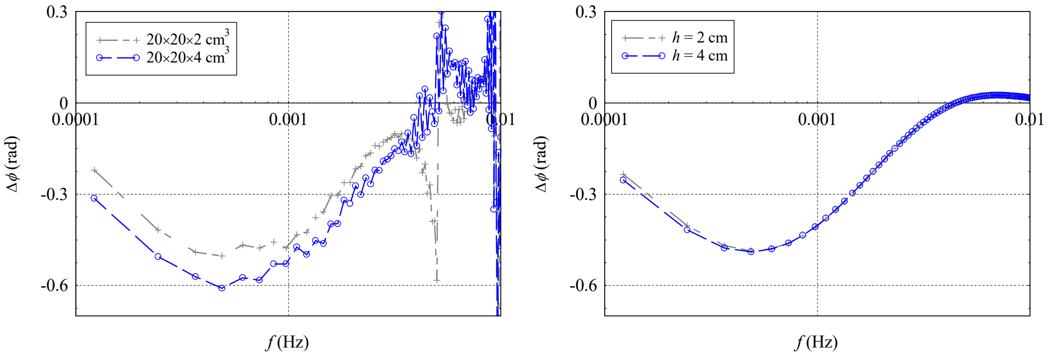

a) b)

Figure 4.12: Phase contrast for an XPS board inclusion of varying thickness: a) experimental results; b) analytical results.

In Figure 4.12 a), the result for the thinner inclusion showed a slight decrease in phase contrast for all frequencies, even though the evolution of the graph is similar. These results indicate that a thinner defect will be less visible in phase contrast images. In the analytical results this disparity is more moderate and only visible in the lower frequencies.

4.4.5.3 Influence of defect material

Tests were performed using 20×20×2 cm^3 XPS, OSB and steel inclusions which were placed inside the specimen at a depth of d = 0.005 m. The results in Figure 4.13 a) show the experimental phase contrast behaviour of the different material inclusions. The test time for all specimens was 4096 s (200 s heating and recording at an acquisition rate of 0.03125 Hz).

Materials with thermal conductivity lower than that of sand have a negative phase contrast with a clearly defined peak, while the phase contrast curve of steel is inverted. The analytical results confirm what was observed in the former analytical study, *i.e.* that materials whose conductivity is lower than sand (XPS and OSB) produce negative phase contrast results whereas steel, whose conductivity is greater than that of sand, yields positive phase contrast results.

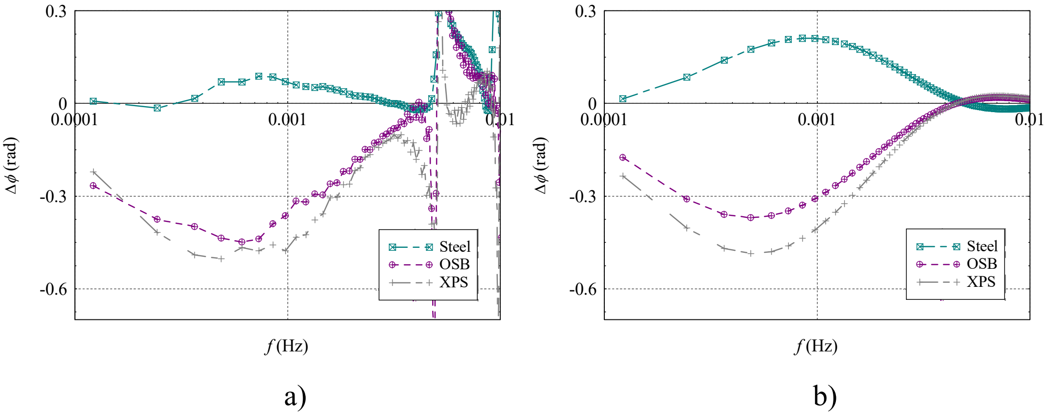

Figure 4.13: Phase contrast for inclusions of different materials: a) experimental results; b) analytical results.

4.4.5.4 Influence of frame acquisition rate

The results in Figure 4.14 a) illustrate the influence of using different rates of frequency resolution. One curve corresponds to a test duration of 4096 s at an acquisition rate of 0.03125 Hz, the other to an 8192 s test with 0.015625 Hz. Both tests were performed for a 20×20×4 cm^3 XPS inclusion placed at $d = 0.005$ m.

The curve corresponding to the longer test exhibits a slightly higher maximum phase contrast, which occurs at a slightly lower characteristic frequency. This behaviour is made clearer by the analytical results. As expected, the longer recording time provides curves that are more discretized in the lower frequencies. This can be quite useful when analysing deeper defects, since the peak in phase contrast occurs at lower frequencies (see Figure 4.10 in 4.4.5.1).

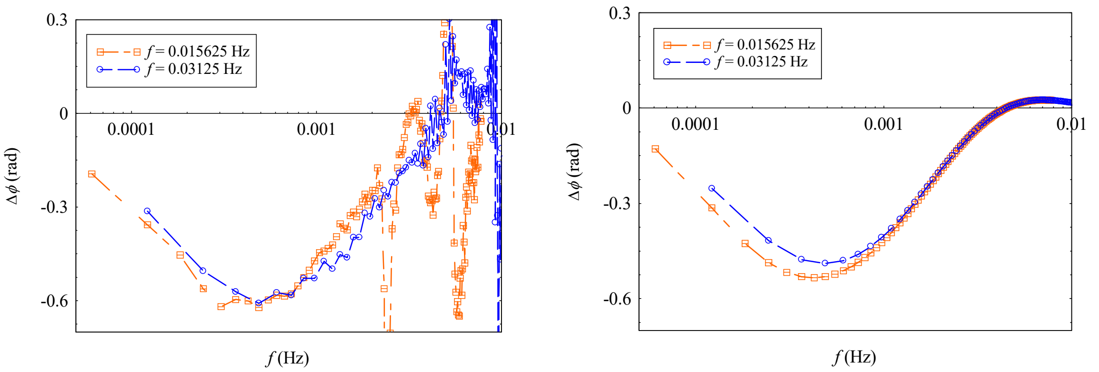

a) b)

Figure 4.14: Phase contrast for different frame acquisition rates: a) experimental results; b) analytical results.

4.4.5.5 Presence of noise

Even under uniform radiation, the temperature recorded by the IRT camera for each pixel oscillates in time. These fluctuations, known as temporal noise, are related to the sensitivity of the IRT camera and other factors such as environmental conditions and surface emissivity. To verify its influence in the phase contrast results obtained, a random temperature variation defined within a certain interval was added to the time response obtained analytically.

The analytical expressions were used to compute thermal phase results directly in the frequency domain and transient temperature results were obtained by performing an inverse fast Fourier transform to the frequency domain results. Then, random temperature increments of ±0.03 °C,

±0.05 °C, ±0.08 °C and ±0.2 °C were added to the time domain results and phase contrast results were again obtained by applying a Fourier transform to the transient temperature results. Figure 4.15 shows the influence that the presence of noise has on analytical phase contrast results, calculated for an XPS inclusion located at $d = 0.005$ m.

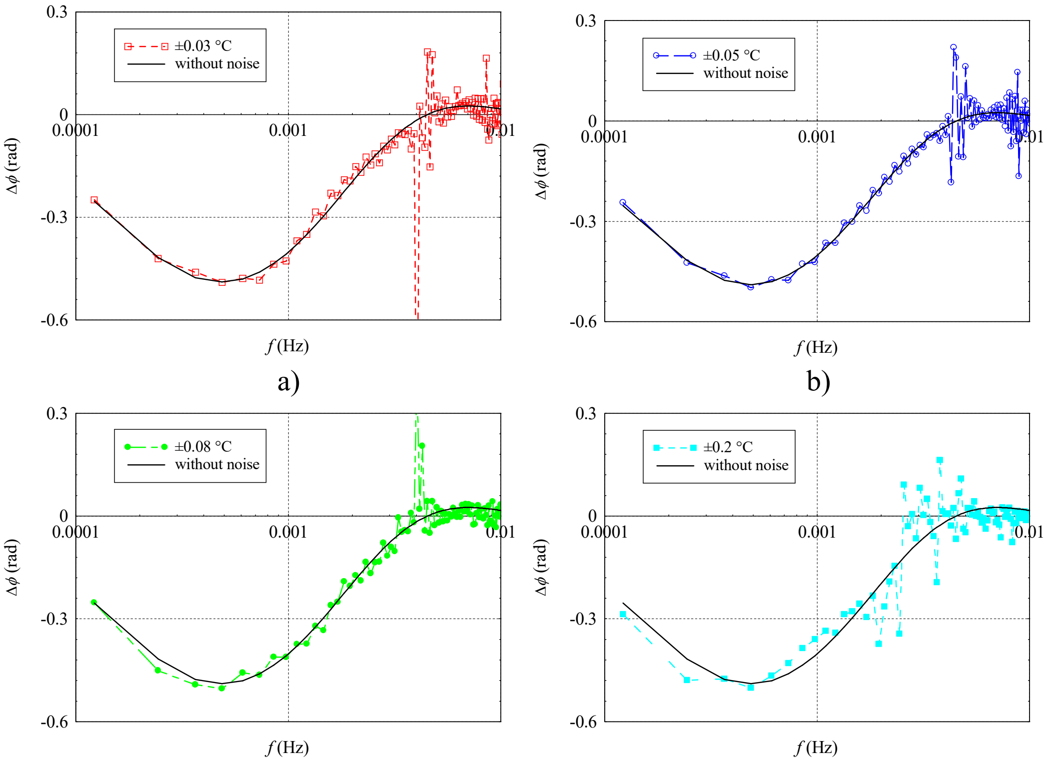

a) b) c) d)

Figure 4.15: Analytical phase contrast result for an XPS layer located at d = 0.005 m with varying levels of noise: a) ±0.03 °C; b) ±0.05 °C; c) ±0.08 °C and ±0.2 °C.

The results in Figure 4.15 illustrate the fact that the presence of noise is most noticeable at the higher frequencies, where the phase contrast oscillates significantly, even for the smallest temperature intervals. It can be seen that throughout the whole frequency spectrum the greater the imposed random noise temperature, the greater the influence on phase contrast.

4.5 Final statements

In this study, analytical expressions based on Green’s functions for modelling heat transfer by conduction in multilayered media were used to simulate the experimental phase contrast results obtained in active IRT tests performed on test specimens that use relative low conductivity materials, similar to those present in building elements.

A set of active IRT tests were performed on a test specimen with an inclusion (defect) with variable characteristics and a multilayered system was used to model a defective building element. The influence of the presence of a given inclusion, corresponding to a defined layer in the multilayered system, was studied using a phase contrast approach. The phase contrast was obtained directly in the frequency domain by calculating the difference between the thermal wave phase results computed for a system with m layers and a system with $m-1$ layers (the layer that is removed is the layer which represents the defect. A number of experimental and analytical phase contrast curves were generated for different test conditions and defect characteristics. Then, the analytically generated phase contrast curves were compared with those obtained experimentally.

The obtained results indicate that the proposed analytical model may provide a reasonable approximation to the experimental results since, in all cases, both the experimental and analytical curves led to the same conclusions. Regarding the influence of depth of the defect, the results clearly demonstrated the potential that phase contrast curves analysis has for estimating the location of defects or inclusions effectively. Regarding the experimental procedure, it can be said that using a slower frame acquisition rate (provided by a longer recording time) led to better results since the phase contrast curves were defined more clearly at the lower frequencies and the registered maximum phase contrast was higher. This suggests that problems in finding and characterizing certain defects can be resolved by performing longer tests, hence decreasing the acquisition rate.

It can be said that the analytical curves were able to predict the frequency range over which the defect was detectable and provided a reasonable approximation to the phase contrast amplitude. In addition, the analytically generated curves benefit from not being affected by the noise associated with the IRT camera. The experimental and analytical results yielded curves with similar behaviour, leading to the conclusion that the consideration of an inclusion or defect as an infinite layer in a multilayered model and the simplification of a planar heat source generated reasonable results, provided that the experiments are sufficiently long and the heating of the surface is uniform. It is concluded that analytical expressions for heat diffusion simulation in layered systems can effectively contribute to the interpretation of quantitative data results from active IRT tests on building envelopes with defects or inclusions.

Analytical phase contrast curves can provide insight into the influence of certain defect characteristics, which is crucial for carrying out defect evaluation studies. These can be particularly useful for defining IRT test procedures, since they allow the definition of the characteristic frequency and blind frequency of a defect without noise.

Additionally, the potential for using phase contrast curves analysis in studies focused on thermal characterization of building elements should be explored, since many follow a layered configuration.

References

[1] Maldague X., Introduction to NDT by Active Infrared Thermography, Materials Evaluation, Vol. 6 (9), pp. 1060-1073, 2002.

[2] Maldague X., Theory and Practice of Infrared Technology for Non-destructive Testing, John Wiley & Sons, 2001.

[3] Balaras C.A., Argiriou A.A., Infrared thermography for building diagnostics, Energy and Buildings, Vol. 34, pp. 171-183, 2002.

[4] Grinzato E., Vavilov V., Kauppinen T., Quantitative infrared thermography in buildings, Energy and Buildings, Vol. 29, pp. 1-9, 1998.

[5] Balageas D.L., Krapez J.C., Cielo P., Pulsed photothermal modelling of layered materials, Journal of Applied Physics, Vol. 59 (2), pp. 348-357,1986.

[6] Busse G., Wu D., Karpen W., Thermal Wave Imaging with Phase Sensitive Modulated Thermography, Journal of Applied Physics, Vol. 71 (8), pp. 3962-3965, 1992.

[7] Balageas D., Defense and illustration of time-resolved pulsed thermography for NDE, Quantitative InfraRed Thermography Journal, Vol. 9 (1), pp. 3-32, 2012.

[8] Vavilov V., Marinetti, S., Thermal Methods pulsed phase thermography and Fourier-analysis thermal tomography, Russian Journal of Nondestructive Testing, Vol. 35 (2), pp. 134-145, 1999.

[9] Busse, G., Eyerer, P., Thermal wave remote and nondestructive inspection of polymers, Applied Physics Letters, Vol. 43 (4), pp. 355–357, 1983.

[10] Maldague X, Marinetti S., Pulse phase infrared thermography, Applied Physics, Vol. 79 (5), pp. 2694-2698, 1996.

[11] Ibarra-Castanedo C., Maldague X., Pulsed phase thermography reviewed, Quantitative InfraRed Thermography Journal, Vol. 1 (1), pp. 47-70, 2004.

[12] Ibarra-Castanedo C., González D., Klein M., Pilla M., Vallerand S., Maldague X., Infrared image processing and data analysis, Infrared Physics & Technology, Vol. 46 (1-2), pp. 75 83, 2004.

[13] Kylili A., Fokaides P.A., Christou P., Kalogirou S.A, Infrared thermography (IRT) applications for building diagnostics: A review, Applied Energy, Vol. 134, pp. 531-549, 2014.

[14] Maierhofer Ch, Brink A, Röllig M, Wiggenhauser H. Transient thermography for structural investigation of concrete and composites in the near surface region. Infrared Physics & Technology, Vol. 43 (3), pp. 271-278, 2002.

[15] Maierhofer Ch., Brink A., Röllig M., Wiggenhauser H., Detection of shallow voids in concrete structures with impulse thermography and radar, NDT&E International, Vol. 36, pp. 257–263, 2003.

[16] Maierhofer Ch., Wiggenhauser H., Brink A., Röllig M., Quantitative numerical analysis of transient IR-experiments on buildings, Infrared Physics & Technology, Vol. 46 (1-2), pp.173-180, 2004.

[17] Maierhofer Ch., Brink A., Röllig M., Wiggenhauser H., Quantitative impulse-thermography as non-destructive testing method in civil engineering - experimental results and numerical simulations, Construction and Building Materials, Vol. 19 (10), pp. 731-737, 2005.

[18] Maierhofer Ch., Arndt R., Röllig M., Influence of concrete properties on the detection of voids with impulse-thermography Infrared Physics & Technology, Vol. 49 (3), pp. 213-217, 2007

[19] Meola C., Infrared thermography of masonry structures, Infrared Physics & Technology, Vol. 49, pp. 228-233, 2006.

[20] Laurenti L., Marcotullio F., Monte F., Determination of the thermal resistance of walls through a dynamic analysis of in-situ data, International Journal of Thermal Science, Vol. 43, pp. 297-306, 2004.

[21] Bison P., Grinzato E., Fast estimate of solid materials thermal conductivity by IR thermography, Quantitative InfraRed Thermography Journal, Vol. 7 (1), pp. 17-34, 2010.

[22] Wiggenhauser H., Active IR-applications in civil engineering, Infrared Physics & Technology, Vol. 43 (3-5), pp. 233-238, 2002.

[23] Tavukçuoğlu A., Grinzato E., Determination of critical moisture content in porous materials by IR thermography, Quantitative InfraRed Thermography Journal, Vol. 3 (2), pp. 231-245, 2006.

[24] Arndt R.W., Square pulse thermography in frequency domain as adaptation of pulsed phase thermography for qualitative and quantitative applications in cultural heritage and civil engineering, Infrared Physics & Technology, Vol. 53 (4), pp. 246-253, 2010.

[25] Carslaw H.S., Jaeger J.C., Conduction of Heat in Solids, Oxford University Press, Vivian Ridler, Walton Street, Oxford, 2nd edition, 1959.

[26] Bathe K.J., Numerical Methods in Finite Element Analysis, Prentice-Hall, New Jersey, 1976.

[27] Brebbia C.A., Telles J.C., Wrobel L.C., Boundary Elements Techniques: Theory and Applications in Engineering, Springer-Verlag, Berlin-New York, 1984.

[28] Özisik M.N., Finite Difference Methods in Heat Transfer, CRC Press Inc., USA, 1994.

[29] Özisik M.N., Heat Conduction, second edition, John Wiley & Sons, New York, 1993.

[30] Haji-Sheikh A., Beck J.V., Temperature solution in multi-dimensional multi-layer bodies. International Journal of Heat Mass Transfer, Vol. 45 (9), pp. 1865–1877, 2002.

[31] Tadeu A., António J., Simões N., 2.5D Green's functions in the frequency domain for heat conduction problems in unbounded, half-space, slab and layered media. Computer Modelling in Engineering and Sciences-CMES Vol. 6 (1), pp. 43-58, 2004.

[32] Tadeu A., Simões N., Three-dimensional fundamental solutions for transient heat transfer by conduction in an unbounded medium, half-space, slab and layered media. Engineering Analysis with Boundary Elements, Vol. 30 (5), pp. 338–349, 2006.

[33] Simões N., Simões I., Tadeu A., Vasconcellos C.A.B., Mansur W.J., 3D Transient heat conduction in multilayer systems - Experimental validation of semi-analytical solution. International Journal of Thermal Sciences, Vol 57, pp. 192-203, 2012.

[34] Vavilov V., Noise-limited thermal/infrared nondestructive testing, NDT&E International, Vol 61, pp. 16–23, 2014.

[35] Mills A.F., Heat Transfer, Second Edition, Prentice Hall, New Jersey, 1999.

CHAPTER 5

MODELLING OF HEAT DIFFUSION IN DEFECTIVE MULTILAYERED MEDIA FOR IRT APPLICATIONS

5 MODELLING OF HEAT DIFFUSION IN DEFECTIVE MULTILAYERED MEDIA FOR IRT APPLICATIONS

5.1 Introduction

Over the previous chapters, the need to develop modelling tools to simulate infrared thermography (IRT) applications in buildings has been substantiated. It is worth emphasizing that, although several testing and data processing techniques have been developed for active IRT studies in other areas, in the building sector its use remains sparse, in part due to a lack of testing and data processing techniques specific for construction materials. IRT in buildings is still used mainly to assess the quality of a building envelope in steady state [1]. However, it is known that the analysis of thermal data obtained in a transient regime combined with the development of numerical models to simulate transient heat phenomena can be useful to characterize and evaluate defects [2]. Furthermore, it is also known that IRT data analysis in the frequency domain can be advantageous, since phase contrast images have demonstrated greater potential for detectability as well as other benefits [3]. Nonetheless, because the heat field that propagates near a defect depends on a combination of factors (defect depth, defect size, material properties, heating and data acquisition methods), interpreting IRT results for defect characterization presents many challenges. Hence, the development of simulation tools that successfully replicate the heat transfer phenomena within the material while taking these factors into account is crucial for the advancement of this technique.

The interest in performing predictive maintenance in ageing buildings and structures to cut down the cost of repairs and in improving energy efficiency to reduce consumption is ever growing, which reinforces the need for further research into IRT applications in buildings. And, since many constructive systems and building elements follow a layered configuration, it can also be said that the interest in studying heat transfer in multilayered systems is becoming more and more relevant. With this in mind, and aiming to contribute to the interpretation of experimental IRT results obtained in buildings, in the present chapter a numerical model is proposed for the simulation of 3D heat diffusion in multilayered solid media containing 3D thin defects.

In the previous chapter, looking to contribute to the interpretation of experimental IRT performed on buildings elements, the thermal wave phase response in defective solid media was simulated using a simple 1D multilayered model in which the defect is considered to be an infinite layer and the heating source is accomplished by imposing uniform temperature. In this chapter, a more realistic (complex) geometry is attempted and a simulation model for 3D heat diffusion in layered solid media containing a 3D thin defect is presented. In this system, the heat field in the media will be affected, not only by the presence of a defect, but also by the existence of the interfaces that separate the different layers of the system which may have different material properties and thickness. In the previous chapter it was considered the case in IRT tests in which uniform heating of the specimen surface is achieved. However, in addition, the influence of a 3D heat source needs to be considered.

In the presence of heterogeneities, such as 2D or 3D inclusions located within otherwise homogeneous layers, numerical models are required. Boundary element [4] based formulations have been selected to be developed and implemented along the present thesis because, when compared with other popular discretization based techniques, such as the finite elements method [5] or the finite difference method [6], the boundary element method presents the clear advantage of only requiring the discretization of the boundary of the inclusion being modelled.

Frequency domain analytical expressions for 3D heat diffusion in unbounded, semi-infinite, slab and layered media subjected to a 3D point heat source using Green's functions have been provided by Tadeu and Simões [7] using 3D fundamental solutions, and by Tadeu *et al*. [8] using a 2.5D problem formulation to reduce the 3D problem by considering linear harmonic sources with varying wavenumber along one direction using a spatial Fourier transformation, which is useful for solving cylindrical 2D geometries. For 3D geometries, an additional spatial Fourier transformation along the perpendicular direction (x) allows the solution to be obtained as a double sum of 1D solutions. An alternative simplification of the 3D problem is to consider the transformations given by Sommerfeld [9] and Ewing and Jardetzky [10] to obtain Bessel integrals, which can be solved considering a finite sum of equally spaced heat sources along one direction. This allows 3D solutions to be obtained as a single sum of solutions with varying wavenumbers along the layered normal direction.

The inclusion being modelled simulates a very thin defect (crack or delamination in a building element) and is assumed in the calculations to have null thickness and null heat flux through it. Therefore, when applying the BEM formulation to this case, the inclusion is discretized as a closed surface. This requires the existence of elements (with opposite normal directions) that coincide. However, under these conditions the BEM degenerates. Several authors have proposed solutions to this problem, such as the hypersingular formulation [11] or the dual boundary element method [12]. In this study, in order to handle the thin defect, the BEM is written in terms of a normal derivative integral equation (TBEM) which is obtained by applying the gradient operator to the classical boundary integral equation and assuming the existence of dipole heat sources. This procedure allows the surface of the inclusion to be discretized as an open surface. However, when using the TBEM formulation, if the element being integrated is the loaded element, hypersingular integrals appear. In order to solve these singularities, known analytical solutions which have been previously validated [13] are used.

The proposed formulation for defective multilayered media is verified against the previously developed 3D TBEM model for heat diffusion in the presence of thin defects in unbounded media [14]. In order to allow the verification, the 3D TBEM model for unbounded media is modified to compute half-space media using a mirror image source technique. This verification is then followed by an application of the proposed model to illustrate its usefulness in active IRT tests that use the phase contrast approach to characterize defects. In order to do so, the numerical model is applied to multilayered systems with defects located at several depths. Once more, the term phase contrast refers to the difference between the thermal wave phase recorded in a defective area and the thermal wave phase recorded in a sound area.

While simulations make it possible to compute phase contrast using the entire domain as a reference for sound media, in real IRT tests the selection of a specific sound zone is necessary. The thermal response anywhere in the domain is dependent on the distance to the heat source, therefore, thermal wave phase results are affected by the 3D point heat source position. Hence, considering a single point in the thermal image to be used as the reference for sound media can carry considerable errors. In this study, in order to evaluate this consideration phase contrast is obtained using two approaches. First, results are computed using the multilayered media without the defect, which will be used as a reference for sound media. Since the inclusion is absent, there is no need to use the BEM and the purely analytical model is used to solve the multilayered system. Then, phase contrast is computed considering a specific pixel located in an area of the thermal image which is considered to be weakly influenced by the presence of the defect. These two approaches are compared and a correction technique to remove the influence of the location of the heat source is presented.

Experimental active IRT tests performed on specimens that have more than one layer are also presented in this chapter. The test specimens contain thin defects located at different depths and their layers are made from different materials common in building systems. Hence, the tests are performed using a long pulse and prolonged recording time, as suggested by Vavilov *et al.* [15] and supported by Maierhofer *et al.* [16] and Ardnt [17], in order to account for the slow response of the building materials. Looking to take advantage of the benefits presented by phase images, these experimental results are also presented in terms of phase contrast.

In the next section of this chapter (Section 5.2), first the 3D TBEM model to simulate a multilayered system subjected to a 3D point heat source that contains a 3D thin defect is formulated in the frequency domain. The problem is fully described and its verification against the 3D TBEM model formulated for unbounded media with thin defects (in Chapter 2) is presented. Afterwards, a numerical application is performed to study systems with defects at several depths. The procedure to obtain phase contrast is also described and the influence of choosing a single sound pixel as a reference for phase contrast calculations in the presence of a 3D point heat source is studied.

Then, in Section 5.3 the experimental results are presented for test specimens with thin defects placed at several depths, and are compared with the numerically obtained results for modelling systems that correspond to the test specimens. From the phase contrast results, by extracting the response for a specific receiver (corresponding to a pixel in the image captured by an IRT camera) phase contrast curves, which are the graphical representation of phase contrast in the frequency domain that characterizes a given defect, are obtained and studied.

5.2 Numerical model

Consider a system of *m* parallel layers bounded by semi-infinite media (medium M_0 at the top and M_{m+1} at the bottom) containing a thin defect. The defect being modelled is a null thickness inclusion with surface *S*, whose size, shape and position can vary. The layers are infinite in the *x* and *z* directions and can each present different thickness, as well as different thermal properties. Each layer *j* has thermal conductivity λ_j, density ρ_j, specific heat capacity c_j and thermal diffusivity K_j. The system is subjected to a 3D point heat source placed somewhere in the domain at $\boldsymbol{x}_s = (x_s, y_s, z_s)$. This system is illustrated in Figure 5.1.

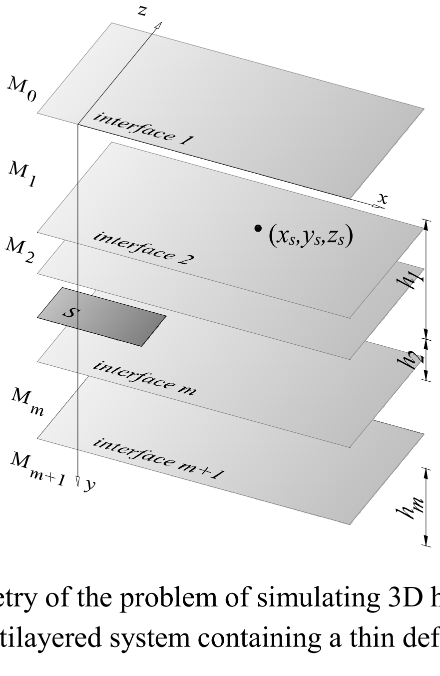

Figure 5.1: Geometry of the problem of simulating 3D heat diffusion in a multilayered system containing a thin defect.

5.2.1 Heat diffusion in unbounded solid media

First consider an unbounded isotropic solid medium. In cartesian coordinates, 3D transient heat diffusion in any point $\boldsymbol{x}=(x,y,z)$ is given by the following equation:

$$\left(\frac{\partial^2}{\partial x^2}+\frac{\partial^2}{\partial y^2}+\frac{\partial^2}{\partial z^2}\right)T(t,\boldsymbol{x})=\frac{1}{K}\frac{\partial T}{\partial t}. \tag{5.1}$$

$T\,(t,\boldsymbol{x})$ is temperature, t is time and K is the thermal diffusivity of the unbounded medium which is given by $K=\lambda/(\rho\,c)$, in which λ is thermal conductivity, ρ is density and c is specific heat capacity. By applying the Fourier transform to this equation, 3D heat diffusion in the frequency domain is obtained:

$$\left(\frac{\partial^2}{\partial x^2}+\frac{\partial^2}{\partial y^2}+\frac{\partial^2}{\partial z^2}+\left(\sqrt{-\frac{\mathrm{i}\omega}{K}}\right)^2\right)\hat{T}(\omega,\boldsymbol{x})=0, \tag{5.2}$$

where $\hat{T}(\omega,\boldsymbol{x})$ is temperature in the frequency domain, ω is angular frequency and $\mathrm{i}=\sqrt{-1}$.

Considering a 3D point heat source placed at $\boldsymbol{x}_s=(x_s,y_s,z_s)$ expressed by $p(t,\boldsymbol{x})=P\,\delta(x-x_s)\delta(y-y_s)\delta(z-z_s)e^{\mathrm{i}\omega t}$, where $\delta(x-x_s)$, $\delta(y-y_s)$ and $\delta(z-z_s)$ are Dirac delta functions and P is its amplitude, the 3D heat source response can be given by the following incident heat field:

$$\hat{T}_{inc}(\omega,\boldsymbol{x})=\frac{P\,e^{-\mathrm{i}k_c r_s}}{2\lambda r_s}, \tag{5.3}$$

in which $k_c=\sqrt{-\mathrm{i}\omega/K}$ and the distance to the source is $r_s=\sqrt{(x-x_s)^2+(y-y_s)^2+(z-z_s)^2}$.

Equation (5.3) can be expressed as a Bessel integral using the procedure proposed by Sommerfeld [9] and by Ewing and Jardetzky [10]:

$$\hat{T}_{inc}(\omega,\boldsymbol{x})=\frac{-\mathrm{i}P}{2\lambda}\int_0^\infty \mathrm{J}_0\left(k_y\,\bar{r}_s\right)\frac{k_y e^{-\mathrm{i}\sqrt{-(\mathrm{i}\omega/K)-k_y^2}\,|y-y_s|}}{\sqrt{-\mathrm{i}\omega/K-k_y^2}}\mathrm{d}k_y, \tag{5.4}$$

in which $\mathrm{J}_{\alpha}(\ )$ are Bessel functions of order *α*, k_y is the wavenumber in the *y* direction and $\bar{r}_s = \sqrt{(x-x_s)^2 + (z-z_s)^2}$. Assuming the existence of virtual heat sources equally spaced by L_y along the y axis, this integral can be expressed by the following discrete sum:

$$\hat{T}_{inc}(\omega, \boldsymbol{x}) = \frac{-\mathrm{i}\pi P}{L_y \lambda} \sum_{n=1}^{N} \mathrm{J}_0(k_n \bar{r}_s) \frac{k_n}{v_n} e^{-\mathrm{i}v_n|y-y_s|}, \tag{5.5}$$

with $v_n = \sqrt{-\mathrm{i}\omega/K - k_n^2}$, $k_n = 2\pi n/L_y$. The distance L_y must be big enough so as to prevent spatial contamination from the virtual sources.

5.2.2 Analytical solution for multilayered media

Next consider a multilayered system of *m* layers infinite in the *x* and *z* axes directions and bounded in the *y* direction by semi-infinite media at the top and at the bottom, which is illustrated in Figure 5.2. The system is sound, meaning that it does not contain any defects, and is subjected to a 3D point heat source placed anywhere in the domain.

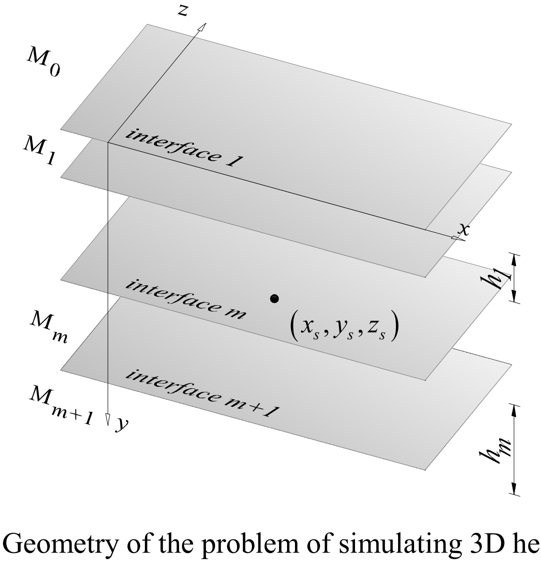

Figure 5.2: Geometry of the problem of simulating 3D heat diffusion in a sound multilayered system.

In multilayered media, it is necessary to take into account both the incident heat field that comes directly from the 3D source, as well as the heat field which results from the presence of the interfaces between the different layers.

Hence, the total heat field in the system is given by the sum of the source terms in Equation (5.5) and the surface terms that are generated at each interface in order to ensure the continuity of heat flux and temperature between layers.

The pair of surface terms that are generated at each interface by imposing continuity of heat flux and temperature are given by the following couple of expressions.

At the top of layer j :

$$\hat{T}_{j1}\left(\omega,\boldsymbol{x}\right)=\frac{-\mathrm{i}\pi P}{L_y\,\lambda_j}\sum_{n=1}^{N}\mathrm{J}_0\left(k_n\,\overline{r}_s\right)\frac{k_n}{v_{nj}}A^t_{nj}e^{-\mathrm{i}v_{nj}\left|y-\sum_{l=1}^{j-1}h_l\right|}\,. \tag{5.6}$$

At the bottom of layer j :

$$\hat{T}_{j2}\left(\omega,\boldsymbol{x}\right)=\frac{-\mathrm{i}\pi P}{L_y\,\lambda_j}\sum_{n=1}^{N}\mathrm{J}_0\left(k_n\,\overline{r}_s\right)\frac{k_n}{v_{nj}}A^b_{nj}e^{-\mathrm{i}v_{nj}\left|y-\sum_{l=1}^{j}h_l\right|}\,. \tag{5.7}$$

In these expressions $j=1,...,m$, $v_{nj}=\sqrt{-\mathrm{i}\omega/K_j-k_n^2}$ with $\mathrm{Im}\left(v_{nj}\right)\leq 0$ and h_l is the thickness of layer *l*. A^t_{nj} and A^b_{nj} are unknown coefficients that depend on the boundary conditions imposed at the top and bottom interfaces of each layer *j*.

Between the semi-infinite medium M_0 and layer M_1 (interface 1), and between layer M_m and medium M_{m+1} (interface *m*+1), the generated surface terms are given by the following pair of expressions.

At the bottom of medium M_0 (interface 1):

$$\hat{T}_{02}\left(\omega,\boldsymbol{x}\right)=\frac{-\mathrm{i}\pi P}{L_y\,\lambda_0}\sum_{n=1}^{N}\mathrm{J}_0\left(k_n\,\overline{r}_s\right)\frac{k_n}{v_{n0}}A^b_{n0}\,e^{-\mathrm{i}v_{n0}\left|y\right|}\,. \tag{5.8}$$

At the top of medium M_{m+1} (interface m+1):

$$\hat{T}_{(m+1)1}\left(\omega,\boldsymbol{x}\right)=\frac{-\mathrm{i}\pi P}{L_y\,\lambda_{(m+1)}}\sum_{n=1}^{N}\mathrm{J}_0\left(k_n\,\overline{r}_s\right)\frac{k_n}{v_{n(m+1)}}A^t_{n(m+1)}\,e^{-\mathrm{i}v_{n(m+1)}\left|y-\sum_{l=1}^{m}h_l\right|}\,. \tag{5.9}$$

In these equations $\nu_{n0} = \sqrt{-\mathrm{i}\omega/K_0 - k_n^{\,2}}$ and $\nu_{n(m+1)} = \sqrt{-\mathrm{i}\omega/K_{(m+1)} - k_n^{\,2}}$, with $\operatorname{Im}(\nu) \leq 0$ and A_{n0}^b and $A_{n(m+1)}^t$ are unknown amplitudes.

By imposing continuity of temperatures and heat fluxes between the different layers, a system of 2×(*m*+1) equations is derived:

$$\begin{bmatrix} -1 & -1 & e^{-\mathrm{i}\nu_{n1}h_1} & \dots & 0 & 0 & 0 \\ \dfrac{1}{\lambda_0\nu_{n0}} & -\dfrac{1}{\lambda_1\nu_{n1}} & -\dfrac{e^{-\mathrm{i}\nu_{n1}h_1}}{\lambda_1\nu_{n1}} & \dots & 0 & 0 & 0 \\ 0 & e^{-\mathrm{i}\nu_{n1}h_1} & -1 & \dots & 0 & 0 & 0 \\ 0 & \dfrac{e^{-\mathrm{i}\nu_{n1}h_1}}{\lambda_1\nu_{n1}} & \dfrac{1}{\lambda_1\nu_{n1}} & \dots & 0 & 0 & 0 \\ \dots & \dots & \dots & \dots & \dots & \dots & \dots \\ 0 & 0 & 0 & \dots & -1 & e^{-\mathrm{i}\nu_{nm}h_m} & 0 \\ 0 & 0 & 0 & \dots & -\dfrac{1}{\lambda_m\nu_{nm}} & -\dfrac{e^{-\mathrm{i}\nu_{nm}h_m}}{\lambda_m\nu_{nm}} & 0 \\ 0 & 0 & 0 & \dots & e^{-\mathrm{i}\nu_{nm}h_m} & -1 & -1 \\ 0 & 0 & 0 & \dots & \dfrac{e^{-\mathrm{i}\nu_{nm}h_m}}{\lambda_m\nu_{nm}} & \dfrac{1}{\lambda_m\nu_{nm}} & \dfrac{1}{\lambda_{(m+1)}\nu_{n(m+1)}} \end{bmatrix} \begin{bmatrix} A_{n0}^b \\ A_{n1}^t \\ A_{n1}^b \\ \dots \\ A_{nm}^t \\ A_{nm}^b \\ A_{n(m+1)}^t \end{bmatrix} = \begin{bmatrix} -e^{-\mathrm{i}\nu_{n1}y_s} \\ \dfrac{e^{-\mathrm{i}\nu_{n1}y_s}}{\lambda_1\nu_{n1}} \\ -e^{-\mathrm{i}\nu_{n1}|h_1-y_s|} \\ -\dfrac{e^{-\mathrm{i}\nu_{n1}|h_1-y_s|}}{\lambda_1\nu_{n1}} \\ \dots \\ 0 \\ 0 \\ 0 \\ 0 \end{bmatrix} \qquad (5.10)$$

The solution to this system provides the amplitude of the surface terms in each interface. The temperature field generated by the surface terms in each layer of the system is given by the equations below.

In the upper semi-infinite medium M_0 *(* $y<0$ *):*

$$\hat{T}(\omega,\boldsymbol{x}) = \frac{-\mathrm{i}\pi P}{L_y\,\lambda_0}\sum_{n=1}^{N}\mathrm{J}_0\left(k_n\,\overline{r}_s\right)\frac{k_n}{\nu_{n0}}A_{n0}^b\,e^{-\mathrm{i}\nu_{n0}|y|}. \qquad (5.11)$$

In any layer j other than M_0 *or medium* M_{m+1} *(* $0<y<\sum_{l=1}^{j}h_l$ *):*

$$\hat{T}(\omega,\boldsymbol{x}) = \frac{-\mathrm{i}\pi P}{L_y\,\lambda_j}\sum_{n=1}^{N}\mathrm{J}_0\left(k_n\,\overline{r}_s\right)\frac{k_n}{\nu_{nj}}\left(A_{nj}^t\,e^{-\mathrm{i}\nu_{nj}\left|y-\sum_{l=1}^{j-1}h_l\right|} + A_{nj}^b\,e^{-\mathrm{i}\nu_{nj}\left|y-\sum_{l=1}^{j}h_l\right|}\right). \qquad (5.12)$$

In the lower semi-infinite medium M_{m+1} *(* $y > \sum_{l=1}^{j=m} h_l$ *):*

$$\hat{T}(\omega,\boldsymbol{x}) = \frac{-\mathrm{i}\pi P}{L_y \lambda_{(m+1)}} \sum_{n=1}^{N} \mathrm{J}_0\left(k_n \overline{r}_s\right) \frac{k_n}{\nu_{n(m+1)}} A^t_{n(m+1)} e^{-\mathrm{i}\nu_{n(m+1)}\left|y-\sum_{l=1}^{m} h_l\right|} . \tag{5.13}$$

In these expressions $\nu_{nj} = \sqrt{-\mathrm{i}\omega/K_j - k_n^2}$ with $\mathrm{Im}(\nu_{nj}) \le 0$ and $K_j = \lambda_j/(\rho_j c_j)$, A^t_{nj} and A^b_{nj} are the amplitudes at the top and bottom of each layer j, and h_l is the thickness of layer l.

In the layer containing the heat source, total heat field is given by adding the direct incident heat field given by Equation (5.3) to the heat field generated by these surface terms.

5.2.3 3D TBEM formulation for multilayered media containing thin defects

The heat field created by the presence of a defect located within one of the layers of the system can be modelled using a BEM based technique, meaning that only the discretization of the inclusion is required. However, when thin defects are present, the conventional direct BEM can degenerate and become inaccurate. This is solved by using the normal derivative integral equations formulation (TBEM) which is derived by applying the gradient operator to the boundary integral equation, assuming the existence of dipole heat sources.

For a 3D point heat source placed at $\boldsymbol{x}_s$, when the boundary *S* is loaded with dipoles, the integral equation is expressed by:

$$a\hat{T}(\omega,\boldsymbol{x}_0) = -\int_S \overline{H}(\omega,\boldsymbol{x},\boldsymbol{x}_0,\mathbf{n}_{n1},\mathbf{n}_{n2})\hat{T}(\omega,\boldsymbol{x})ds + \overline{T}_{inc}(\omega,\boldsymbol{x}_0,\boldsymbol{x}_s,\mathbf{n}_{n2}), \tag{5.14}$$

in which $\mathbf{n}_{n1}$ represents the unit outward normal to the boundary *S* at point $\boldsymbol{x}$, $\mathbf{n}_{n2}$ represents the unit outward normal to boundary *S* at the collocation points $\boldsymbol{x}_0 = (x_0, y_0, z_0)$ and *a* is null for planar piecewise boundary elements.

The solution to the problem is obtained by solving the normal derivative integral equation, which requires the discretization of the surface of the defect *S* into N_B planar boundary elements with one nodal point at the centre of each element.

If the source is located somewhere in the same layer as the defect, then the incident heat field in (5.14) is given by the sum of the field generated by the source (expressed as $\overline{T}_{inc\_f}$), which is equal to that obtained for an unbounded medium, with the disturbances that occur at each interface between layers ($\overline{T}_{inc\_l}$). The heat field incident in $\boldsymbol{x}$ is then given by the following expression:

$$\overline{T}_{inc}\left(\omega,\boldsymbol{x},\boldsymbol{x}_s,\mathbf{n}_{n2}\right)=\overline{T}_{inc\_f}\left(\omega,\boldsymbol{x},\boldsymbol{x}_s,\mathbf{n}_{n2}\right)+\overline{T}_{inc\_l}\left(\omega,\boldsymbol{x},\boldsymbol{x}_s,\mathbf{n}_{n2}\right), \tag{5.15}$$

where

$$\overline{T}_{inc\_f}\left(\omega,\boldsymbol{x},\boldsymbol{x}_s,\mathbf{n}_{n2}\right)=\frac{Pe^{-\mathrm{i}k_j r_s}\left(-\mathrm{i}k_j r_s-1\right)}{2\lambda_j r_s^{\,2}}\left(\frac{\partial r_s}{\partial x}\frac{\partial x}{\partial \mathbf{n}_{n2}}+\frac{\partial r_s}{\partial y}\frac{\partial y}{\partial \mathbf{n}_{n2}}+\frac{\partial r_s}{\partial z}\frac{\partial z}{\partial \mathbf{n}_{n2}}\right), \tag{5.16}$$

$$\begin{aligned}\overline{T}_{inc\_l}\left(\omega,\boldsymbol{x},\boldsymbol{x}_s,\mathbf{n}_{n2}\right)=\frac{-\mathrm{i}\pi P}{L_y\lambda_j}\sum_{n=1}^{N}\Bigg[&\left(-k_n\right)\mathrm{J}_1\left(k_n\overline{r}_s\right)\left(\frac{\partial \overline{r}_s}{\partial x}\frac{\partial x}{\partial \mathbf{n}_{n2}}+\frac{\partial \overline{r}_s}{\partial z}\frac{\partial z}{\partial \mathbf{n}_{n2}}\right)\frac{k_n}{\nu_{nj}}A_{nj}^{1}\\&+\mathrm{J}_0\left(k_n\overline{r}_s\right)\frac{k_n}{\nu_{nj}}\left(-\mathrm{i}\nu_{nj}\right)A_{nj}^{2}\frac{\partial y}{\partial \mathbf{n}_{n2}}\Bigg],\end{aligned} \tag{5.17}$$

in which $A_{nj}^{1}=A_{nj}^{t}\,e^{-\mathrm{i}\nu_{nj}\left|y-\sum_{l=1}^{j-1}h_l\right|}+A_{nj}^{b}\,e^{-\mathrm{i}\nu_{nj}\left|y-\sum_{l=1}^{j}h_l\right|}$ and $A_{nj}^{2}=A_{nj}^{t}\,e^{-\mathrm{i}\nu_{nj}\left|y-\sum_{l=1}^{j-1}h_l\right|}-A_{nj}^{b}\,e^{-\mathrm{i}\nu_{nj}\left|y-\sum_{l=1}^{j}h_l\right|}$.

If the source is not located in the layer containing the defect, then the incident heat field in (5.14) is only given by the $\overline{T}_{inc\_l}$.

The required Green's functions are also written as the sum of source and surface terms, which are the terms relative to the field generated by the presence of the interfaces. For temperature these are expressed as:

$$G\left(\omega,\boldsymbol{x},\boldsymbol{x}_0\right)=G_f\left(\omega,\boldsymbol{x},\boldsymbol{x}_0\right)+G_l\left(\omega,\boldsymbol{x},\boldsymbol{x}_0\right), \tag{5.18}$$

in which $G_f\left(\omega,\boldsymbol{x},\boldsymbol{x}_0\right)=\dfrac{e^{-\mathrm{i}k_j r_0}}{4\pi\lambda_j r_0}$ and $G_l\left(\omega,\boldsymbol{x},\boldsymbol{x}_0\right)=\dfrac{-\mathrm{i}P}{2L_y\lambda_j}\sum_{n=1}^{N}\mathrm{J}_0\left(k_n\overline{r}_0\right)\dfrac{k_n}{\nu_{nj}}A_{nj}^{1}$,

where $k_j=\sqrt{-\mathrm{i}\omega/K_j}$, $\overline{r}_0=\sqrt{\left(x-x_0\right)^2+\left(z-z_0\right)^2}$ and $r_0=\sqrt{\left(x-x_0\right)^2+(y-y_0)^2+\left(z-z_0\right)^2}$.

The Green's functions for heat fluxes are derived from the previous and given by:

$$H\left(\omega,\boldsymbol{x},\boldsymbol{x}_0,\mathbf{n}_{n1}\right)=H_f\left(\omega,\boldsymbol{x},\boldsymbol{x}_0,\mathbf{n}_{n1}\right)+H_l\left(\omega,\boldsymbol{x},\boldsymbol{x}_0,\mathbf{n}_{n1}\right), \tag{5.19}$$

in which $H_f\left(\omega,\boldsymbol{x},\boldsymbol{x}_0,\mathbf{n}_{n1}\right)=\dfrac{e^{-\mathrm{i}k_j r_0}\left(-\mathrm{i}k_j r_0-1\right)}{4\pi\lambda_j r_0^{\;2}}\dfrac{\partial r_0}{\partial\mathbf{n}_{n1}}$ and

$$H_l\left(\omega,\boldsymbol{x},\boldsymbol{x}_0,\mathbf{n}_{n1}\right)=\frac{-\mathrm{i}P}{2L_y\lambda_j}\sum_{n=1}^{N}\left[-k_n\mathrm{J}_1\left(k_n\bar{r}_0\right)\left(\frac{\partial\bar{r}_0}{\partial x}\frac{\partial x}{\partial\mathbf{n}_{n1}}+\frac{\partial\bar{r}_0}{\partial z}\frac{\partial z}{\partial\mathbf{n}_{n1}}\right)\frac{k_n}{\nu_{nj}}A_{nj}^1\right.$$
$$\left.+\mathrm{J}_0\left(k_n\bar{r}_0\right)\frac{k_n}{\nu_{nj}}\left(-\mathrm{i}\nu_{nj}\right)A_{nj}^2\frac{\partial y}{\partial\mathbf{n}_{n1}}\right].$$

The required Green's fundamental solutions $\bar{H}$ are obtained by applying the gradient operator to $H\left(\omega,\boldsymbol{x},\boldsymbol{x}_0,\mathbf{n}_{n1}\right)$ and similarly are given by:

$$\bar{H}\left(\omega,\boldsymbol{x},\boldsymbol{x}_0,\mathbf{n}_{n1},\mathbf{n}_{n2}\right)=\bar{H}_f\left(\omega,\boldsymbol{x},\boldsymbol{x}_0,\mathbf{n}_{n1},\mathbf{n}_{n2}\right)+\bar{H}_l\left(\omega,\boldsymbol{x},\boldsymbol{x}_0,\mathbf{n}_{n1},\mathbf{n}_{n2}\right). \tag{5.20}$$

The part of this derivation relative to the heat field in an unbounded medium is given by:

$$\bar{H}_f\left(\omega,\boldsymbol{x},\boldsymbol{x}_0,\mathbf{n}_{n1},\mathbf{n}_{n2}\right)=\frac{\partial H_f}{\partial x}\frac{\partial x}{\partial\mathbf{n}_{n2}}+\frac{\partial H_f}{\partial y}\frac{\partial y}{\partial\mathbf{n}_{n2}}+\frac{\partial H_f}{\partial z}\frac{\partial z}{\partial\mathbf{n}_{n2}}, \tag{5.21}$$

with $\dfrac{\partial H_f}{\partial x}(\omega,\boldsymbol{x},\boldsymbol{x}_0,\mathbf{n}_{n1})=\dfrac{1}{4\pi}\left\{A\left[\left(\dfrac{\partial r_0}{\partial x}\right)^2\dfrac{\partial x}{\partial\mathbf{n}_{n1}}+\dfrac{\partial r_0}{\partial x}\dfrac{\partial r_0}{\partial y}\dfrac{\partial y}{\partial\mathbf{n}_{n1}}+\dfrac{\partial r_0}{\partial x}\dfrac{\partial r_0}{\partial z}\dfrac{\partial z}{\partial\mathbf{n}_{n1}}\right]+B\left[\dfrac{\partial x}{\partial\mathbf{n}_{n1}}\right]\right\}$,

$$\frac{\partial H_f}{\partial y}(\omega,\boldsymbol{x},\boldsymbol{x}_0,\mathbf{n}_{n1})=\frac{1}{4\pi}\left\{A\left[\frac{\partial r_0}{\partial x}\frac{\partial r_0}{\partial y}\frac{\partial x}{\partial\mathbf{n}_{n1}}+\left(\frac{\partial r_0}{\partial y}\right)^2\frac{\partial y}{\partial\mathbf{n}_{n1}}+\frac{\partial r_0}{\partial y}\frac{\partial r_0}{\partial z}\frac{\partial z}{\partial\mathbf{n}_{n1}}\right]+B\left[\frac{\partial y}{\partial\mathbf{n}_{n1}}\right]\right\},$$

$$\frac{\partial H_f}{\partial z}(\omega,\boldsymbol{x},\boldsymbol{x}_0,\mathbf{n}_{n1})=\frac{1}{4\pi}\left\{A\left[\frac{\partial r_0}{\partial x}\frac{\partial r_0}{\partial z}\frac{\partial x}{\partial\mathbf{n}_{n1}}+\frac{\partial r_0}{\partial y}\frac{\partial r_0}{\partial z}\frac{\partial y}{\partial\mathbf{n}_{n1}}+\left(\frac{\partial r_0}{\partial z}\right)^2\frac{\partial z}{\partial\mathbf{n}_{n1}}\right]+B\left[\frac{\partial z}{\partial\mathbf{n}_{n1}}\right]\right\},$$

in which $A=-\dfrac{k_j^{\;2}e^{-\mathrm{i}k_j r_0}}{r_0}+\dfrac{3\mathrm{i}k_j e^{-\mathrm{i}k_j r_0}}{r_0^{\;2}}+\dfrac{3e^{-\mathrm{i}k_j r_0}}{r_0^{\;3}}$ and $B=-\dfrac{\mathrm{i}k_j e^{-\mathrm{i}k_j r_0}}{r_0^{\;2}}-\dfrac{e^{-\mathrm{i}k_j r_0}}{r_0^{\;3}}$.

The part of $\bar{H}$ relative to the heat field generated by the interfaces can be written as:

$$\overline{H}_l\left(\omega,\boldsymbol{x},\boldsymbol{x}_0,\mathbf{n}_{n1},\mathbf{n}_{n2}\right)=\frac{\partial H_l}{\partial x}\frac{\partial x}{\partial \mathbf{n}_{n2}}+\frac{\partial H_l}{\partial y}\frac{\partial y}{\partial \mathbf{n}_{n2}}+\frac{\partial H_l}{\partial z}\frac{\partial z}{\partial \mathbf{n}_{n2}}\,, \tag{5.22}$$

with

$$\begin{aligned}\frac{\partial H_l}{\partial x}(\omega,\boldsymbol{x},\boldsymbol{x}_0,\mathbf{n}_{n1})=\frac{-\mathrm{i}P}{2L_y}\sum_{n=1}^{N}\Bigg[&-k_n\left(\frac{\mathrm{J}_1\left(k_n\overline{r}_0\right)}{\overline{r}_0}-k_n\mathrm{J}_2\left(k_n\overline{r}_0\right)\right)\left(\frac{\partial\overline{r}_0}{\partial x}\frac{\partial x}{\partial \mathbf{n}_{n1}}+\frac{\partial\overline{r}_0}{\partial z}\frac{\partial z}{\partial \mathbf{n}_{n1}}\right)\frac{k_n}{\nu_{nj}}A_{nj}^1\frac{\partial\overline{r}_0}{\partial x}\\&-k_n\mathrm{J}_1\left(k_n\overline{r}_0\right)\left(\frac{1-\left(\frac{\partial\overline{r}_0}{\partial x}\right)^2}{\overline{r}_0}\frac{\partial x}{\partial \mathbf{n}_{n1}}-\frac{\frac{\partial\overline{r}_0}{\partial x}\frac{\partial\overline{r}_0}{\partial z}}{\overline{r}_0}\frac{\partial z}{\partial \mathbf{n}_{n1}}\right)\frac{k_n}{\nu_{nj}}A_{nj}^1-k_n\mathrm{J}_1\left(k_n\overline{r}_0\right)\left(-\mathrm{i}k_n\right)A_{nj}^2\frac{\partial\overline{r}_0}{\partial x}\frac{\partial y}{\partial \mathbf{n}_{n1}}\Bigg],\end{aligned}$$

$$\begin{aligned}\frac{\partial H_l}{\partial y}(\omega,\boldsymbol{x},\boldsymbol{x}_0,\mathbf{n}_{n1})=\frac{-\mathrm{i}P}{2L_y}\sum_{n=1}^{N}\Bigg[&-k_n\,\mathrm{J}_1\left(k_n\overline{r}_0\right)\left(\frac{\partial\overline{r}_0}{\partial x}\frac{\partial x}{\partial \mathbf{n}_{n1}}+\frac{\partial\overline{r}_0}{\partial z}\frac{\partial z}{\partial \mathbf{n}_{n1}}\right)\left(-\mathrm{i}k_n\right)A_{nj}^2\\&+\mathrm{J}_0\left(k_n\overline{r}_0\right)k_n\left(-\nu_{nj}\right)A_{nj}^1\frac{\partial y}{\partial \mathbf{n}_{n1}}\Bigg],\end{aligned}$$

$$\begin{aligned}\frac{\partial H_l}{\partial z}(\omega,\boldsymbol{x},\boldsymbol{x}_0,\mathbf{n}_{n1})=\frac{-\mathrm{i}P}{2L_y}\sum_{n=1}^{N}\Bigg[&-k_n\left(\frac{\mathrm{J}_1\left(k_n\overline{r}_0\right)}{\overline{r}_0}-k_n\mathrm{J}_2\left(k_n\overline{r}_0\right)\right)\left(\frac{\partial\overline{r}_0}{\partial x}\frac{\partial x}{\partial \mathbf{n}_{n1}}+\frac{\partial\overline{r}_0}{\partial z}\frac{\partial z}{\partial \mathbf{n}_{n1}}\right)\frac{k_n}{\nu_{nj}}A_{nj}^1\frac{\partial\overline{r}_0}{\partial z}\\&-k_n\mathrm{J}_1\left(k_n\overline{r}_0\right)\left(\frac{-\frac{\partial\overline{r}_0}{\partial x}\frac{\partial\overline{r}_0}{\partial z}}{\overline{r}_0}\frac{\partial x}{\partial \mathbf{n}_{n1}}+\frac{1-\left(\frac{\partial\overline{r}_0}{\partial z}\right)^2}{\overline{r}_0}\frac{\partial z}{\partial \mathbf{n}_{n1}}\right)\frac{k_n}{\nu_{nj}}A_{nj}^1-k_n\mathrm{J}_1\left(k_n\overline{r}_0\right)\left(-\mathrm{i}k_n\right)A_{nj}^2\frac{\partial\overline{r}_0}{\partial z}\frac{\partial y}{\partial \mathbf{n}_{n1}}\Bigg].\end{aligned}$$

The solution to the problem is obtained by solving the normal derivative integral equation in (5.14), after discretizing the defect surface *S* into N_B boundary surface elements.

This leads to a system of $N_B \times N_B$ equations that require the integration $\overline{H}^{kl}=\int_{B_l}\overline{H}\left(\omega,x_l,y_l,z_l,x_k,y_k,z_k,\mathbf{n}_{n1},\mathbf{n}_{n2}\right)\mathrm{d}B_l$, in which *l* is the element being integrated, *k* is the loaded element, and B_l is the surface of boundary element *l*. When the element to be integrated is not the loaded element, then the integrations are evaluated using a Gaussian quadrature scheme. For the loaded element, the integrands exhibit a singularity (hypersingular element). Such singularities may be solved analytically (as described thoroughly in section 2.3.3).

5.2.4 Verification of the solution

The verification of the model proposed in this study was performed against the previously presented 3D TBEM model for unbounded media (in Chapter 2). In order to enable the comparison between the methods, a mirror image source technique was used, which is explained next.

First, two systems were modelled using the previous 3D TBEM for unbounded media: a half-space with prescribed null normal heat fluxes along the surface and a half-space with imposed null temperature. Null heat fluxes along a flat surface are achieved by adding the heat field generated by the real source and the real inclusion to that which is produced by a virtual source and a virtual inclusion (which act as a mirror). Similarly, null temperature is accomplished by using a virtual source with negative amplitude in order to guarantee the required boundary conditions.

Then, using the proposed 3D TBEM multilayered model, heat diffusion was computed in a multilayered medium whose layers, other than medium M_0, have constant thermal properties equal to those of the semi-infinite medium simulated using the previously developed 3D TBEM model. At the top, null normal heat fluxes are achieved by imposing very low conductivity in M_0, while null temperatures are enforced by imposing extremely high conductivity in M_0.

The geometry of the system modelled for the verification of the solution is shown in Figure 5.3. To perform the verification of the solution, a medium with conductivity $\lambda = 1.4$ W/(m.°C), heat capacity $c = 880.0$ J/(kg.°C) and density $\rho = 2300.0$ kg/m^3 was considered. This system is subjected to a 3D point heat source placed at $\boldsymbol{x}_s = (0.03, 0.04, 0.03)$ m and the defect is a plane 0.05×0.05 m^2 null thickness inclusion located parallel to the xz plane at $y = 0.05$ m. Its boundary surface is discretized into 20×20 square boundary elements with a side length of 0.0025 m.

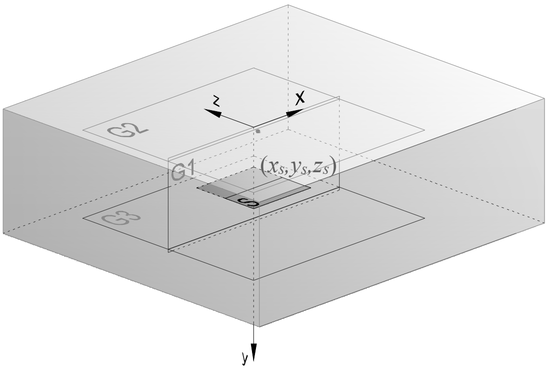

Figure 5.3: 3D view of the geometry of the system modelled for the verification of the solution.

The frequency domain temperature response was computed over three grids of receivers: one placed parallel to plane *xy* at $z = 0.0$ m (G1) and the other two placed parallel to the defect (G2 at $y = 0.0025$ m and G3 at $y = 0.075$ m). The receivers are spaced at equal intervals of 0.0020 m in the *x* and *z* directions and 0.0013 m in the *y* axis direction. A more detailed representation is given in Figure 5.4, along with the placement of specific receivers: A at (−0.015, 0.0025, −0.015) m, B at (0.015, 0.0025, 0.015) m, C at (−0.035, 0.075, −0.035) m and D at (−0.015, 0.0625, 0.0) m.

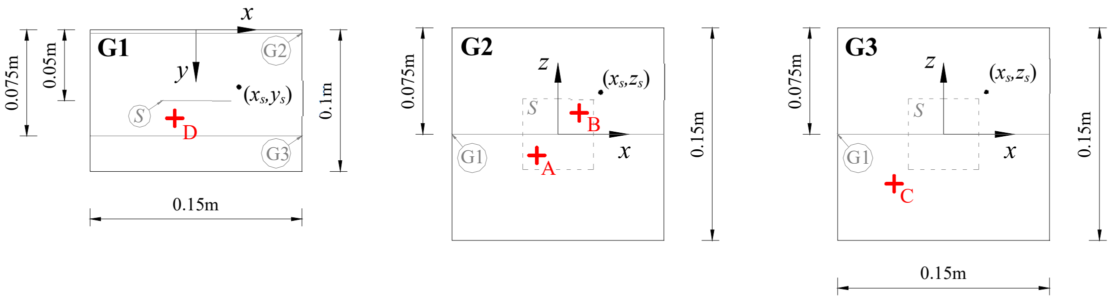

a) b) c)

Figure 5.4: 2D view of the geometry of the system modelled for the verification of the solution: a) *xy* plane and position of rec. D in G1 at $z = 0$ m; b) *xz* plane and position of recs. A and B in G2 at $y = 0.025$ m; c) *xz* plane and position of rec. C in G3 at $y = 0.075$ m.

Results were computed in a frequency range of 0.0 Hz to 6.35×10^{-5} Hz. The real and imaginary part of the response at receivers A, B, C and D are illustrated in Figure 5.5, which corresponds to the case of null heat flux, and Figure 5.6, corresponding to the null temperature imposition case.

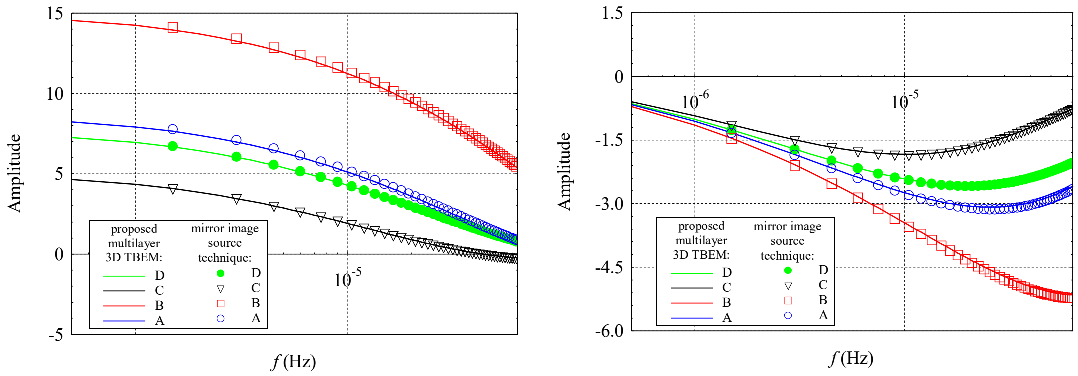

a) b)

Figure 5.5: Responses of the proposed multilayered 3D TBEM model against the previous 3D TBEM model for the case of null heat flux at $y = 0$, recorded at receivers A, B, C and D: a) real part; b) imaginary part.

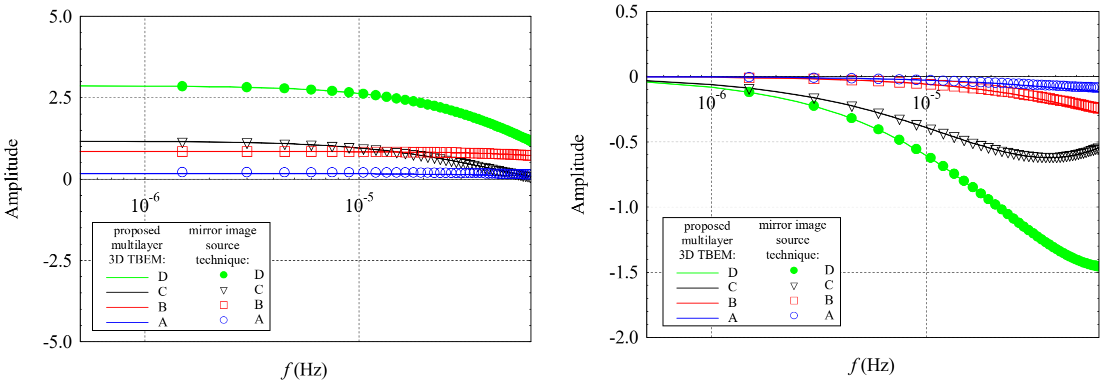

a) b)

Figure 5.6: Responses of the proposed multilayered 3D TBEM model against the previous 3D TBEM model for the case of null temperature at $y = 0$, recorded at receivers A, B, C and D: a) real part; b) imaginary part.

The results show that, both for the cases of imposed null heat flux and null temperature, the frequency domain temperature responses appear to be in agreement.

5.2.5 Numerical application results

In order to illustrate the usefulness of the proposed method for computing heat diffusion in a defective multilayered system, a number of numerical applications were performed to the system of two layers bounded by two semi-infinite media subjected to a 3D point heat source shown in Figure 5.7.

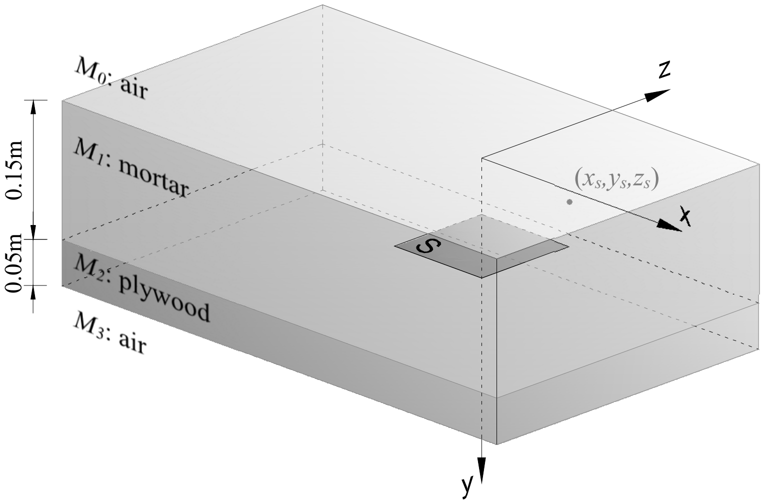

Figure 5.7: 3D view of the defective two-layer system subjected to 3D heat source.

The defect is a 0.05×0.05 m^2 flat null thickness inclusion located in the layer of mortar and is placed parallel to the flat interfaces at a specific depth *d*. The vertical placement of the heat source y_s and the depth *d* at which the defect is located within the mortar layer can vary.

The top and bottom semi-infinite media have properties similar to those of air ($\lambda = 0.026$ W/(m.ºC), $c = 1000.0$ J/(kg.ºC) and $\rho = 1.293$ kg/m^3) [18]. The upper layer is 0.15 m thick mortar and the lower layer is a wood-based material (marine plywood) that is 0.05 m thick. The materials are considered to have the thermal properties given in Table 5.1. These correspond to the thermal properties found for the materials used in the test specimens of the experimental part of this study which is presented in the next section of the present chapter (section 5.2).

Table 5.1: Material thermal properties considered in the model.

Material	Conductivity λ (W/(m.ºC))	Specific heat c (J/(kg.ºC))	Density ρ (kg/m^3)
Mortar	0.484	1010	1307
Marine plywood	0.114	1210	484

Results are recorded over three grids of receivers: one is perpendicular to the interfaces and the defect, and is located at $z = 0.0$ m (G1) while the two others are placed parallel to the defect and the interfaces (G2 at $y = 0.0$ m and G3 at $y = 0.075$ m). The receivers are spaced at equal intervals of 0.002 m in the x and z directions and 0.004 m in the y axis direction. A representation of the grids is given in Figure 5.8.

Note that, in this simulation model, G2 corresponds to the surface of a test specimen being inspected in IRT tests. Therefore, results computed numerically at this grid of receivers attempt to simulate a response obtained experimentally.

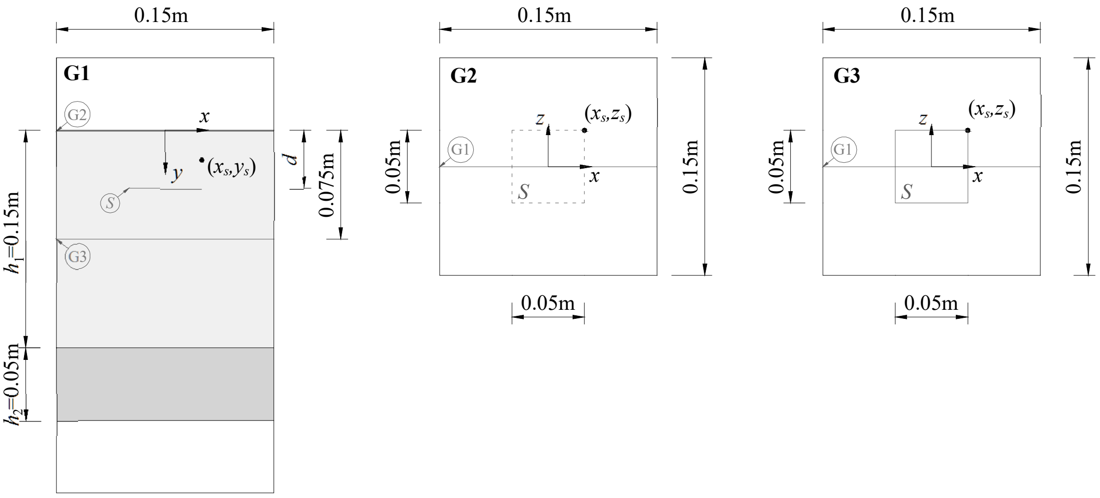

a) b) c)

Figure 5.8: 2D view of the system modelled: a) xy plane showing the grid of receivers G1 at $z = 0$ m; b) xz plane and G2 at $y = 0.005$ m; c) xz plane and G3 at $y = 0.075$ m.

Time domain temperature results

Time domain results were obtained by applying a numerical inverse fast Fourier transform to the frequency domain response. This procedure is given in more detail in section 2.3.5 in Chapter 2. In order to avoid aliasing phenomena, a dumping factor of $\eta = 0.7\Delta\omega$ was used, in which $\Delta\omega$ is the frequency step and $\Delta\omega = 2\pi\Delta f$. The results presented next are for computations performed assuming that the defect is located at $d = 0.04$ m and that the 3D point heat source is placed at $\mathbf{x}_s = (0.025, 0.02, 0.025)$ m, which is not aligned with the centre of the defect. The surface of the defect is discretized into 400 square boundary elements which are 0.0025×0.0025 m^2. The system is considered to be initially at 0 °C. The heat source starts emitting energy at $t = 28$ h and continues until $t = 167$ h, following a rectangular heating function.

Calculations were performed in a frequency range of 0.0 Hz to 1.024×10^{-3} Hz, with an increment of $\Delta f = 0.5\times10^{-6}$ Hz, corresponding to a total time window of 555.56 h. This frequency range was selected in such a way as to ensure a negligible contribution to the responses from the frequencies above a certain limit.

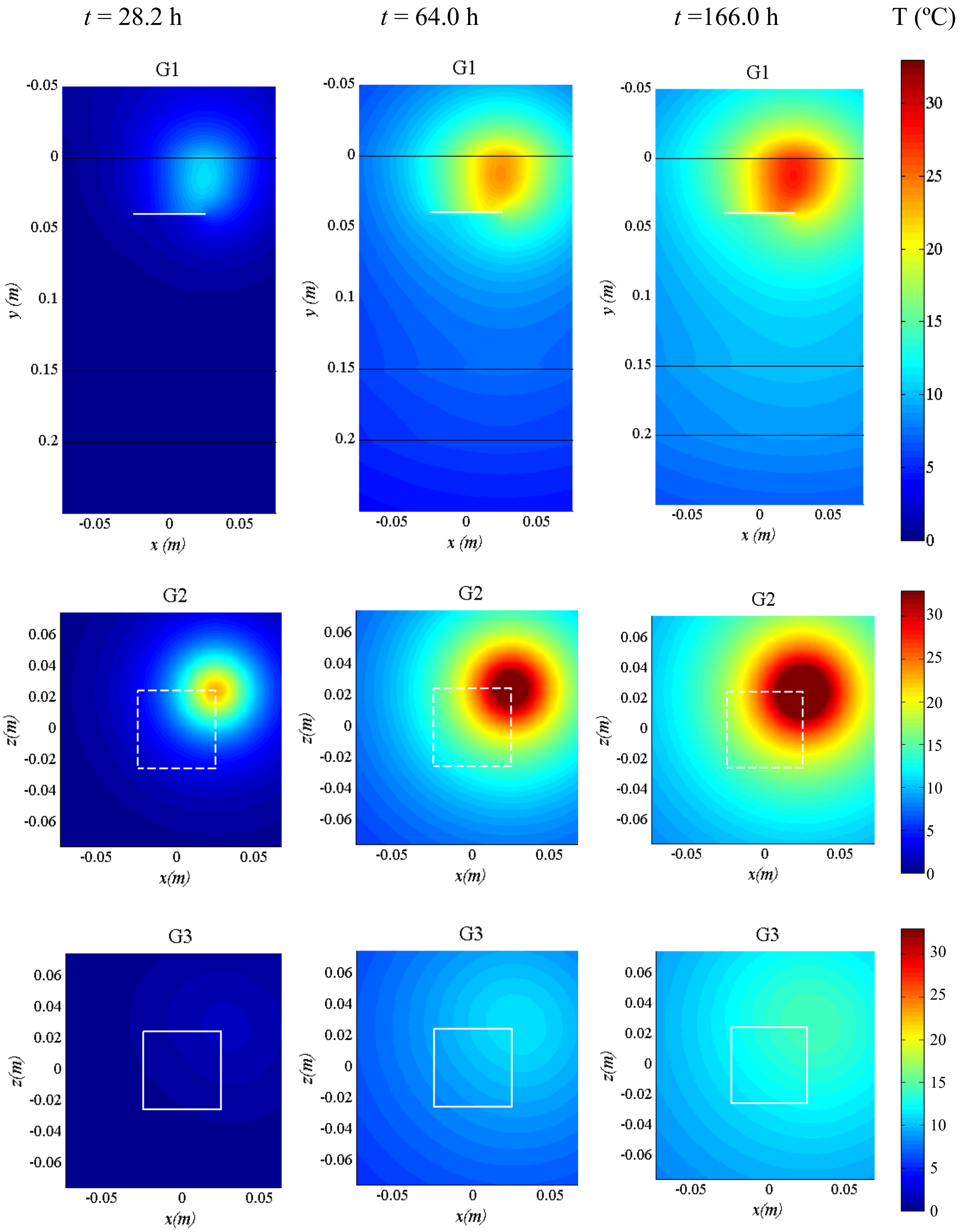

Figure 5.9: Snapshots of the temperature pattern response in the time domain, in °C, recorded over the grids of receivers G1, G2 and G3, taken at several instants.

Snapshots of the heat field taken at several instants are shown in Figure 5.9. The images on the left correspond to the results recorded at the instant immediately after the heating begins and on the right, is the temperature field relative to the moment just before the heat source is turned off. In the centre of the image are results computed sometime during the heating stage.

The results in Figure 5.9 illustrate the effects on the heat diffusion pattern of both the presence of the defect and the interfaces between layers. The results recorded for G1 clearly show the disturbance caused by the defect in the heat field. In particular, it is visible that heat flow is not allowed to propagate directly through the defect, resulting in an accumulation of heat between the defect and the top surface (noticeable in G2). By contrast, the field registered behind the defect in G3 is weak. It can also be observed that isothermal lines near the defect are perpendicular to its surface, which was expected given that null heat fluxes were prescribed. Additionally, the heat field across the layer interfaces exhibits continuity of temperature. In G2 and G3 the effect of the heat source is domineering and, although the defect's presence influences the heat field, its geometry and placement cannot be determined.

<u>*Phase results*</u>

In order to simulate results obtained in active IRT studies that use a phase contrast approach to defect detection, simulations were performed for the system represented in Figure 5.3 and Figure 5.4, but now considering that the defect is placed at either $d = 0.01$ m, $d = 0.02$ m or $d = 0.04$ m, and that the 3D point heat source is located in medium M_0 at $\boldsymbol{x}_s = (0.025, -0.50, 0.025)$ m.

Figure 5.10 shows snapshots, taken at several frequencies, of the phase amplitude results obtained for the receivers in grid G2. Thermal wave phase was calculated directly in the frequency domain from the arctangent of the quotient between the imaginary part and the real part of the frequency domain temperature response. In the snapshots presented, the outline of the defect is given in order to allow an easier interpretation of the results.

These results show how phase amplitude oscillates between positive and negative responses along the frequency spectrum. Even though the defect creates a disturbance, its detectability is not reliable. In particular, in the case of $d = 0.04$ m, the defect is hardly noticeable. Furthermore, the phase results are strongly affected by the 3D nature and by the location of the point heat source.

Then, phase contrast results were obtained by computing both the results for the defective multilayered system using the 3D TBEM formulation presented in section 5.2.3, and for a medium with the same configuration and characteristics, but which does not contain any defects (sound media), which is solved analytically following the expressions given in section 5.2.2, and then by calculating the difference between defective and sound media responses. These results are given in Figure 5.11.

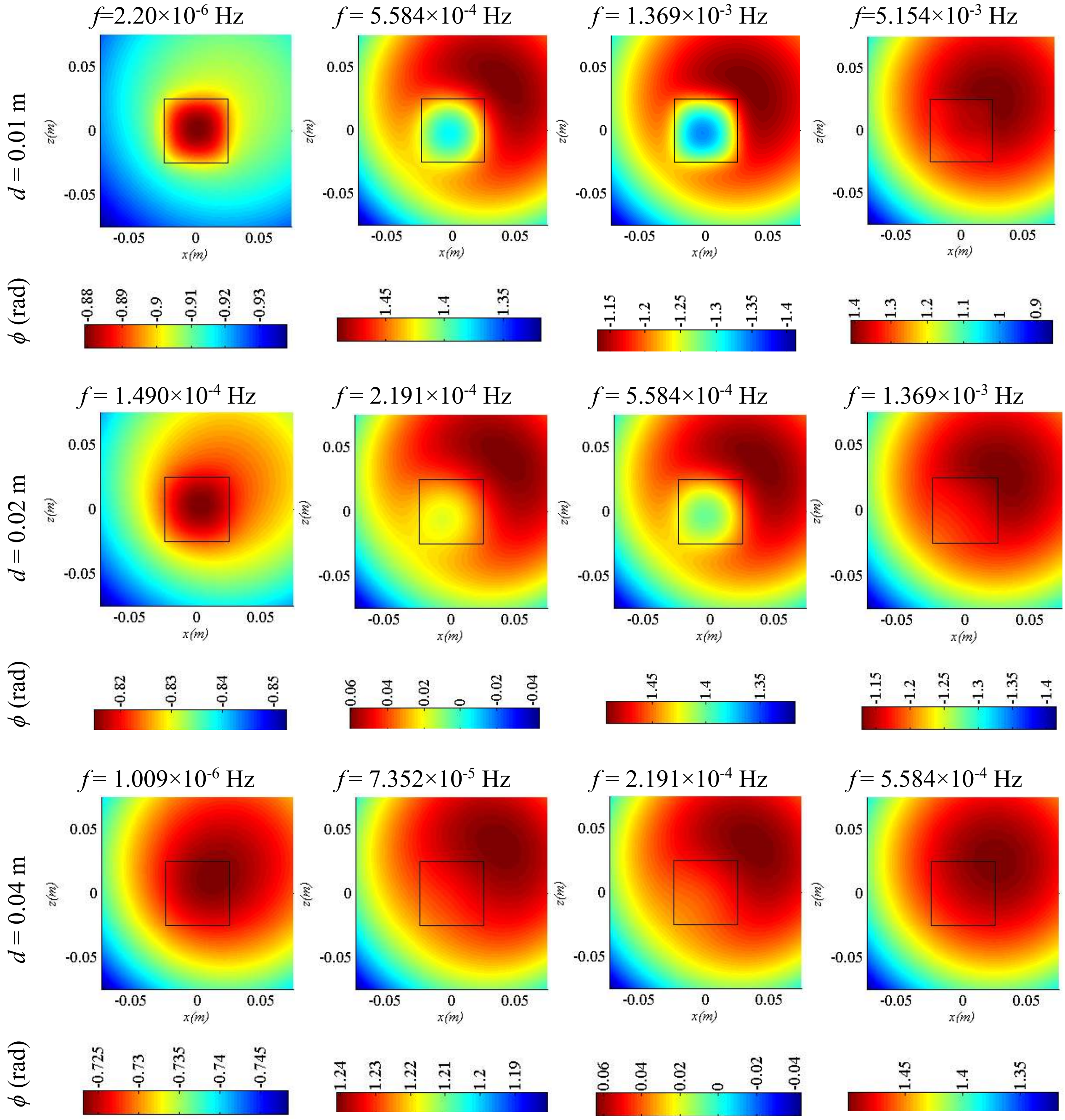

Figure 5.10: Snapshots of the phase amplitude results, in radians, recorded over the grid of receivers G2 for varying defect depth, taken at several frequencies.

Figure 5.11 shows phase contrast results for several different frequencies. In defect detection studies, the frequency for which a defect is most visible is referred to as the characteristic frequency of the defect (f_{ch}). Hence, for each defect depth, the selected frequencies correspond to the characteristic frequency registered for the centre of the defect, and to two frequencies taken before, and one after, the characteristics frequency.

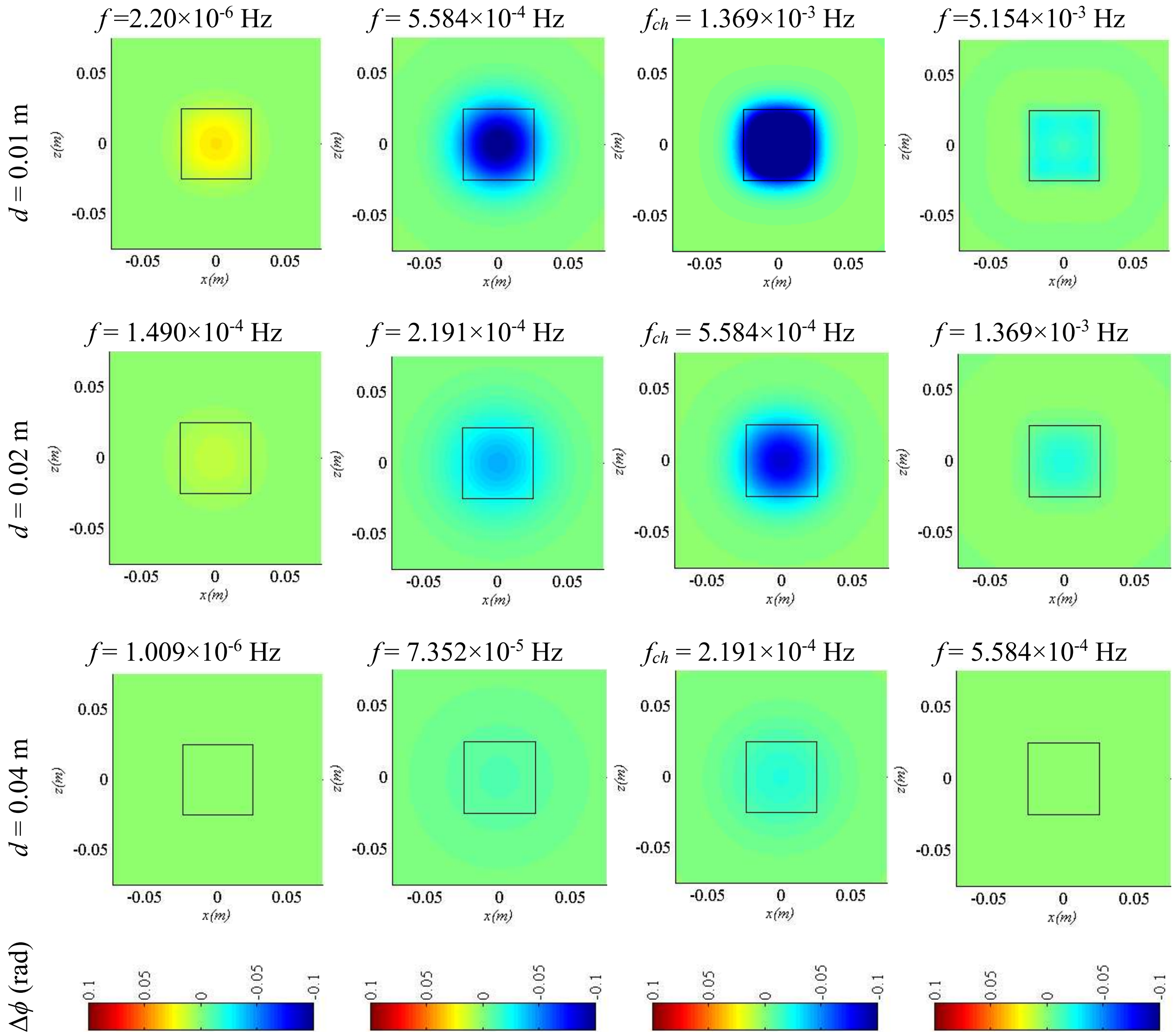

Figure 5.11: Snapshots of the phase contrast results, in radians, recorded over the grid of receivers G2 for varying defect depth, taken at several frequencies.

Compared to phase amplitude results, the phase contrast results shown are not affected by the non-uniform heating of the surface (provided by the 3D point source) and the defect geometry is easily defined. It should also be noted that, when the defect is closest to the surface, the geometry of the defect is easily detectable at the characteristic frequency. As the defect is further embedded in the media the amplitude of the phase contrast is weaker, not allowing the characterization of the defect geometry. In fact, for the deeper defect the signal is very subtle and the defect is hardly noticeable. This process for obtaining phase contrast results is not viable in real experiments since it is not possible to actually obtain the thermal response for the sound media. Therefore, similarly to the procedure used in IRT tests, phase contrast results in Figure 5.12 were obtained by selecting one receiver located at $\boldsymbol{x}_r = (x_r, y_r, z_r)$ in an area which is considered not to be influenced by the defect, to act as a reference for sound phase results.

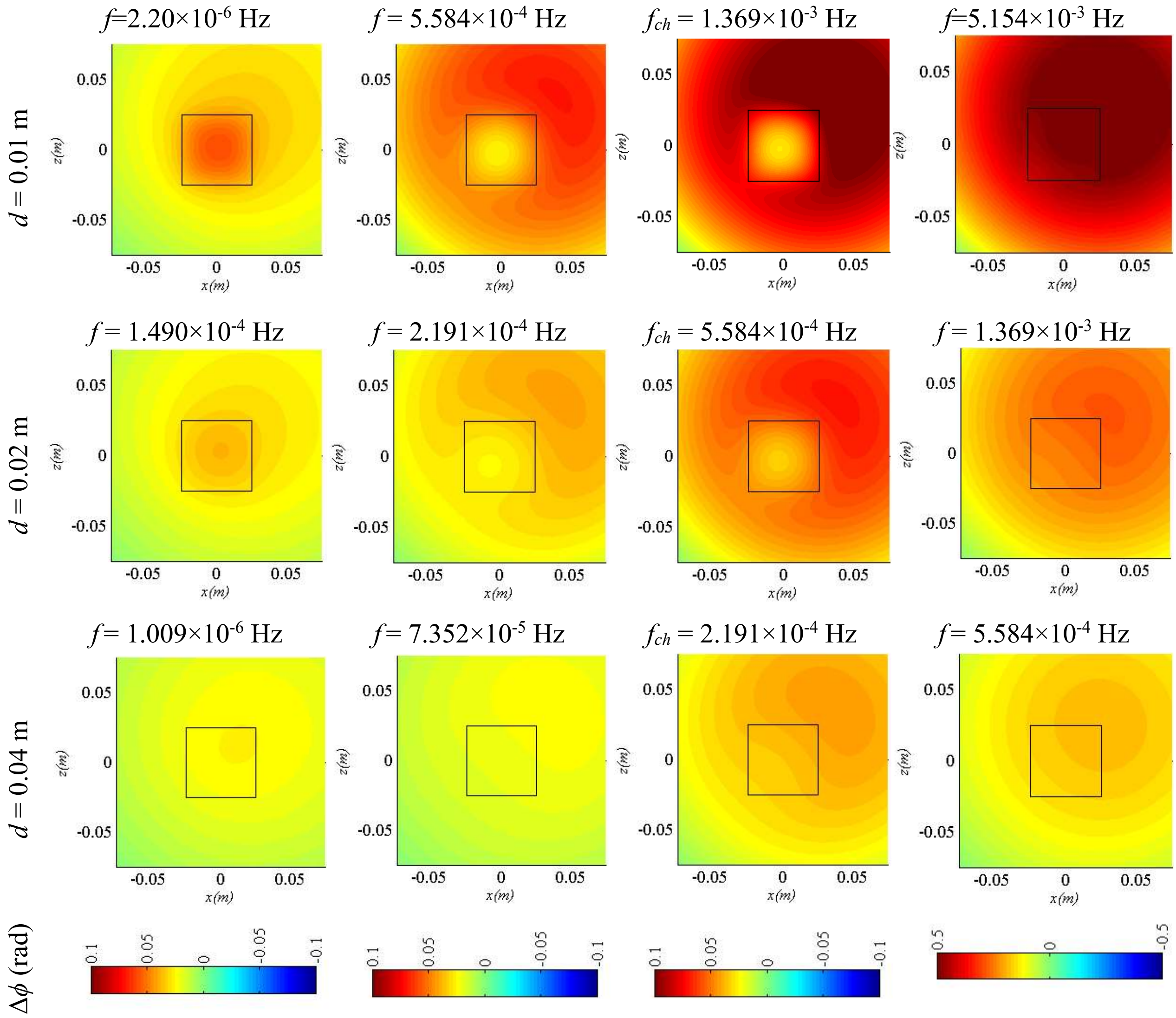
f=2.20×10^{-6} Hz; f = 5.584×10^{-4} Hz; f_{ch} = 1.369×10^{-3} Hz; f=5.154×10^{-3} Hz

f = 1.490×10^{-4} Hz; f = 2.191×10^{-4} Hz; f_{ch} = 5.584×10^{-4} Hz; f = 1.369×10^{-3} Hz

f = 1.009×10^{-6} Hz; f = 7.352×10^{-5} Hz; f_{ch} = 2.191×10^{-4} Hz; f = 5.584×10^{-4} Hz

Figure 5.12: Snapshots of the phase contrast results recorded over G2 for varying defect depth, in radians, calculated using a single pixel as reference for sound media, taken at several frequencies.

In the results presented, the receiver located at $\boldsymbol{x}_r$ = (−0.075, 0.0, −0.075) m was selected and phase contrast was obtained by computing the difference between phase in the defective layered media using the proposed 3D TBEM and phase obtained for $\boldsymbol{x}_r$ using the purely analytical model for sound multilayered media.

Phase contrast results shown in Figure 5.12 are now strongly affected by the 3D heat source and the detectability and characterization of the defect is now compromised. To overcome this, a correction technique can be applied, which takes into account the three-dimensionality of the point heat source. It is a simplified approach assuming that the correction of the phase follows the variation of the direct incident field given by Equation (5.3), and can be expressed by the following:

$$\phi_c(\omega,\boldsymbol{x}) = \arctan\left(\frac{\sin(\phi_r)\cos(k\,\Delta r)-\cos(\phi_r)\sin(k\,\Delta r)}{\cos(\phi_r)\cos(k\,\Delta r)+\sin(\phi_r)\sin(k\,\Delta r)}\right) \tag{5.23}$$

where ϕ_c is corrected phase, ϕ_r is phase at the reference sound receiver and $\Delta r = r_r - r_s$, in which $r_r = \sqrt{\left(x_r - x_s\right)^2 + (y_r - y_s)^2 + \left(z_r - z_s\right)^2}$.

Figure 5.13 shows the phase contrast results obtained using the correction technique proposed in Equation (5.23).

Results shown in Figure 5.13 are very similar to Figure 5.11, except for very low frequencies. This is due to the fact that, only at the higher frequencies does the phase of the reflected field (generated by the multilayer interfaces and the defect) come close to that of the direct incident heat field. In the case of d = 0.01 m or d = 0.02 m, the results at the lower frequencies, where phase contrast is positive, also show the position of the defect. However, in order to achieve these frequencies in real experiments, it would require the use of very long recording periods and the acquisition of a great number of frames. It is also important to notice that at the lower frequencies the positive phase contrast amplitude is more reduced, and, therefore, more easily influenced by the presence of noise.

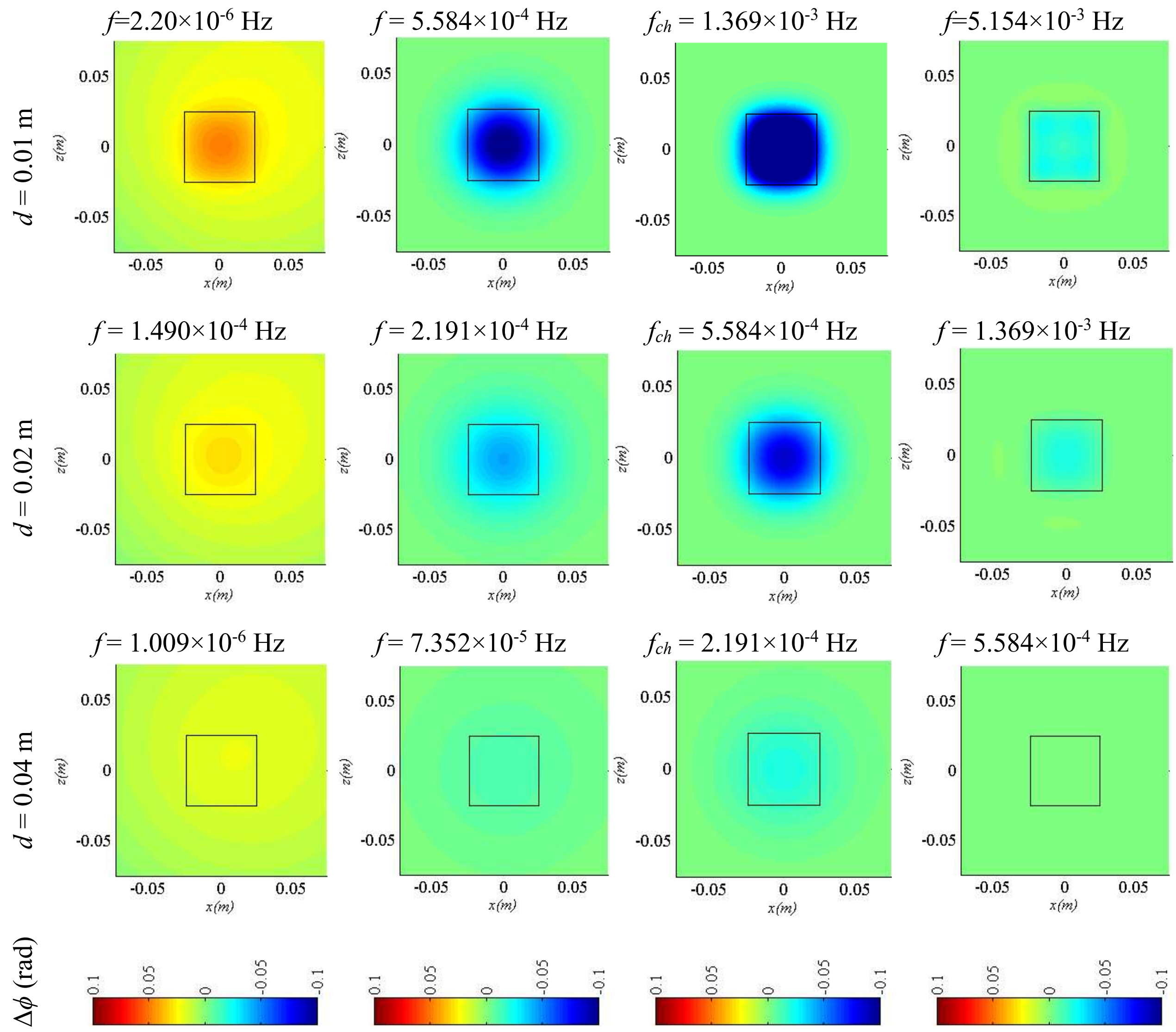

Figure 5.13: Snapshots of the corrected phase contrast results, in radians, recorded over G2 for varying defect depth, taken at several frequencies.

5.3 Experimental vs numerical results

A number of active IRT experiments were performed on test specimens that contain thin defects located at different depths within one of its layers. In order to avoid the required corrections for 3D heat sources, uniform heating of the surface of the test specimens was accomplished by using two halogen lamps to perform the long pulse thermal stimulation and the tests were performed under controlled conditions. Thermal wave phase was calculated by applying a Fourier transform to the temperature results recorded in each pixel of the thermal image and phase contrast was computed by selecting a pixel located in an area which is considered to be weakly influenced by the defect (sound area) to act as a reference for sound results.

The test specimen and the experimental apparatus are presented next.

5.3.1 Experimental apparatus

Active IRT tests were performed using a FLIR A615 camera connected to a control unit (Automation Technology IRX-Box) and to a computer with IR NDT 1.74 software. The IRT camera has the following technical specifications: 640×480 pixels resolution; 7.5-14 μm spectral range; field of view (FOV) of 25°×19°; 0.68 mrad spatial resolution; thermal sensitivity/noise equivalent temperature difference (NETD) <0.05 °C @ 30 °C and accuracy of ±2 °C or 2 %. The tests were performed in reflection mode with the camera 0.70 m away from the surface being inspected and using two 2500 W halogen lamps. A scheme of the experimental setup is shown in Figure 5.14. The resulting FOV of the recorded images is 0.296×0.228 m^2 (see Figure 5.15).

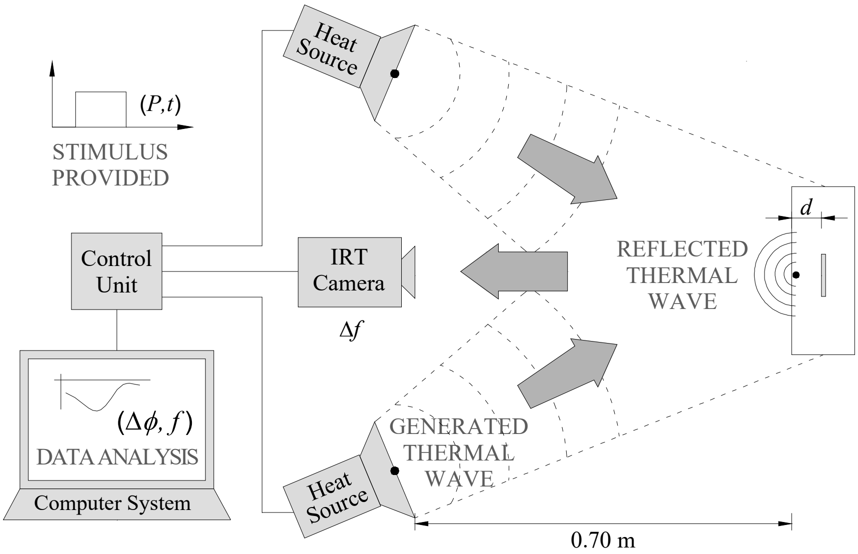

Figure 5.14: Scheme of the experimental apparatus.

The thermal stimulation was performed following a rectangular heating function. In each test, thermal images were recorded for a defined length of time (total test duration of 8192 s), which includes an initial offset period (100 s), a heating period (200 s) and a cooling down period (remainder of the recording time). A total of 256 thermal images were recorded in each test, corresponding to an acquisition frequency of 0.03125 Hz (256 frames recorded for 8192 s).

5.3.2 Test specimen

Three test specimens were constructed to simulate defective building elements with thin inclusions located at three different depths: $d = 0.01$ m and $d = 0.02$ m and $d = 0.04$ m. A schematic representation of a test specimen, along with the location of the defect, is given in Figure 5.15.

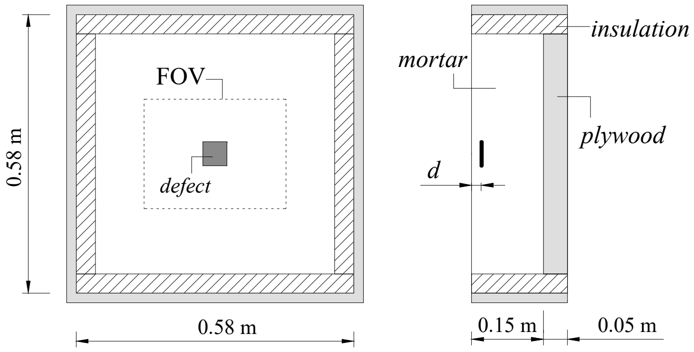

Figure 5.15: Schematic front view and cross section of one of the test specimens.

Each test specimen was assembled by pouring a cement based mortar mix into a box constructed with a marine plywood, and by carefully placing a 0.05×0.05 m^2 defect made from 0.0022 m thick polyethylene foam at the specific desired depth. An insulation layer of 0.04 m (extruded polystyrene foam) was placed along the lateral boundaries of the specimen in order to minimize heat flow exchange.

Prior to the IRT experiments, thermal characterization tests were performed to determine the conductivity λ, specific heat c and density ρ of the materials used in the test specimen. To compute density, measurements of linear dimensions and mass were performed after constant mass is achieved with conditioning at 23 ºC and 50 % relative humidity. Thermal conductivity was determined using the guarded hot plate method in accordance with EN 12664:2001 and EN 12667:2001. Specific heat was obtained by differential scanning calorimetry. The resulting thermal properties given in Table 5.1 correspond to the average values obtained for three different test samples of each material.

5.3.3 Results and discussion

For each pixel in the FOV, phase results were calculated by applying a Fourier transform to the thermal wave results recorded in the time domain. Phase contrast was then determined by computing the difference between the phase recorded in each pixel and the phase recorded at a receiver located in a sound area (one that is not influenced by the defect). For each pixel, calculations were performed considering the average temperature in the neighbouring pixels using a total of 25 pixels.

Phase contrast images

The images in Figure 5.16 show the experimental phase contrast obtained for the several defect depth cases, taking a receiver located in the lower left of the FOV as the reference for sound zone. The snapshots at the centre correspond to the frequency at which maximum absolute phase contrast is found for a pixel located at the centre of the image, corresponding to the centre of the defect. The other two frequencies in the left and right columns were randomly selected in order to illustrate the evolution of phase contrast along the frequency spectrum. To allow for an easier interpretation of the images, the outline of the defect is drawn over the FOV.

The results show that using a phase contrast approach and the mentioned test parameters enabled the detection of the polyethylene foam defect for the cases of $d = 0.01$ m and $d = 0.02$ m, but not for $d = 0.04$ m. Note that, for this case all frequencies shown were selected arbitrarily since the characteristic frequency could not be established. It can be seen that when the defect is closer to the surface, its visibility is greater and it is possible to fully outline the defect. On the other hand, in the case of $d = 0.02$ m, while the defect is still detected, it is not possible to make out its geometry and size with any accuracy. Also, visible in the results are non-intentional defects in spots of positive phase contrast amplitude, which correspond to heterogeneities of the material in this test specimen.

By comparing the numerical results obtained in the previous section (Figure 5.13) and these experimental results one arrives at very similar conclusions: the defect at $d = 0.01$ m is visible with a clear geometry in all selected frequencies and the defect located at $d = 0.02$ m is only detectable in the first two selected frequencies and its geometry is not well defined. The deeper defect at $d = 0.04$ m is not detectable in the experimental phase contrast images and is only slightly visible in the numerical results. The fact that this difficulty is greater in real experiments can be explained by the presence of noise, the precision of the equipment, and the material heterogeneities.

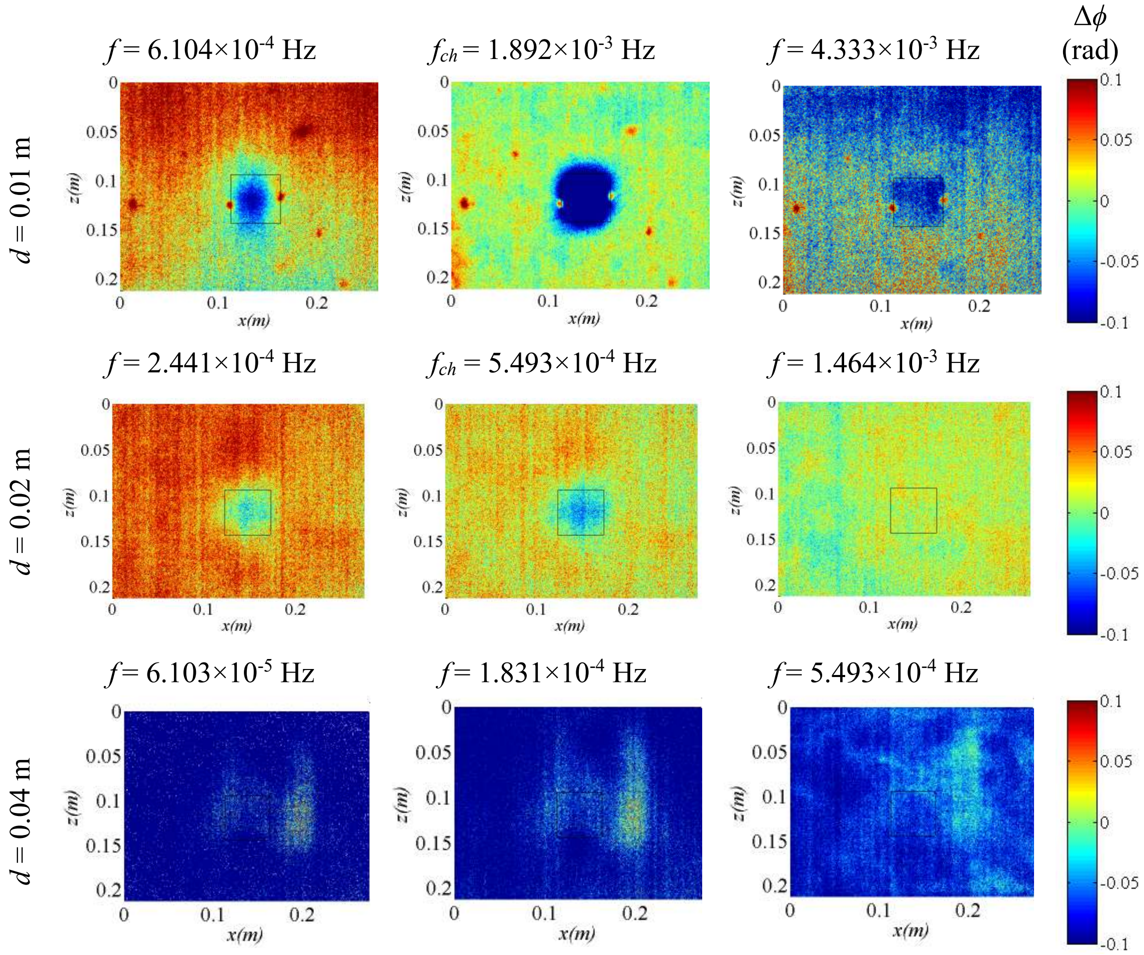

Figure 5.16: Snapshots of experimental phase contrast results recorded for varying defect depths, taken at several frequencies.

Phase contrast curves

Numerical and test results were also extracted in terms of phase contrast curves for a specific pixel (receiver) in the phase contrast images. For each of the defect depths considered, shown in Figure 5.17 shows the results obtained for the receiver located at the centre of the defect which coincides with the centre of the FOV in Figure 5.15, and the centre of the grid of receiver G2 in Figure 5.8.

Looking at the phase contrast curves obtained experimentally and numerically, the influence of the noise in the test results data (which is also visible in the results in Figure 5.16) is clearly evident. As a result, smooth well defined curves could not be obtained from this experimental study. Nonetheless, the amplitude of the phase contrast and characteristic frequencies are close. It should be noted that, the results in the higher frequencies (after the detection threshold) are not meaningful. It is also visible that, the characteristic frequency for the deepest defect is more susceptible to the presence of noise. In fact, there is no discernible peak in the experimental curve for the case of the defect at $d = 0.04$ m.

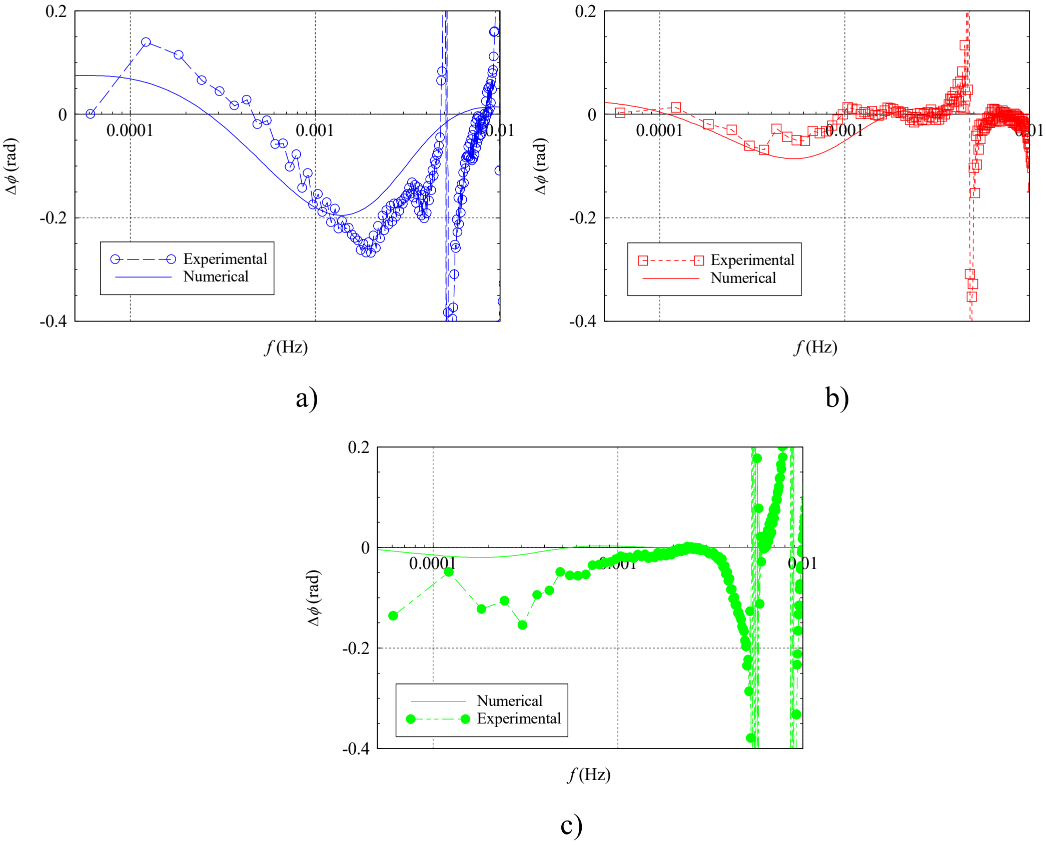

a) b)

c)

Figure 5.17: Numerical and experimental phase contrast curves obtained for a receiver located at the centre of the defect, for different defect depths: a) $d = 0.01$ m; b) $d = 0.02$ m and c) $d = 0.04$ m.

5.4 Final statements

This chapter presents a numerical model to simulate 3D heat diffusion in multilayered media containing thin defects for infrared thermography (IRT) applications using the phase contrast approach. The present model incorporates analytical solutions for multilayered media into a 3D normal derivative integral equation formulation (TBEM) in order to handle a thin defect (inclusion with assumed null thickness) without the need to discretize the domain or the interfaces between the layers.

A detailed formulation of the model in the frequency domain has been provided, along with a verification performed against the previous 3D TBEM model (presented in Chapter 2) using a half-space geometry. Then, in order to illustrate its potential for IRT test results simulation, a numerical application of the model was performed to compute phase contrast results. These results confirm the usefulness of the phase contrast approach in IRT tests for detecting and characterizing defects located beneath the surface. Furthermore, a correction technique that accounts for the off-centre placement and three-dimensionality of the point heat source was successfully employed in the range of frequencies that are useful for IRT data analysis.

Active IRT tests were conducted on test specimens containing thin defects located at several depths. In this case, the results were highly influenced by the presence of noise in the experimental IRT data. When compared with the other experimental results (obtained in Chapter 4), these last experiments were more heavily influenced by noise. This was to be expected since, even though both campaigns were performed in controlled laboratorial environments, the type of test specimen differed. From the results in previous chapters, it was concluded that depth, size and thickness are defect characteristics with major importance for the phase contrast amplitude results. In these tests the defects are considerably smaller (from 0.2×0.2 m^2 to 0.05×0.05 m^2) and thinner (from 0.04 m to 0.0022 m). The heat field disturbance generated by such defects is therefore subtler and more susceptible to the presence of noise.

Nonetheless, the amplitude of the maximum phase contrast and characteristic frequency values were close for the numerical and experimental results. Therefore, this model is found to be useful for simulating results of active IRT tests performed in defective layered building systems, contributing to the interpretation of experimental IRT performed on buildings elements and to the definition of test parameters.

References

[1] Balaras C.A., Argiriou A.A., Infrared thermography for building diagnostics, Energy and Buildings, Vol. 34, pp. 171-183, 2002.

[2] Grinzato E., Vavilov V., Kauppinen T., Quantitative infrared thermography in buildings, Energy and Buildings, Vol. 29, pp. 1-9, 1998.

[3] Ibarra-Castanedo C., Maldague X., Pulsed phase thermography reviewed, Quantitative InfraRed Thermography Journal, Vol. 1 (1), pp. 47-70, 2004.

[4] Brebbia C.A., Telles J.C., Wrobel L.C., Boundary Elements Techniques: Theory and Applications in Engineering, Springer-Verlag, Berlin-New York, 1984.

[5] Bathe K.J., Numerical Methods in Finite Element Analysis, Prentice-Hall, New Jersey, 1976.

[6] Özişik M.N., Finite Difference Methods in Heat Transfer, CRC Press Inc., USA, 1994.

[7] Tadeu A., Simões N., Three-dimensional fundamental solutions for transient heat transfer by conduction in an unbounded medium, half-space, slab and layered media, Engineering Analysis with Boundary Elements, Vol. 30 (5), pp. 338-349, 2006.

[8] Tadeu A., António J., Simões N., 2.5D Green's functions in the frequency domain for heat conduction problems in unbounded, half-space, slab and layered media, Computer Modelling in Engineering and Sciences - CMES, Vol. 6 (1), pp. 43-58, 2004.

[9] Sommerfeld A., Mechanics of deformable bodies, New York: Academic Press, Inc., 1950.

[10] Ewing W.M., Jardetzky W.S., Press F. Elastic Waves in Layered Media, McGraw-Hill Book Company, 1957.

[11] Rudolphi T.J., The use of simple solutions in the regularisation of hypersingular boundary integral equations, Mathematical and Computer Modelling, Vol. 15, pp. 269-278, 1991.

[12] Hong H., Chen J., Derivations of integral equations of elasticity, Journal of Engineering Mechanics, ASCE, Vol. 114 (6), pp. 1028-1044,1988.

[13] Tadeu A., Prata J., Simões N., Closed form integration of singular and hypersingular integrals in 3D BEM formulations for heat conduction, Mathematical Problems in Engineering (2012), Article ID 647038.

[14] Serra C., Tadeu A., Prata J., Simões N., Application of 3D heat diffusion to detect embedded 3D empty cracks, Applied Thermal Engineering, Vol. 61 (2), pp. 596-605, 2013.

[15] Vavilov V., Kauppinen T., Grinzato E., Thermal characterisation of defects in building envelopes using long square pulse and slow thermal wave techniques, Research Non-Destructive Evaluation, Vol. 9, pp. 181–200, 1997.

[16] Maierhofer Ch., Brink A., Röllig M., Wiggenhauser H., Transient thermography for structural investigation of Concrete and Composites in the Surface Near Region, Infrared Physics and Technology, Vol. 43 (3-5), pp. 271 – 278, 2002.

[17] Arndt R.W., Square pulse thermography in frequency domain as adaptation of pulsed phase thermography for qualitative and quantitative applications in cultural heritage and civil engineering, Infrared Physics & Technology, Vol. 53 (4), pp. 246-253, 2010.

[18] Mills A.F., Heat Transfer, Second Edition, Prentice Hall, New Jersey, 1999.

CHAPTER 6

CONCLUSIONS

6 CONCLUSIONS

6.1 Final statements

The main objective that was set out for the research work presented in this thesis was to develop and implement heat diffusion modelling techniques that contribute to the quantitative interpretation of experimental transient results obtained in infrared thermography (IRT) applications in buildings. The work was motivated by the fact that, even though studies using active IRT have demonstrated great potential for detecting and evaluating defects in many other fields (aeronautics, mechanics, electronics, etc.), there is a lack of testing and data processing techniques adequate for common construction materials and building systems. In order for IRT applications to become more widespread in building envelopes inspections, it was considered essential to understand the interaction that occurs between heat source, building elements and their potential defects, taking into account the thermal properties of common construction materials, and the fact that many constructive systems are composed by several layers of different materials. It is also important to understand the limitations associated with using the technique in building systems. In order to achieve this, both simulations and experimental tests were carried out to investigate the effects caused by the presence of null thickness inclusions that simulate very thin defects in building elements, such as small cracks, delaminations, or material inclusions.

Throughout the work, the complexity of the problem increased from modelling a thin defect located somewhere in an unbounded medium to simulating a defective multilayered system. The study focused mainly on attaining heat field results in terms of thermal wave phase, in order to explore the advantages of analysing defects using a phase contrast approach. Therefore, the problem was posed in the frequency domain, which allows phase to be calculated directly using the frequency domain temperature response. In the case of the experimental tests, a Fourier transform was applied to the time domain temperature results in order to obtain frequency domain temperature.

First, in order to model three-dimensional (3D) heat diffusion in the proximity of a 3D null thickness defect located in an unbounded uniform solid medium, a formulation of the boundary element method in terms of normal derivative integral equation (TBEM) to obtain numerical phase contrast results was proposed and implemented. The verification of the numerical model against a response obtained analytically using a cylindrical inclusion and a mirror image source technique was also performed. In order to perceive better the effect that an embedded defect has on the surrounding heat field, time domain temperature results were also obtained using an inverse Fourier transform. Additionally, in order to understand the influence of considering either a 3D or 1D heat source in the simulations, calculations were performed using both types of heat sources.

Looking to evaluate key factors that influence IRT results, a number of numerical applications were performed, considering several variations to an initial case study of a vertical thin plane inclusion with specific dimensions, located at a certain distance from a 3D heat source or 1D heat source. The frequency domain temperature response was computed for three grids of receivers located in the medium, one of which represented the supposed surface being inspected using IRT. For each case, calculations were performed twice, once for the defective medium and then for a similar medium subjected to the same heat source (3D or 1D), but in which the defect is absent. This second calculation is used as the reference sound medium, which is required for phase contrast calculations. Then, to understand the evolution of phase contrast along the frequency spectrum, phase contrast curves were extracted for specific receivers. The numerical results obtained in this study demonstrated the potential that phase contrast curves have to characterize defects, since they revealed to be uniquely influenced by certain factors. In particular, the influence of defect characteristics such as size and depth was very noticeable in these curves, both in terms of maximum visibility (maximum phase contrast achieved at a certain characteristic frequency) and defect visibility threshold (given by the blind frequency). The results revealed that a limitation of this type of analysis may have been related to the position of the defect, since its inclination influenced the results and provided a mixed response along the receivers which is not easy to interpret. Regarding the type of heat source being modelled, using a 1D source revealed the advantage of not being influenced by the distance to the source.

Even though boundary element models have the advantage over domain discretization methods of only requiring the discretization of the inclusion being modelled, the simulation of 3D heat conduction around 3D thin defects still involves considerable computational effort. Therefore, an iterative approach to the 3D TBEM formulation was proposed to reduce the processing (CPU) time required for the calculations. Its implementation to a system of unbounded solid media containing four plane inclusions, lead to promising results. The average CPU time was greatly reduced because the size of each system of equations associated with each inclusion is smaller than the full 3D TBEM system. Additionally, the possibilities of pairing two inclusions at each step (instead of considering each inclusion separately) was also studied and the number of iterations required for each case was recorded. This iterative approach can be particularly useful, not only to reduce the time required to model multiple inclusions, but also to model any thin defect if it is considered to be divided into several subdomains.

Then, in order to deal with the fact that many current building elements are made up of multiple layers of different materials, the research proceeded to focus on modelling an IRT setup using a multilayered model. In this case, instead of considering a thin inclusion, the defect was simulated by one of the layers in the media. Hence, now the influence of defect characteristics on results was studied by changing parameters related to a certain layer which was considered to be the defect under study. Again, phase contrast was obtained by performing frequency domain calculation twice, once for the multilayered media in which such layer is present, and then for a medium in which such layer is absent. These calculations were performed analytically, using fundamental solutions (Green's functions) obtained by a double spatial Fourier transformation. In order to simulate IRT tests in which uniform heating of the surface is achieved, the analytical solution was manipulated to consider an imposed temperature at one of the boundary interfaces, which reduced the problem to a 1D model. Active IRT tests were performed, and experimental and analytical results were compared considering varying defects and experimental setup parameters. In this model, the defect is considered to have infinite dimension in two directions, however because the layer has a certain thickness it was possible to additionally analyse the influence of varying the thickness of the defect. The analytical curves were able to generate results that were reasonably close to the experimental results and led to the same conclusions regarding the influence of key parameters in IRT tests. The influence that the presence of noise has on results was also studied by simulating random temperature variations in the numerical results. It was concluded that the noise can noticeably influence the results, particularly at high frequencies.

Looking to simulate the case of IRT tests performed on multilayered building elements that may contain 3D thin defects, a more sophisticated model was developed. In this case, the 3D heat field anywhere in the system is determined by the presence of the defect, the 3D heat source, and the reflections that occur at each interface between layers. This problem was formulated by combining the 3D TBEM to model a 3D defect, with analytical expressions for multilayered media that avoid the discretization of the interfaces. In order to simplify the 3D problem, analytical solutions expressed as Bessel integrals were used in the model. The proposed formulation was verified using a mirror image source technique to enable comparisons with the former 3D TBEM proposed for unbounded media. Since in experimental tests it is necessary to choose a sound area, this was taken into account in the numerical simulation by considering a single pixel as the reference for phase contrast calculation. The effects caused by this consideration required the use of a correction technique to account for the 3D nature of the point heat source. It should be noted that this issue was not relevant in the previous study because the defect being modelled had infinite extent and the heat source was planar. To avoid this correction, practical active IRT experiments were performed to test specimens with more than one layer and containing thin defects located at several depths using two halogen lamps to ensure uniform heating. In this case, as expected, due to the size and thickness of the defects considered, the results were more heavily influence by the presence of noise in the experimental IRT data. Nonetheless, the amplitude of the maximum phase contrast and characteristic frequency values were approximate for both the numerical and the experimental results.

Hence, it is considered that the proposed models can effectively be used to predict the detectability of defects in multilayered media and can be particularly useful to define experimental setup parameters.

6.2 Future studies

Through the development and implementation of numerical and analytical models formulated in the frequency domain, this research focused on simulating experimental IRT test results, following in particular a phase contrast approach. These allowed for the evaluation of key factors that influence IRT tests data, which is an essential contribution to the interpretation of IRT test data for defect characterization studies using the phase contrast approach. Nonetheless, the need to investigate IRT applications in buildings goes well beyond the present study, and future studies are still necessary for the advancement of IRT applications in buildings.

Namely, as a continuation of the present work it will be relevant to:

- Explore the potential of the active IRT technique to detect specific pathologies in buildings such as the presence of excessive moisture, the detachment of coating materials and the identification of fixing anchors in external thermal insulation composite systems;
- Define the relationships between important defect characteristics (depth, size) and parameters of interest in phase contrast curves (characteristic frequency, blind frequency) that occur in construction materials;
- Define the basic experimental setup required for known common buildings solutions (concrete, masonry and wood systems);
- Perform active IRT experiments to actual building elements to identify practical difficulties associated with the implementation of the technique in-situ, in particular the due to the presence of wind, solar radiation and moisture;
- Model thin inclusions filled with other materials, in which both continuity of temperatures and heat fluxes need to be imposed at the inclusions interfaces;
- Develop coupled (or hybrid) formulations that combine the numerical methods used in this thesis with other established classical numerical methods, as well as with more recently developed techniques, such as the meshless methods. Using this kind of formulations will make it possible to benefit from the main advantages of each method. In particular, it can help reduce the required processing time (or enable the modelling of

more comprehensive heat diffusion domains using the same resources) and allow for the modelling of heat diffusion trough media whose properties may vary spatially.